*University of Basilicata*

Doctoral research (PhD) programme in
ENGINEERING FOR INNOVATION AND SUSTAINABLE DEVELOPMENT

# A FOUR-DIMENSIONAL SOIL MOISTURE PRODUCT: CLOSING THE SOIL PROFILE GAP WITH A SWI-SMAR APPROACH.

Academic Discipline
ICAR/02


PhD Coordinator:
Prof. Aurelia SOLE

Candidate:
Eng. Arianna MAZZARIELLO

Supervisor:
Prof. Aurelia SOLE

Co-supervisor:
Eng. PhD Raffaele ALBANO


Ciclo: XXXVI

**Per aspera ad astra.**

***A chi mi ha sostenuto.***
***A chi c'è stato.***
***A chi c'è.***

***Alla mia famiglia e al mio Gelsomino.***

**ABSTRACT**

The increasing frequency and intensity of extreme meteorological and climatic events, such as droughts and floods, represent a direct manifestation of the growing impacts of climate change on natural hazards. Within the context of these phenomena, one of the crucial parameters to be considered is the variability of the Soil Moisture (SM), namely the soil water content from the soil surface up to the root zone (RZ) depth. However, to fully understand the four dimensions (i.e., 3D spatial plus temporal) SM evolution and its implications for associated risks, it is essential to have access to high-resolution temporal and spatial data.

Currently, SM information retrieval relies on three main approaches: ground-based measurements, hydrological modeling, and remote sensing. However, each method has its own limitations as well as advantages. Ground-based measurements often provide high quality point data, but they are unevenly distributed across territories with limited spatial extension, and that can be affected by systematic probe errors. On the other hand, hydrological modelling can extend the scale of application but relies heavily on the fundamental assumptions of the model used as well as on the quality of the available input/ancillary data. Finally, satellite sensors can provide a synoptic view and high frequency of observation, but often struggle to simultaneously provide adequate spatial and temporal resolution.

The integration of data from ground measurements, remote sensing, and hydrological modeling could allow for filling the gap(s) in each approach, fostering the creation of an innovative and cost-effective monitoring system. Such an integrated approach would also be capable of providing precise measurements along the soil profile, addressing another open field in SM research.

This thesis aims at bridging these gaps by addressing three key questions. Firstly, it seeks to explore the peculiarities of SM products within the European context

encompassing the Mediterranean area recognized as one of the areas most impacted by climate change. Secondly, it aims to investigate the possibility of integrating different SM products on a large scale. Lastly, it focuses on examining the feasibility of constructing high-resolution spatial (x, y) and temporal (t) information at various soil depths (d). The development and testing of a 4D SM product would facilitate the acquisition of accurate SM information throughout the soil layer, from the surface to the root zone, holding the potential to significantly enhance our understanding of soil moisture dynamics.

To reach such results, several intermediate steps have been developed, starting with a preliminary analysis of the accuracy of a few satellite-based SM products, trying to investigate which one offers the best performance also concerning the goal of create a 4D SM product. Such an analysis has been carried out, for the first time in this work, at the European ecoregions spatial scale, by an intercomparison of five SM datasets with the ground information made available by the International Soil Moisture Network (ISMN). This preliminary analysis allowed us to both assess the different performance of the considered products, and to understand that the ecoregion scale could be a suitable investigation level to capture dynamic behavior patterns. A deeper exploration of previous findings and a confirmation of the behavior of these ecoregions concerning seasonality, including the complete removal of seasonality and studying the relationships with phenological phases, were then carried out. Finally, focusing only on active microwave sensors, which have demonstrated a different level of accuracy, the 4D SM product has been developed and tested. In particular, ASCAT (H119-H120) and the enhanced S-1 SM product, both based on active measurements in the C-band, were considered. The first is sub-daily provided at about 25km of spatial resolution, while the second one can allow for information at a higher spatial resolution (1km for the Surface Soil Moisture – SSM - data) but with a sub-weekly temporal resolution. Two different approaches, the Soil Water Index (SWI) and Soil Moisture Analytical

Relationship (SMAR), respectively, were then applied to the data, first to produce the blended SSM product, and then the RZSM one.

The results obtained provide an overview of the fundamental role of SM, which is helpful in issues related to climate change. In particular, the application of SCAT-SAR SWI SMAR demonstrated a substantial correlation with in-situ data ($r \sim 0.8$), along with significantly reduced prediction errors (RMSD ~ 0.003/0.01). At the regional level, the application of SMAR provided more consistent information on RZSM with real hydraulic processes compared to the SWI application, which displayed a simple reduction in saturation values while maintaining the same input data pattern. This discrepancy can be attributed to the absence of a clear connection between soil depth and the parameter T.

The proposed method involves a limited number of parameters and is easily implementable. Since the SWI-SMAR approach is based on a recursive algorithm, the output improves as the time series length increases. This approach could prove particularly useful for large-scale studies to advance our understanding of the effects of climate change and risk management. However, current limitations arise from approximations of parameters as the normalized coefficient of losses (a), or the normalized coefficient related to the soil properties and the depth (b), or the saturation at wilting point ($s_w$), or the saturation at field capacity ($s_c$), and the computational capacity required for processing large volumes of data (with a nine GB output for the sole application in the Basilicata region). Addressing these obvious gaps and enhancing the accuracy of the predictions along the soil profile would require improvements in parameter derivation. Future developments could include integration with additional field experiments and the use of artificial intelligence methodologies.

**SINOSSI**

L'incremento nella frequenza e nell'intensità degli eventi meteorologici e climatici estremi, come siccità e inondazioni, rappresenta una manifestazione diretta degli impatti in aumento dei cambiamenti climatici sui rischi naturali. Nel contesto di tali fenomeni, la variabilità della SM, ossia il contenuto d'acqua nel suolo dalla superficie fino alla profondità della zona delle radici (RZ), svolge un ruolo di cruciale importanza. Tuttavia, per comprendere appieno l'evoluzione della SM in quattro dimensioni (cioè, spaziale in 3D più la dimensione temporale) e le sue implicazioni per i rischi associati, è essenziale avere accesso a dati temporali e spaziali ad alta risoluzione.

Attualmente, l'acquisizione delle informazioni sulla SM si basa su tre principali approcci: misurazioni in situ, modellazione idrologica e misure telerilevate. Tuttavia, ciascun metodo ha i propri limiti e vantaggi. Le misurazioni in situ forniscono spesso dati puntuali di alta qualità, ma sono distribuiti in modo disomogeneo sui territori con limitata estensione spaziale e possono essere influenzati da errori sistematici delle sonde. D'altra parte, la modellazione idrologica può estendere le scale di applicazione, ma dipende pesantemente dalle assunzioni fondamentali del modello utilizzato e dalla qualità dei dati di input/ancillari disponibili. Infine, i sensori satellitari possono fornire una vista sinottica e una frequenza elevata di osservazione, ma spesso faticano a fornire contemporaneamente una risoluzione spaziale e temporale adeguata. L'integrazione dei dati provenienti dalle misurazioni in situ, dal telerilevamento e dalla modellazione idrologica potrebbe consentire di colmare le lacune di ciascun approccio, favorendo la creazione di un sistema di monitoraggio innovativo ed economicamente vantaggioso. Un tale approccio integrato sarebbe inoltre in grado di fornire misurazioni precise lungo il profilo del suolo, affrontando un altro campo aperto nella ricerca sulla SM.

Questa tesi si propone di colmare queste lacune affrontando tre domande chiave. In primo luogo, cerca di esplorare le peculiarità dei prodotti di SM nel contesto europeo che comprende l'area mediterranea, riconosciuta come una delle aree più colpite dal cambiamento climatico. In secondo luogo, mira a investigare la possibilità di integrare diversi prodotti di SM su larga scala. Infine, si concentra sull'esame della fattibilità di costruire informazioni spaziali (x, y) e temporali (t) ad alta risoluzione a diverse profondità del suolo. Lo sviluppo e la sperimentazione di un prodotto di SM a 4D faciliterebbero l'acquisizione di informazioni precise sull'SM lungo l'intero strato di suolo, dalla superficie alla zona radicale, con il potenziale di migliorare significativamente la comprensione delle dinamiche dell'umidità del suolo.

Per raggiungere tali risultati, sono stati sviluppati diversi passaggi intermedi, a cominciare da un'analisi preliminare dell'accuratezza di alcuni prodotti di SM basati su satelliti, cercando di individuare quale offra le migliori prestazioni anche riguardo all'obiettivo di creare un prodotto 4D di SM. Tale analisi è stata condotta, per la prima volta in questo lavoro, alla scala spaziale delle ecoregioni europee, attraverso un'intercomparazione di cinque dataset di SM con le informazioni in situ messe a disposizione dall'International Soil Moisture Network (ISMN). Questa analisi preliminare ci ha permesso sia di valutare le diverse prestazioni dei prodotti considerati, sia di comprendere che la scala delle ecoregioni potrebbe essere un livello di indagine adatto per catturare i modelli di comportamento dinamico. Successivamente, è stata condotta un'approfondita esplorazione delle scoperte precedenti e una conferma del comportamento di queste ecoregioni riguardo alla stagionalità, compresa la rimozione completa della stagionalità e lo studio delle relazioni con le fasi fenologiche. Infine, concentrandosi solo sui sensori a microonde attivi è stato sviluppato e testato il prodotto 4D di SM. In particolare, sono stati considerati i prodotti ASCAT (H119-H120) e il prodotto migliorato derivante da S-1, entrambi basati su misurazioni attive nella banda C. Il primo è

fornito in modo sub-giornaliero con una risoluzione spaziale di circa 25 km, mentre il secondo può fornire informazioni a risoluzione spaziale più elevata (1 km per i dati di SM superficiale - SSM) ma con una risoluzione temporale sub-settimanale. Due diversi approcci, il Soil Water Index (SWI) e la Soil Moisture Analytical Relationship (SMAR), sono stati quindi applicati ai dati, prima per produrre il prodotto SSM combinato e poi quello di RZSM.

I risultati ottenuti forniscono una panoramica del ruolo fondamentale dell'umidità del suolo, utile per le questioni legate al cambiamento climatico. In particolare, l'applicazione di SCAT-SAR SWI SMAR ha dimostrato una sostanziale correlazione con i dati in situ ($r \sim 0,8$), insieme a errori di previsione significativamente ridotti (RMSD ~ 0,003/0,01). A livello regionale, l'applicazione di SMAR ha fornito informazioni più coerenti su RZSM con veri processi idraulici rispetto all'applicazione SWI, che ha mostrato una semplice riduzione dei valori di saturazione mantenendo lo stesso modello di dati di input. Questa discrepanza può essere attribuita all'assenza di una chiara connessione tra la profondità del suolo e il parametro T.

Il metodo proposto coinvolge un numero limitato di parametri ed è di facile implementazione. Poiché l'approccio SWI-SMAR si basa su un algoritmo ricorsivo, l'output migliora man mano che la serie temporale si estende. Questo approccio potrebbe dimostrarsi particolarmente utile per studi su larga scala per avanzare nella comprensione degli effetti del cambiamento climatico e della gestione del rischio. Tuttavia, le attuali limitazioni derivano da approssimazioni nei parametri come il coefficiente normalizzato delle perdite (a), il coefficiente normalizzato relativo alle proprietà del suolo e alla profondità (b), la saturazione al punto di appassimento ($s_w$), la saturazione alla capacità di campo ($s_c$), e dalla capacità computazionale richiesta per l'elaborazione di grandi volumi di dati (con una produzione di nove GB per l'applicazione nella sola regione della Basilicata).

Per affrontare queste lacune evidenti e migliorare l'accuratezza delle previsioni lungo il profilo del suolo, sarebbe necessario un miglioramento nella derivazione dei parametri. Sviluppi futuri potrebbero includere l'integrazione con ulteriori esperimenti sul campo e l'uso di metodologie di intelligenza artificiale

**PUBLICATIONS:**
Some ideas and figures have appeared previously in the following works:

- Mazzariello, A., Albano, R., Lacava, T., Manfreda, S., Sole, A., 2023. Intercomparison of recent Microwave satellite Soil Moisture Products on European Ecoregions. Journal of Hydrology 130311. https://doi.org/10.1016/j.jhydrol.2023.130311

- Mazzariello, A., Albano, R., Sole, A., Lacava, T., 2023. SCAT-SAR SWI SMAR: un prodotto 4D di soil moisture. Giornate dell'Idrologia 2023.

- Mazzariello, A., Albano, R., Sole, A., Lacava, T., 2023 VALUTAZIONE DI UN NUOVO PRODOTTO DI UMIDITÀ DEL SUOLO 4D SULLA BASILICATA. PhD days- Matera |GRUPPO iTALIANO DI iDRAULICA.

- Albano, R., Mazzariello, A., Lacava, T., Manfreda, S., Sole, A., 2023. Satellite-based soil moisture product performance assessment among the EU Ecoregions (other). https://doi.org/10.5194/egusphere-egu23-11433.

- Mazzariello, A., Albano, R., Sole, A., Lacava, T., Manfreda, S., 2022. Inter-comparison of Soil Moisture Satellite products on160; European Ecoregions (other). display. https://doi.org/10.5194/egusphere-egu22-4169

- Notarangelo, N.M., Mazzariello, A., Albano, R., Sole, A., 2021. Comparing Three Machine Learning Techniques for Building Extraction from a Digital Surface Model. Applied Sciences 11, 6072. https://doi.org/10.3390/app11136072

## INTRODUCTION

This study was supported by the School of Engineering at the University of Basilicata, as part of the Ph.D. Program "Engineering for Innovation and Sustainable Development" (curriculum: Methods and Technologies for Environmental Monitoring and Protection). The thesis presented here, titled "A Four-Dimensional Soil Moisture Product: Closing the Soil Profile Gap with a SWI-SMAR Approach," aims to outline a scientific-technical innovative scenario by using an integrated system of measurements to delineate 4D soil moisture information. The investigative process was conducted in conjunction with contextualization and theoretical references. The research took place in Italy and Austria, particularly in Potenza and Vienna.

In an era of climate change, the scope and cumulative consequences of both natural and human-made disasters underscore the importance of disaster management, which refers to a set of principles and strategies for preventing, reducing, or controlling risk (EM-DAT 2019). Extreme weather events resulting from climate change can alter the hydrological regime by increasing the frequency and magnitude of floods (IPCC and others, 2013), droughts, and landslides. Mediterranean regions present a highly modified landscape. A correct representation of any phenomenon related to climate change requires soil moisture information at a temporal resolution of at most daily and a spatial resolution of kilometers.

Currently, most soil moisture data on a larger or smaller scale are obtained from ground-based or remote sensing measurements, which may have some limitations (limited temporal or spatial resolution, high cost). In this context, one of the greatest potentials lies in the integration of sensors, remote sensing measurements, and hydrological modeling. Several studies have developed new techniques to

retrieve large-scale soil moisture information with low operational costs that can be effectively combined with modeling systems.

Technology may play a pivotal role in improving soil moisture prediction, especially in the root zone. Applications related to climate change can benefit from recent technological advancements in data storage, big data management, and computational algorithms. Recent years have witnessed a significant increase in the amount of data continuously produced and collected for various purposes, which can be combined to provide valuable information along the soil profile. The overall goal of this thesis was to enhance soil moisture prediction through an evolution of the fusion algorithm along the soil profile.

The key idea is to combine freely available data sources, previously unpublished data, and computation techniques, such as the Soil Water Index (SWI) and Soil Moisture Analytical Relationship (SMAR), to devise a method for daily 1 km soil moisture prediction on a large scale for climate change applications in the Mediterranean area. The specific aim was to investigate the capabilities of active and passive remote sensing in Europe and subsequently the use of physically based models to improve predictions within the soil.

In contrast to existing works, the present study focuses on creating a workflow that provides soil moisture information consistent with physical parameters, soil properties, and survey depth. This implies that the more layers for which physical parameters are available, the greater the detail along the profile. Models for soil moisture along the profile were compiled, trained, validated, and tested. They were shown to produce favorable outcomes. The results were applied to Basilicata, using empirical parameters. This approach offers an initial operational tool for low-cost soil moisture monitoring. It can provide a means to monitor and forecast soil moisture on a large scale with high spatial and temporal resolution.

The main drawback pertains to the approximate nature of the parameters and outcomes. Another limitation may arise from machine-specific constraints due to extensive data storage. The overall findings suggest that SWI-SMAR provides an effective method for profiling soil moisture monitoring. Improving the parameters and expanding the analysis region to include all of Italy may be future directions.

The central idea of climate change serves as the starting point for the research in this thesis. Its primary effects, certain general concerns related to international and national agreements, and the role of soil moisture in this context are all summarized in Chapter 1.

Chapter 2 provides a concise review of soil moisture measurement techniques in the literature. The analysis of existing literature led to the definition of the specific research goals, variables, and components.

Chapter 3 addresses the methodology used in this study: a SWI-SMAR approach based on active remote sensing products (i.e., ASCAT and an enhanced version of SSM Sentinel-1).

Chapter 4 includes: a) a preliminary stage of intercomparison between remote sensing soil moisture products at the ecoregion scale; b) an in-depth study of the effects of seasonality on ecoregion performance; c) the creation of the SCAT-SAR SWI datasets used in the SMAR model to obtain the SCAT-SAR SWI SMAR dataset; d) validation on the COSMOS Alento network; e) application to Basilicata.

Chapter 5 outlines the significance of the main findings and includes some suggestions for improvement and speculation on future directions.

**LIST OF FIGURES**

**LIST OF TABLES**

**ACRONYMIS**

ALICE: Absolute Variation of Local Change of Environment index;
AMSR: Advanced Microwave Scanning Radiometer;
AMSU: Advanced microwave sounding unit;
ARC: Alento River Catchment;
ASCAT: Advanced scatterometer;
AVHRR: Advanced Very High Resolution Radiometer;
BRDF: bidirectional reflectance distribution function;
CDF: Cumulative Distribution Function;
CDR: climate data records;
CDTI: Centro para el Desarrollo Tecnológico Industrial;
CGLS: Copernicus Global Land Service;
CNES: French Centre National d'Études Spatiales;
CRNS: cosmic-ray neutron sensors;
ECMWF: European Centre for Medium-Range Weather Forecasts;
ECV: essential climate variables;
EEA: European Environment Agency;
ENVISAT: Environmental Satellite;
EOS: end of growing season;
ESA CCI: European Space Agency Climate Change Initiative;
ET: evapotranspiration;
FAO: Food and Agriculture Organization of the United Nations;
FDR: Frequency-Domain Reflectometry;
GCM: general circulation models;
GCOS: Global Climate Observing System;
GLDAS: Global Land Data Assimilation System;
GPI: Grid Point Locator;
IFS: Integrated Forecasting System;
IGBP: Geosphere-Biosphere Programme;
IPCC: Intergovernmental Panel on Climate Change;
IPF: Institute of Photogrammetry and Remote Sensing;
ISMN: International Soil Moisture Network;
IW: Interferometric Wide swath;
LAI: Leaf Area Index;
LDAS: Land Data Assimilation System
LIS: Land Information System;
LSM: land surface model;
MAP: Mediterranean Action Plan;
MODIS: Moderate Resolution Imaging Spectroradiometer;
MSSD: Mediterranean Strategy for Sustainable Development;
MW: microwave
NASA: National Aeronautics and Space Administration;
NEE: net ecosystem exchange;
NETCDF: Network Common Data Form;
NLDAS: North American Land Data Assimilation System;
NOAA: National Oceanic and Atmospheric Administration;
NPW: Numerical weather prediction;
NWP: numerical weather forecasting;
PPI: Plant phenology index;
PTF: pedotransfer function;
r: Pearson Correlation Coefficient

RFI: Radio Frequency Interference;
RMSD: root mean square difference;
RSME: root mean square error;
RTM: radiative transfer model;
RZ: root zone;
RZSM: root zone soil moisture;
SDG: Sustainable Development Goals;
S-1 SSM: Surface Soil Moisture from Sentinel-1,
SM: Soil Moisture;
SMAP: Soil Moisture Active Passive;
SMAR: soil moisture analytical relationships;
SMI: soil moisture index;
SMOS: Soil Moisture Ocean Salinity;
SMOS-IC: SMOS INRA-CESBIO;
SNR: signal to noise ratio;
SSF: surface state flag;
SSM. Surface Soil Moisture;
SVGS: start of the growing season;
SWI: Soil Water Index;
$T_b$: brightness temperature;
TDR: Time-Domain Reflectometry;
UARC: Upper Alento River Catchment;
UNEP: United Nation Environment Program;
UNFCCC: United Nations Framework Convention on Climate Change
VGSL: Vegetation growing season length;
VIC: Variable Infiltration Capacity;
VOD: Vegetation Optical Depth;
VWC: volumetric water content;
WFP: World Food Program;
WP: wilting point;
WWF: WorldWide Fund;
$\theta$: SM into volumetric water content [$m^3/m^3$];
$\theta_{wp}$: Volumetric water content at wilting point[$m^3/m^3$];
$s_w$: : Saturation at wilting point;
$\theta_{FC}$: Volumetric water content at field capacity [$m^3/m^3$];
$s_C$: : Saturation at field capacity.

*Chapter 1*

# THE CLIMATE CHANGE

Climate change has been a significant and recurring phenomenon in recent decades that is causing numerous detrimental impacts on the environment and society. The global nature of climate change and its anthropogenic origin (Masson-Delmotte et al., 2021) make it a particularly challenging phenomenon to address. The climate has been changing across all corners of the world, resulting in a range of impacts. Its impacts are multiple and far-reaching, and one of the most obvious impacts is the average increase in global temperatures. This increase causes heat waves, droughts, forest fires, and sea level rise in different ways from region to region. In general, 2020 was the hottest year ever recorded, according to the National Aeronautics and Space Administration.

California experienced severe drought from 2011 to 2017, leading to forest fires and problems with the availability of drinking water. Among tropical or subtropical regions, Madagascar experienced a famine in 2021, with over one million people struggling to have enough to eat due to reduced seasonal precipitation and degraded natural resources, as reported by the World Food Program (WFP) (https://www.wfp.org/). Shorter and more intense rainfall, combined with the consequences of increased temperatures, can lead to flooding and the exacerbation of drought. For example, in August 2020, heavy rains caused flash floods in parts of Afghanistan and Pakistan, resulting in at least 160 deaths and damage to thousands of homes. Similarly, in Lombardy and Veneto, Italy, heavy rains during the same period caused at least five deaths. These events illustrate the severe consequences of extreme weather events on human lives and infrastructure. Italy is particularly vulnerable to hydrogeological risks due to its geography and climate.

Significant damage to infrastructure and property can be derived from the increase in frequency and intensity of extreme weather events such as hurricanes, storms, and floods. All these factors are also causing a loss of biodiversity, due to changes in natural habitats, the reduction of wildlife, and the spread of invasive species. This is damaging ecosystems and the ecosystem services they provide.

The effects of climate change are not only limited to the environment; they can also affect human health through the spread of vector-borne diseases, air pollution, and exposure to temperature. This can cause respiratory and cardiovascular problems, among other health issues. Or it presents significant risks to the economy. Reduced agricultural productivity, increased costs associated with infrastructure and sea level damage, and reduced tourism can all cause significant economic losses. It has also been recognized that climate change will lead to economic disparities, especially as the degree of dependence on agriculture is one of the critical factors. Specifically, 86% of the countries in the world will become poorer and income inequality will increase significantly in each of these countries. In the worst projections, variations in precipitation alone will result in a 45% increase in income inequality for the most agriculture-dependent nations, but considering temperature variations, this could increase to a 78% increase in inequality (Palagi et al., 2022). Overall, the described effects constitute the vast majority of natural disasters reported worldwide in the Emergency Events Database (EM-DAT 2022), an international database managed by the Centre for Research on the Epidemiology of Disasters (CRED) at the Catholic University of Louvain. The database collects fundamental data on technological and natural disasters from 1900 to the present, compiled from various sources. The criteria for an event to be classified as a natural disaster include the existence of at least one of the following conditions: 100 or more people affected, 10 or more deaths, a declaration of a state of emergency, or a request for international assistance. Due to social, political, and economic factors, a complete and homogeneous

representation of all regions of the world is impossible, and the actual number of disasters is likely higher. Even if, hazardous events in 2022 were high and increased compared to the period from 2002 to 2021, as shown in Fig. 1.

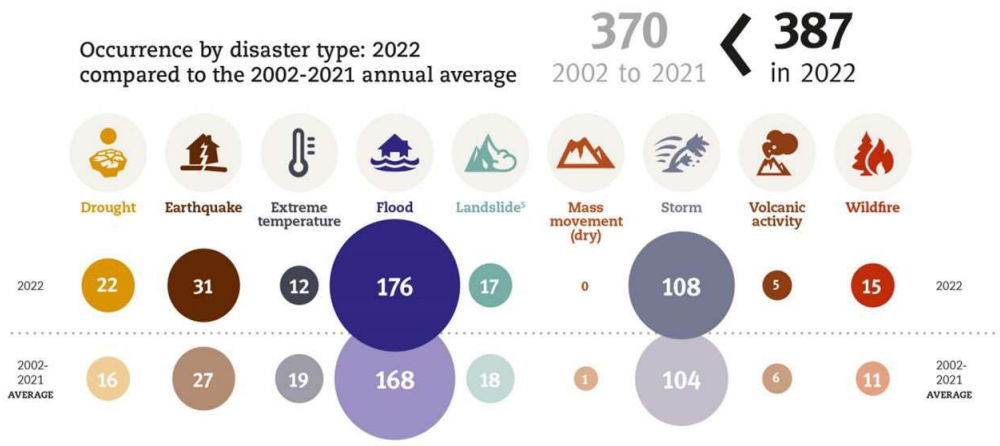


Fig. 1: Occurrence of natural disasters type of the 2022 in comparison with the average of the years 2001-2021. Data source: EM-DAT (2022).

Globally, the most commonly occurring disasters were those associated with floods (176) and storms (108). Nevertheless, an elevated degree of variability from the mean value of the period 2002–2021 was also observed in other types of disasters, such as droughts.

The EM-DAT 2022 report also highlights that Europe has witnessed a concerning rise in the occurrence of natural disasters in recent years, with an especially noticeable increase in the frequency of flood and storm events. In addition, the region has also experienced a rising number of disasters related to drought and wildfires. Specifically, the Mediterranean area has been affected by a significant increase in temperatures and a decrease in rainfall, leading to more frequent and

severe droughts and a higher risk of forest fires. In fact, it has been estimated that the frequency of wildfires has risen by 30% in the Mediterranean region since 1980, and this trend is projected to continue.

Therefore, the growing frequency and intensity of extreme events have raised awareness of the negative impacts that climate change can have on the environment and society. Therefore, a series of policies and measures are being implemented to mitigate its effects, including the adoption of renewable energy sources, the reduction of deforestation, and sustainable agriculture.

### 1.1 Risk assessment

Given the magnitude and cumulative impacts of repercussions from climate change and more generally from catastrophic events (natural and man-made catastrophes), disaster management—defined as a set of policies and techniques to avoid, minimize, or limit the risk—is crucial. The efforts are intended to lessen losses while boosting resilience. These approaches can be categorized as prospective disaster risk management, corrective disaster risk management, and compensatory disaster risk management (residual risk management), contingent upon whether the threat is current, potential, or residual, as outlined by the United Nations General Assembly in 2016. It is important to approach environmental sustainability and disaster risk reduction holistically, which necessitates the systematization of several gnoseological concepts and epistemological norms. There are intricate connections between problems like crises, resilience, intellect, and ecology. Effective risk mitigation requires taking into account the values and characteristics of numerous components and heterogeneous phenomena.

The concept of risk can be mathematically expressed as:

$$Risk = hazard\ x\ exposure\ x\ vulnerability \quad \text{Eq. 1}$$

As a result, it is possible to think of the risk from natural hazards as a combination of three essential factors: hazard, exposure, and vulnerability. According to the United Nations General Assembly 's 2016 definition of hazard, it is "a process, phenomenon, or human activity that may result in loss of life, injury, or other health impacts, property damage, social and economic disruption, or environmental degradation." Natural processes and occurrences are mostly linked to natural dangers.

While, exposure is the state of people, infrastructure, housing, manufacturing capabilities, and other tangibly held human assets in hazard-prone places.

Finally, vulnerability refers to an individual, a community, assets, or systems that are more susceptible to the effects of hazards when they are in a state, which is determined by physical, social, economic, and environmental elements and processes.

### 1.2 Normative framework

#### 1.2.1 International Climate Change Policies: an overview

According to the US government agency responsible for collecting and publishing climate data, the National Oceanic and Atmospheric Administration (NOAA), the concentration of $CO_2$ in the atmosphere exceeded 414 parts per million (ppm) in 2020. This is a level that has not been seen for at least 800 000 years (J. Blunden and Boyer, 2022; Jessica Blunden and Boyer, 2022). The increase in atmospheric $CO_2$ concentrations was one of the first effects considered when discussing climate change. In fact, during the 1980s and 1990s, the rise in $CO_2$ concentration in the atmosphere, along with the increase in greenhouse gas emissions resulting from human activities such as fossil fuel use and deforestation, and the associated

impacts such as global temperature increases, reductions in snow cover and sea ice, led the scientific community to establish a solid understanding of climate change.

One of the earliest actions taken in response to this understanding was the establishment of the Intergovernmental Panel on Climate Change (IPCC) by the World Meteorological Organization in 1988. The IPCC is an independent scientific body composed of experts from around the world who assess the scientific evidence on climate change and provide policy recommendations based on this evidence. The IPCC's scientific assessments are published in the form of reports, which are used as a basis for policy decisions and international climate negotiations.

An important step forward in the fight against climate change was taken in 1992 with the United Nations Framework Convention on Climate Change (UNFCCC), which aimed to establish an international framework for action to address climate change. Agenda 21 (https://www.un.org/esa/dsd/agenda21/res_agenda21_00.shtml ), a worldwide action plan implemented at the international, national, and local levels by United Nations system institutions, governments, and significant groups in every area where people have an influence on the environment, was also adopted during the 1992 Earth Summit in Rio de Janeiro.

However, awareness of the problem of climate change increased particularly from 2000 onwards, when the Kyoto Protocol came into force and there was a growing international commitment to tackling the issue. Adopted in 1997, the Kyoto Protocol was the first binding international agreement to reduce greenhouse gas emissions. It established emission reduction targets for developed countries and introduced the emissions trading mechanism, which allowed countries to offset their emissions by purchasing carbon credits from other countries. Although representing an important step in the fight against climate change, it also

highlighted the difficulties in involving all countries, as only developed countries were bound by emission reduction targets.

At the Millennium Summit in New York in 2000, the United Nations Member States overwhelmingly approved the Millennium Declaration. Eight Millennium Development Goals (MDGs) were established as a result of the Summit to end extreme poverty by 2015.

Political decisions on climate change have been made through a series of Conferences of the Parties (COP) of the UNFCCC, which have been held annually since 1995. The COPs have provided an opportunity for nations to discuss strategies for reducing greenhouse gas emissions and mitigating the effects of climate change.

One of the main COPs was COP21, held in Paris in 2015, which led to the adoption of the Paris Agreement, a binding international agreement that sets the goal of limiting the increase in global temperature to less than 2°C above pre-industrial levels, and pursuing efforts to limit the increase to 1.5°C. The Paris Agreement was ratified by 197 countries, representing an important step forward in the fight against climate change.

The Ageda 2030 common roadmap for world peace and prosperity for people and the earth was adopted that same year. The 17 Sustainable Development Goals (SDGs) are its basic tenets and are reported in Fig.2. The SDGs, which have their origins in the MDGs (2000-2015), replace them for the period 2015-2030 with the intention of addressing a wider range of global challenges, including social, economic, and environmental aspects, addressing, for example, climate change (goal 13), with an integrated approach, acknowledging the connections between different objectives and the need to address challenges in a comprehensive manner.


Fig. 2: The 17 sustainable development goals (SDG).
Data source: United Nations.

Subsequent COPs have seen nations commit to achieving the goals set out in the Paris Agreement. COP22, held in Marrakech in 2016, saw the adoption of a climate action proclamation, while COP23, held in Bonn in 2017, saw nations commit to strengthening climate action through increased efforts to reduce emissions and increase climate resilience.

COP24, held in Katowice in 2018, saw the adoption of a package of rules for the implementation of the Paris Agreement, establishing the modalities for monitoring and reporting greenhouse gas emissions. COP25, held in Madrid in 2019, was characterized by important discussions on outstanding issues of the Paris Agreement, such as financing for mitigation and adaptation to climate change.

COP26, held in Glasgow in 2021, was perhaps one of the most important climate change events in recent years. During the conference, nations committed to

increasing efforts to reduce greenhouse gas emissions and to providing financing for adaptation to climate change in the most vulnerable countries. In addition, the Glasgow Climate Pact was adopted, a set of decisions aimed at strengthening global climate action and implementing the Paris Agreement. These ambitious goals include limiting global warming, reducing greenhouse gas emissions, increasing climate financing, a greater commitment to climate adaptation, and support for innovation.

### 1.2.2 European Climate Change Policies

The international policy to combat climate change adaptation and achieve the goals of the Paris Agreement has been incorporated and implemented at the European level through the production of a series of regulations. In particular, the European Green Deal is a comprehensive plan of investments and actions aimed at making Europe the first continent to achieve net zero greenhouse gas emissions by 2050. The plan was presented by the European Commission in December 2019 as part of the EU's long-term strategy for climate neutrality. The European Green Deal is based on three main pillars:

a) Reducing greenhouse gas emissions by 55% by 2030 compared to 1990 levels and achieving net zero emissions by 2050. To achieve these goals, the plan includes a series of actions, such as reforming the EU's emissions trading system, increasing energy efficiency, increasing the share of renewable energy in the EU, and decarbonizing the transport sector.

b) Protecting nature and biodiversity, promoting sustainable agricultural practices, reducing the use of pesticides and fertilizers, protecting forests, and promoting biodiversity.

b) Creating a sustainable and inclusive economy, through the creation of new green jobs, investment in sustainable infrastructure, and promoting a fair and just transition to a net zero emissions economy.

c) The European Green Deal is integrated with the EU's emissions trading system (ETS), the Renewable Energy Directive, and the Energy Efficiency Directive. The ETS sets a cap on the total amount of greenhouse gas emissions that can be released by certain industries in the EU, while the renewable energy and energy efficiency directives set binding targets for the share of renewable energy in the EU's energy mix and for energy savings in member states. The EU also uses economic tools, such as fines, to enforce its regulations on climate change. The fines are based on the severity of the violation and can be substantial.

In the European policy, another noteworthy plan is the Mediterranean Action Plan (MAP), which is a specific program of the United Nation Environment Program (UNEP). The MAP was created in 1975 in response to the Mediterranean Sea's growing environmental problems. It was intended to encourage collaboration among Mediterranean coastal nations to address these issues jointly.

In 2015, the MAP underwent a substantial sea change when it unveiled its first Medium-Term Strategy (MTS 2016-2021). Targeting looming climate change and environmental sustainability concerns in marine habitats, this strategy laid forth an ambitious five-year plan.

The Mediterranean Strategy for Sustainable Development (MSSD) 2016–2025 was also introduced at the same time. This tactic strengthened the MAP's dedication to promoting sustainable development across the Mediterranean. It underlined the significance of striking a balance between economic development and environmental preservation, and it promoted spending on renewable energy, ethical fisheries management, and environmentally friendly tourism.

### 1.3 Essential climatic variables

The Global Climate Observing System (GCOS) was established in 1992 to ensure the collection and dissemination of information and observations necessary to address climate-related issues. This system was created in response to the statements made by the famous NASA scientist James Hansen to the United States Senate in 1988, in which he argued that human-caused global warming had already measurably influenced the Earth's climate (The New York Times, 1988 https://www.nytimes.com/1988/06/24/us/global-warming-has-begun-expert-tells-senate.html ). Four years after this key statement, the GCOS led to the identification of 55 essential climate variables (ECV) since 2003. The concept of ECV was introduced to identify a set of critical parameters for monitoring long-term climate trends and understanding the health of the climate system. ECVs have subsequently been recognized as an important tool for assessing the effects of climate change on Earth by the United Nations Framework Convention on Climate Change (UNFCCC) (Pettorelli et al., 2016; Bojinski et al., 2014).

ECVs are defined as physical, chemical, or biological variables, or a group of related variables, that critically contribute to the characterization of the Earth's climate. These variables are considered essential because they provide critical information on the health of the climate system and its ability to support life on Earth. ECVs have been grouped according to their physical interdependence and purpose of use. Each ECV has been selected based on its relevance to the climate system and its ability to provide essential information on the health of the system and climate trends. The principles adopted to select ECVs include the critical relevance of the variable to the climate system, the technical feasibility of observation or derivation on a global scale using proven methods, and the cost-effectiveness of generating and storing data on the variable.

ECVs have been classified into three main groups (Fig. 3): atmospheric, terrestrial, and oceanic. These groups reflect the major influences on the climate system and the role that essential climate variables play in providing critical information on the health of the system. For example, atmospheric ECVs include variables such as air temperature and greenhouse gas concentrations, while terrestrial ECVs include variables such as land cover and soil temperature. Oceanic ECVs, on the other hand, include variables such as sea surface temperature and salinity. In 2010, the soil moisture (SM) become one of the ECVs since it is a key variable for understanding a lots of process.

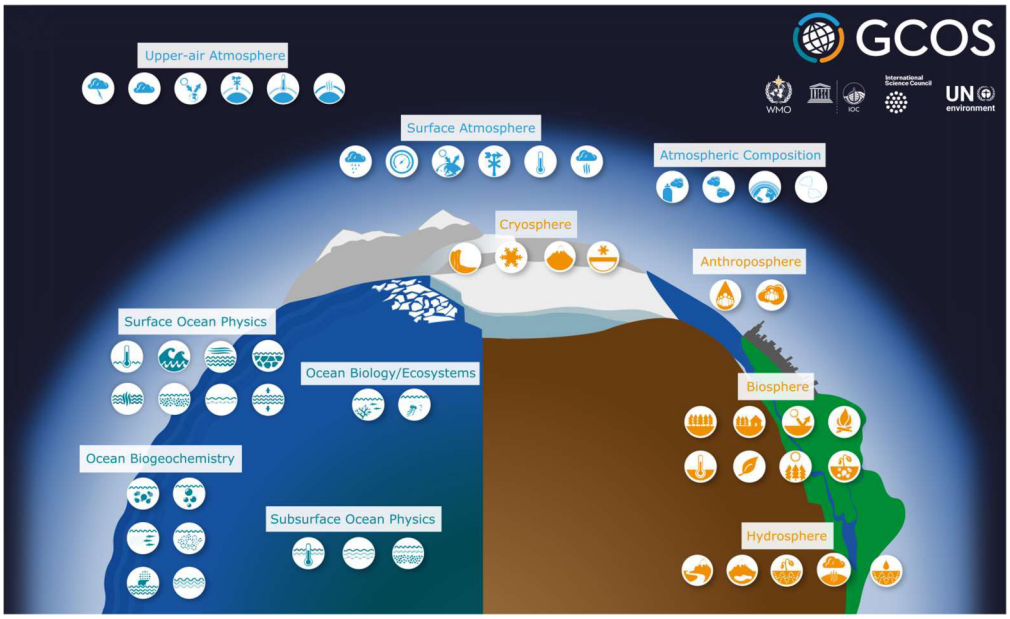


Fig. 3: Classification of the ECVs by GCOS. Data source: GCOS.

### 1.3.1 ECV of hydrosphere: the soil moisture

Water is the fundamental resource of our planet, without which life cannot exist. Approximately 97.2% of the water present on Earth is stored in the oceans, 2.15% in glaciers, and 0.63% in the land. SM, which is the water contained within the soil

up to the plant roots, constitutes only 0.005%. Despite the small reserves occupied by SM, it plays a fundamental role in many of the interactions that take place between the hydrosphere, biosphere, and atmosphere. Consequently, knowledge of SM and its variations is essential in studies that analyze the environment and its changes, in meteorology, hydrology, agrometeorology, and climatology.

In agronomy, an estimate of SM is important for the study of crop development during the initial phase of their growth (germination, development of the root system, etc.) since plant growth is generally conditioned by the amount of available water. In meteorology and climatology, the estimation of SM is particularly important because it directly influences the partitioning of energy between latent and sensible heat. In hydrological models, it is decisive in determining the division of meteoric waters between infiltration and runoff and for predicting the duration of drought periods.

Fig. 4 shows that although the role of SM is central in these fields of application, each of them requires a different spatial and temporal resolution. For climate and numerical weather prediction (NPW) applications, low spatial resolution and variable time resolutions (daily to monthly) are generally required. In the case of forest applications, the information should be below km but with a wide temporal resolution (weekly/monthly). Hydrological applications refer to a more variable spatial scale and a time scale below the day. Finally, applications for agriculture require a high spatial resolution (below 1 km) and a temporal resolution at least daily or weekly. These factors lead to the conclusion that a scale with a spatial resolution of 1 km and a daily temporal resolution would be appropriate for the different uses.

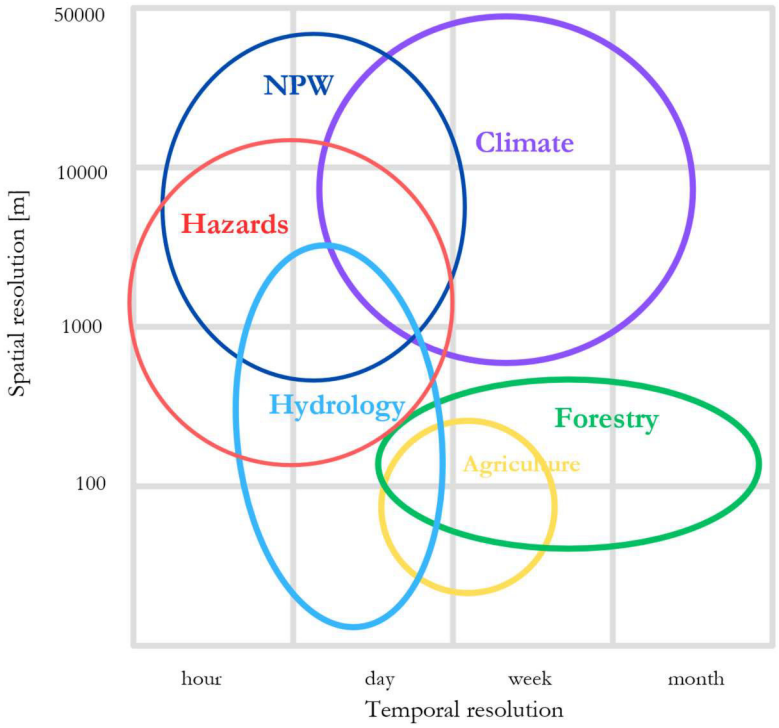


Fig. 4: Spatial and temporal resolution of the application fields in which is involved the SM.

Focusing on the reason why the SM is essential in so many applications we have considered the repercussions it induces. The most important effect is played on evapotranspiration, making SM a key variable for understanding water (Eq. 2) and energy balance (Eq. 3).

$$P = I + E + R + \Delta S \qquad \text{Eq. 2}$$

In the water budget equation, $\Delta S$ is the change of water content, P is the precipitation, E is the evapotranspiration, R is the surface runoff, and I is the infiltration rate. Note that the term $\Delta S$ includes SM, but can also encompass additional forms of water storage, such as surface water, snow, ice cover, and groundwater.

$$R_n = G + \lambda E + SH + \Delta H \quad \text{Eq. 3}$$

In the energy budget equation, $R_n$ is the net radiation, G is the ground heat flux, λE is the latent heat flux, SH is the sensible heat flux and **ΔH** is the change of energy. As we can see from both equations, the land energy and water balances are coupled through the evapotranspiration term (*E*, *λE*). Additionally, it is connected to a number of biogeochemical cycles (such as the carbon and nitrogen cycles) due to the coupling of photosynthesis and transpiration in plants. However, these impacts are only significant in areas where soil moisture is the primary determinant of evapotranspiration (Seneviratne et al., 2010).

Fig. 5 provides an overview of the main processes and feedbacks of the soil that will be analyzed in the Section 1.2.2.

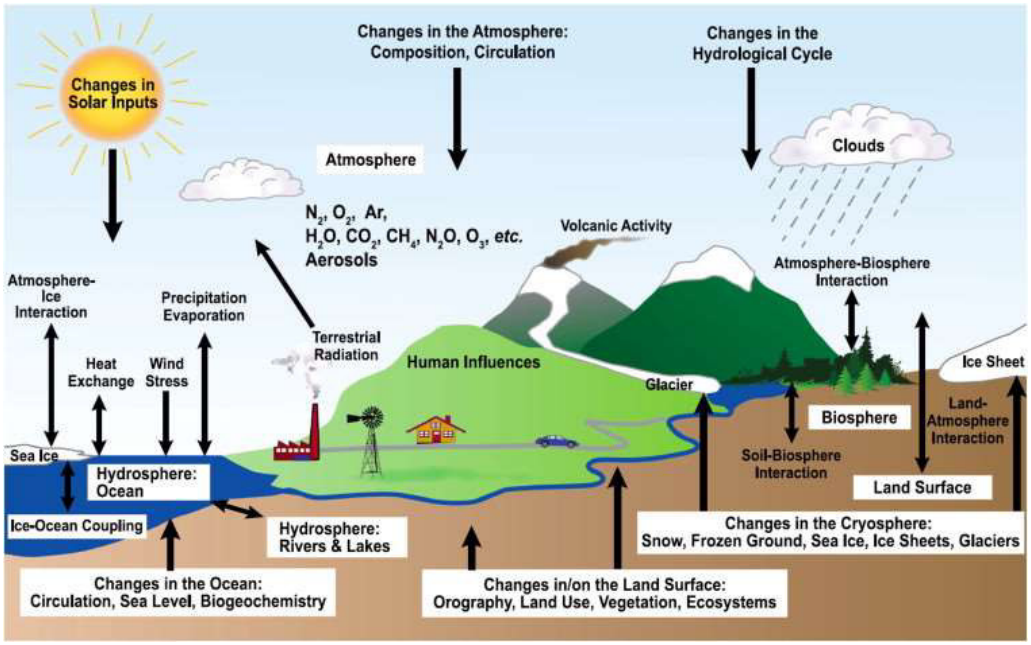


Fig. 5: Main processes and feedbacks of SM. Data Source: IPCC and others, 2013.

### 1.3.2 Feedback between SM and climate

Due to the cycles (water, energy, and biogeochemical) in which the SM is involved, it is subjected to a series of feedbacks, i.e., the possible retroactions of soil moisture on itself through the combination of its impact on variables and of the return impact of variables on soil moisture. These SM impacts are affected by the evapotranspiration (ET) in regime of soil moisture limitation, where the reduction in SM brings to a reduction in water available for plants and consequentially reduction in ET, since the SM is linked with the water potential in soil.

The classical hydrology is based on the theory of Budyko (1974, 1956), who presented the relation between the evaporative fraction (EF) and the SM with three zones, that is, dry, transition, and wet (Seneviratne et al., 2010; Teuling et al., 2009; Koster et al., 2004).

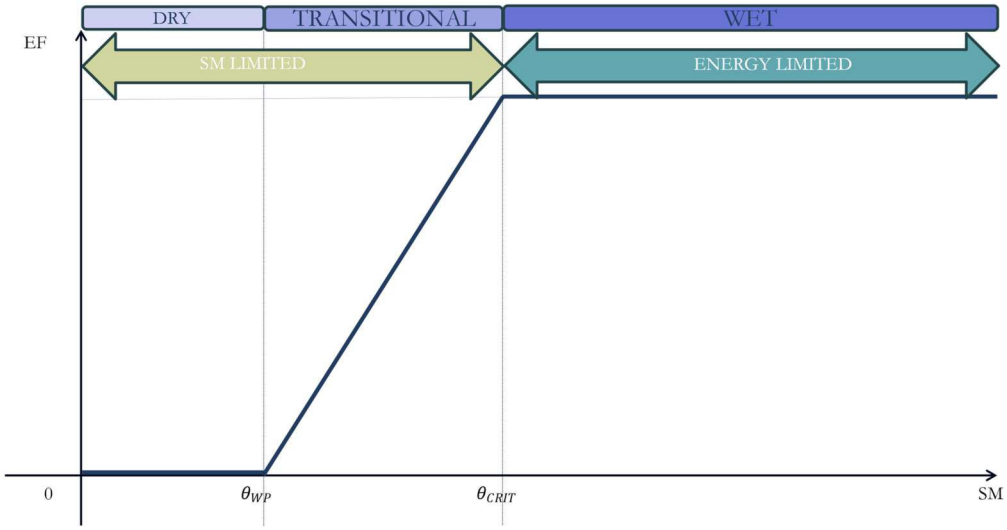


Fig. 6: Definition of the evaporative fraction (EF) and its maximum value (EFmax) as well as the accompanying soil moisture regimes and evapotranspiration regimes.

There are two basic evapotranspiration regimes that may be distinguished by the evaporative fraction: an energy-limited and a soil moisture-limited regime. The

evaporative fraction is independent of the soil moisture content under the energy-limited evapotranspiration regime, which corresponds to soil moisture values above a certain critical soil moisture value $\theta_{crit}$. A first-order limitation on evapotranspiration (soil moisture-limited evapotranspiration regime) is provided below $\theta_{crit}$ by soil moisture content. The wilting point ($\theta_{WP}$), below which no evapotranspiration occurs any longer, is another significant barrier. Please note that $\theta$ refers to a type of unit of measurements in which can be expressed the SM, i.e., in terms of volumetric water content (VWC). The other units will be detailed in the following (Section 1.2.3).

In light of the influence of soil moisture on evapotranspiration variability, three climate/soil moisture regimes can be distinguished: a wet climate regime $\theta > \theta_{crit}$, a dry climate regime $\theta < \theta_{WP}$, and a transitional climate regime $\theta_{WP} \leq \theta \leq \theta_{crit}$, where SM significantly limits evapotranspiration variability and the ensuing feedbacks to the atmosphere. The linear dependence of the variables (EF- SM) in transition regime is an approximation, however, Seneviratne et al. (2010) have reported that this dependence provides a good representation of the first order both in the land surface model (LSM) than in observations. In fact, only under transition regime both conditions i.e., the strong dependence of evapotranspiration on soil moisture and elevate average evapotranspiration are reached for a strong soil-climate coupling.

Precipitation (P) and temperature (T) are two factors that may have a significant influence on feedback, with the last causing heat waves. Naturally, we expect an increase in P to lead to an increase in SM, but this condition does not occur in very humid soils, where instead runoff is generated. All of this can result in negative feedback with an increase in ET and a consequent reduction in SM. However, in the case of a transitional regime, positive feedback occurs where an increase in SM leads to an increase in ET and an increase in P, which in turn leads to an increase

in SM. On the other hand, the reduction of SM could bring to a drying process with the reduction of ET and the increase in T. Finally, the increase in T may lead to the occurrence of a negative feedback with the increase in ET and the reduction of SM.

Moreover, there are other variables (e.g., albedo, vegetation) and feedback that make it complex to schematize the processes that occur, highlighting the centrality of SM in soil-atmosphere exchanges.

### 1.3.3 SM definition for measurements

According to Hillel (1998), the water that is typically referred to as SM is that present in the unsaturated soil zone. Only a very small portion of this water is typically substantial or clearly measured in connection to a certain volume of soil. The measure of the volume of water into the volume of soil is indicate as $\theta$ as follows:

$$\theta = \frac{\text{volume of water } [m^3]}{\text{volume of soil } [m^3]} \quad \text{Eq. 4}$$

In relation to its formulation $\theta$ varies from 0 to $\theta_{SAT}$ and can assume:

- Permanent wilting point ($\theta_{WP}$): This is the lowest water level to which the soil can go while still being in an equilibrium with gravity. Because the soil has such a low water content, plants can no longer properly draw water because the soil's water tension is too high. Water stress symptoms start to appear in plants, and they develop much slower.

- Critical ($\theta_{CRIT}$): a certain critical soil moisture value as said in the previous section (Section 1.2.2).

- Field capacity ($\theta_{FC}$): amount of water that the soil can retain after excess water is drained away under the effect of gravity. Plants are able to draw water from the soil for their requirements at this moisture level.

- Saturation ($\theta_{SAT}$): all soil pores are completely saturated with water. For the definition, $\theta_{SAT}$ could be at most equal to the porosity of the volume of soil considered.

Note that these quantities depend on soil characteristics such as soil texture (and on the kind of plant for the wilting point; see Hupet et al. (2005); Sperry et al. (2002)). Furthermore, the FC less the WP represents the maximum amount of water that may be made accessible to plants. Below the WP, the water is held too tightly by the soil matrix and is not available to plants (Hillel, 2003).

Using $\theta_{SAT}$, a further common definition of soil moisture is the saturation ratio $\theta_S$, which varies between 0 and 1:

$$\theta_s = \frac{\theta}{\theta_{SAT}} \qquad \text{Eq. 5}$$

In the remaining part of this manuscript, to indicate SM saturation, we will use "s" for simplicity.

The FC and WP led us to the possibility to define the soil moisture index (SMI) as follows:

$$SMI = \frac{\theta - \theta_{WP}}{\theta_{FC} - \theta_{WP}} \qquad \text{Eq. 6}$$

Thus, the SMI (which ranges from 0 and 1) is a measurement of the soil moisture content as a proportion of the total storage accessible to plants. It should be noted that under some conditions, real soil moisture may exceed the field's tolerance (for

example, during periods of high precipitation or in saturated riverbank regions). The SMI may be adjusted to 1 for any number over FC to get around this problem.

Define SM in absolute term express S [mm] with the considered soil depth (d, with constant cross section).

$$S = \theta \cdot d \qquad \text{Eq. 7}$$

Finally, the soil moisture potential $\psi$ can be used to indicate SM for describing how soil moisture binds to the soil matrix. According to standard definitions, SAT, FC, WP correspond respectively to soil moisture potentials of 1 hPa, about 100–300 hPa, and around 15,000 hPa (1.5 MPa). Accordingly, the corresponding suction heads (negative pressure heads) are 1 cm, 1-3 m, and 150 m.

These definitions are significant especially in the context of ground measurements since most measures of soil moisture are indirect (e.g., dielectric constant, changes in the gravitational field, or soil suction), and are often only connected to one definition of SM.

### 1.3.4 SM along profile: SSM vs RZSM

The definitions provided in Section 1.2.3 have highlighted the significance of soil volume, with particular emphasis on the importance of constant soil section thickness (d). While processes involving SM have been extensively discussed, it is imperative to distinguish between moisture in the surface soil layer, referred to as Surface Soil Moisture (SSM), and that in the deeper layer, termed Root Zone Soil Moisture (RZSM). SSM pertains to a depth of a few centimeters (up to 10 cm), depicted as Soil "A" in Fig. 7, representing the water content that predominantly interacts with the atmosphere. Conversely, RZSM is referenced at a greater depth (up to 1 meter, equivalent to the unsaturated zone depth), Soil "B" in Fig. 7) and constitutes the pivotal water source from which plants draw sustenance. However,

precisely determining RZSM, as elaborated in Chapter 2, presents challenges often addressed through modeling. Nonetheless, its accurate determination holds paramount importance in the agricultural domain, as expounded upon later in the chapter, enabling optimal assessment and planning of water requirements, thereby maximizing available resources and mitigating potential calamities.

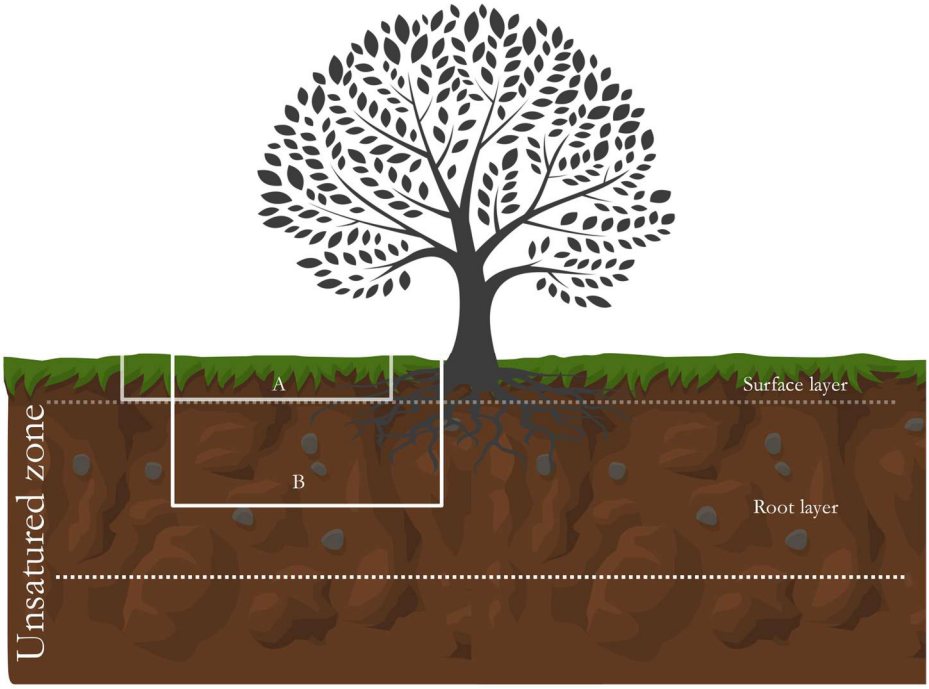


Fig. 7: Distinction of the unsatured zone into a surface layer and deepen layer.

## 1.4 Purpose

The ongoing climate change presents an urgent global challenge, with far-reaching impacts on ecosystems and humanity. Extreme weather events, floods, droughts, and landslides are just a few of the effects induced by climate change, all intricately connected to soil water resources and alterations in its absorptive capacity.

In the following chapter, we will explore various measurement methodologies. While point measurements offer precision, they are costly and intricate to extrapolate spatially. Satellite-based microwave techniques enable synoptic global coverage and excellent measurement repeatability. Nevertheless, a distinction should be made between products with high spatial resolution and those emphasizing temporal resolution. Hydrological modeling, on the other hand, offers solid backing, despite being inextricably linked to model assumptions and input data.

Cramer et al. (2018) revealed that the Mediterranean basin faces a heightened risk of climate and environmental changes surpassing global averages in both extent and rate. This is due to a convergence of local factors, such as land use changes, and global influences propagating through the Mediterranean basin via diverse teleconnection modes (Lionello et al., 2014).

Mitigating the underlying processes of climate and environmental changes and adapting to their inevitable consequences stand as paramount priorities for public and private stakeholders shaping the future of Mediterranean communities and environmental integrity. Such attempts demand research that goes beyond what is already known. Currently, several challenges and needs are evident in the Mediterranean context: the MAP identifies an observational data and monitoring system disparity between the North, South and East regions, prompting an increase of observations and network establishment.

The aim of this thesis is to provide an overview of SM measurements within the European zone encompassing the Mediterranean area, focusing particularly on microwave remote sensing measurements. Subsequently, the goal is to develop a high spatial and temporal resolution product (with a daily interval and 1 km resolution), offering a comprehensive four-dimensional depiction of soil profiles. This product aims to contribute to climate change mitigation efforts.

*Chapter 2*

# STATE OF THE ART: SOIL MOISTURE MEASUREMENT TECHNIQUES

This section is going to provide an overview of the unique properties of SM and its fundamental relationships with soil and water. Thus, the focus has been shifted to a comprehensive analysis of the applications of measurement techniques in the field of soil moisture observation.

## 2.1 The role of soil moisture

SM, as an integral component of the three-phase soil system, plays a fundamental role in various applications. In fact, it is a key element of the surface water balance, which controls numerous processes that occur at different temporal and spatial scales within the climate system (Baldwin et al., 2019; Manfreda et al., 2011; Rodríguez-Iturbe et al., 2006). SM is essential for plant transpiration and photosynthesis, it exerts influence over water, energy, and biogeochemical cycles, and contributes to natural hazard triggers such as droughts, floods, and landslides, owing to its significant role in regulating outflow dynamics and infiltration patterns (Albano et al., 2017; Chen et al., 2017; Miralles et al., 2012; Seneviratne et al., 2010; Koster et al., 2004).

The computation of SM considers the variation of this parameter across different volumes of soil. Due to its uneven distribution both vertically and horizontally, the measurement of SM exhibits variability based on the specific volume under consideration (Seneviratne et al., 2010). This variability holds significant implications for comparing different measurement methods. Furthermore, achieving a robust and accurate estimation of SM, along with its spatiotemporal

fluctuations, should ensure significant advantages in the large-scale monitoring of the effects induced by extreme meteorological events of climate change. Despite the considerable advancements made over time, the absence of an operational system capable of monitoring SM variations at the necessary spatial and temporal resolutions for various applications continues to be a challenge. Many applications, in fact, require frequent observation estimates, typically on a daily basis and over expansive areas (Schmugge et al., 1980).

However, measurement of SSM using conventional methods in large regions presents difficulties and high costs. The precise measurements obtained from distributed stations across the terrain provide data that span from a few centimeters to a few hundred meters at best (Fig. 8). Furthermore, these stations exhibit spatial heterogeneity, thereby complicating the straightforward reconstruction of the measured parameter (Jackson et al., 1981). This complexity arises due to the substantial variability present in the data sought for interpolation.

Given the challenges associated with directly assessing the spatial distribution of SSM through specific measurements, hydrological models are frequently employed (Jackson, 1986). Unfortunately, these models rely on extensive sets of meteorological data (which can be arduous and costly to acquire) and parameters that are often challenging to estimate accurately or are prone to significant errors (Walker and Houser, 2002; Wood et al., 1993).

During the past two decades, the application of remote sensing (RS) techniques (both spaceborne and airborne) to measure SSM and its variations has gained much attention. These techniques generally facilitate coverage of expansive regions with varying time intervals, contingent on the satellite platform employed. Nevertheless, a primary limitation of this approach lies in the challenge of reconciling high-frequency temporal measurements with adequately precise spatial resolution measurements, especially in cases where freely available data products are utilized.

Furthermore, these measurements solely pertain to the uppermost soil layers, which are most susceptible to weather conditions and may not accurately reflect the overall soil wetness state.

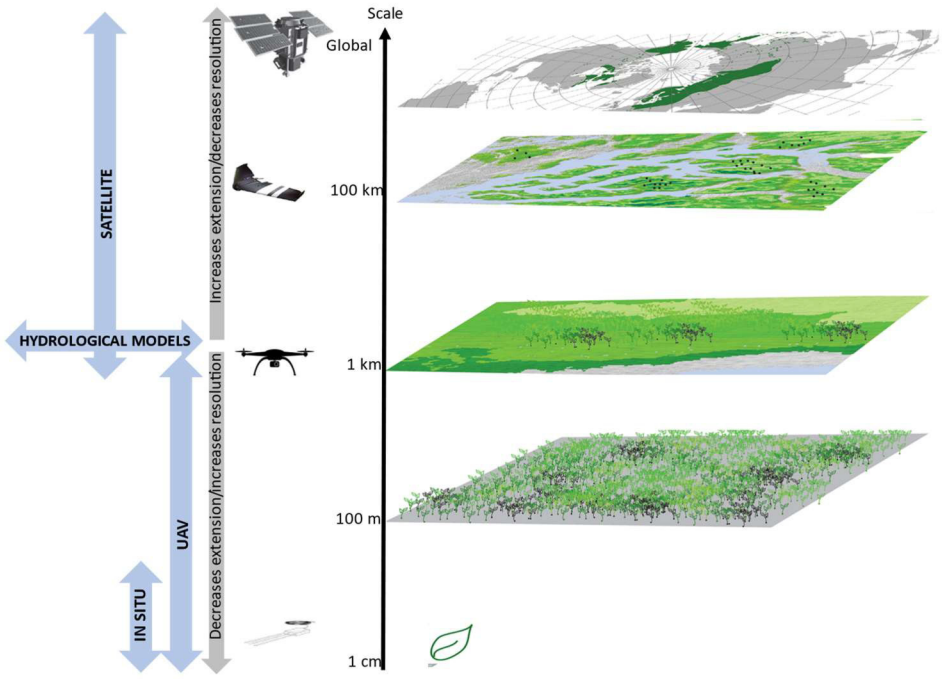


Fig. 8: Types of SM measurements (in situ, hydrological modelling, and remote sensing) their relationship with the spatial resolution.

Therefore, each approach comes with its distinct advantages and drawbacks, yet its integration typically yields optimal results in retrieving SM information (Lacava et al., 2013; Walker and Houser, 2002; Schmugge et al., 1980). Ground-based measurements hold the potential for exceptional accuracy and are, thus, well-suited for calibrating and validating hydrological models that provide insights into the vertical distribution of SM across the soil profile. On the other hand, satellite measurements offer a momentary glimpse into ongoing processes at specific

instances, thereby serving as valuable snapshots of dynamic conditions at a given point in time (Walker and Houser, 2002).

### 2.2 Water-soil relationship

Rainfall, snowfall, frost, and fog contribute water to the soil. However, only a portion, influenced by permeability, can infiltrate the soil. Once inside, its residence time is determined by the soil's physical-chemical attributes, biological processes, and temperature. The latter factor can impact water losses due to evaporation. Water's duration in the soil and its movement within it hinge on the forces affecting the water volume within the soil.

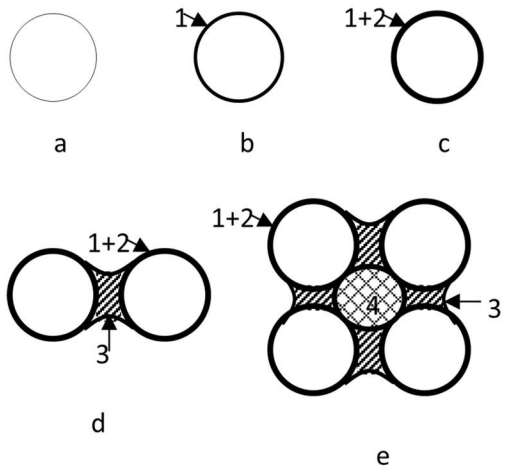


Fig. 9: Types of water in rocks: (1) hygroscopic water; (2) pellicular water; (3) capillary water; (4) gratifying water. Data Source: Casadio and Elmi, 2000.

The primary acting forces encompass surface adhesion forces, surface tension forces, and gravitational forces. Gravitational force is linked to the constant "g" and propels the water vertically downward. Surface adhesion force acts on the layer of water molecules on a colloid's surface, where dipoles orient themselves based on the polarity of the electronegative field from organ-mineral cells. Surface tension forces, also known as capillary forces, are akin to those generated within a

capillary tube, leading to the formation of two menisci - one internal and one external. In this scenario, water circulates within micropores (diameter <10 mm). For instance, when a micropore is filled with water between 50% and 75% and transitions into a macropore filled with air, two menisci emerge: one at the air-to-water interface inside the micropore and the other at the micropore's outer end. This gives rise to distinctions between "gravitational," "capillary," "film," and "hygroscopic" types of water based on these factors.

Hygroscopic water (Fig. 9b) is the water in contact with soil colloids, forming a layer up to 0.1 $\mu$m thick. It is not available for use by plants and can be extracted only by drying the soil at 105°C for 24-48 hours. Pellicular water (Fig. 9c), closely associated with hygroscopic water due to adhesion, can be removed through centrifugation and is found in layers of around 1-2 $\mu$m thickness. Once the needs for pellicular water are met, capillary water is held within the narrower pores (Fig. 9d), defying the force of gravity. This phenomenon is a result of capillarity, which arises from the interplay between adhesion and cohesion forces. A portion of capillary water, located in pores with a diameter less than 0.2 $\mu$m, remains unavailable to plant roots. However, the capillary water in pores with a diameter between 0.2 and 10 $\mu$m, although moving relatively slowly, is accessible for root uptake. The combined content of hygroscopic, pellicular, and capillary water is collectively termed retention water.

As the diameter of micropores expands, particularly exceeding 30 $\mu$m, surface tension forces diminish. Consequently, the water's movement becomes more influenced by gravity (Fig. 9e), promoting downward movement and depleting water from surface layers that are explored by roots and heavily influenced by biological components.

Macropores possess diameters that prevent capillary retention of water, effectively holding only air and excluding any water vapor present. Higher levels of water vapor elevate the likelihood of its condensation onto colloidal surfaces, forming a "hygroscopic" water layer.

### 2.3 Dielectric properties of soil

As mentioned, several methods for measuring SM exist, and some of these leverages the dielectric properties of the soil, particularly the distinction between the dielectric properties of soil and water. These properties are quantified using the dielectric constant or permittivity (ε), which characterizes how a specific material reacts to the presence of an electromagnetic field (Schmugge, 1983). Essentially, it signifies the resistance or permission that a material presents to the propagation of an electric field within it.

$$\varepsilon = \varepsilon' + \varepsilon'' \qquad \text{Eq. 8}$$

$\varepsilon$ consists of a real part $\varepsilon'$, which describes the propagation of the wave within the material (e.g., velocity) and an imaginary part $\varepsilon''$, which describes the loss of energy resulting from the material crossing (Engman and Chauhan, 1995; Topp et al., 1980). Usually, it is expressed by reference to the dielectric constant measured in empty space:

$$\varepsilon_{r=} \varepsilon_{/} \varepsilon_0 \qquad \text{Eq. 9}$$

Nevertheless, for the sake of simplicity we will refer to $\varepsilon_r$ as ε.

Fig. 10 depicts, on the left side, the plots of the real part ε' and the imaginary part ε" of the dielectric constant as they vary with different soil types, measured at a frequency of 1.4 GHz (Ulaby, 1986). On the right side, the graphs illustrate their trends (the upper part for the real part and the lower part for the imaginary part)

concerning frequency (in Hz) and temperature (in ºC) (Hoekstra and Delaney, 1974).

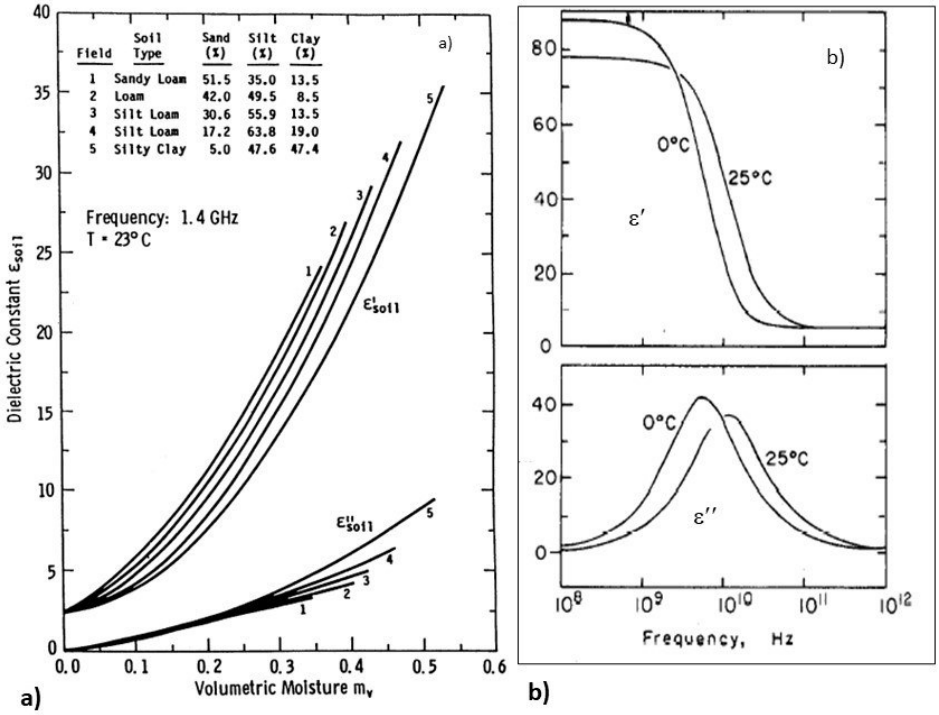


Fig. 10: (a) Variation of the $\varepsilon'$ and the $\varepsilon''$ for 5 different soils as a function of water content at 1.4 GHz (Ulaby et al., 1986); (b) Variation of the real the real $\varepsilon$ " and complex part $\varepsilon''$of the dielectric constant of water as a function of frequency (Hoekstra and Delaney, 1974).

Ulaby et al. (1982) emphasized the frequency-independence of ε' for dry soil, where ε' varies between 2 and 5, and ε" remains below 0.05. The distinct behaviors observed among different soil types arise from varying water content, porosity (Njoku and Entekhabi, 1996), and differing levels of porosity. In contrast to the behavior of free water at approximately 1 GHz, the real part of the dielectric constant exceeds 80, and the imaginary part is around 4 (Ulaby et al., 1996) (Fig. 10b). This increase in the case of free water is due to the polar nature of water

molecules, causing their electric dipoles to align with the direction of the electric field. Consequently, this results in enhanced electrical shielding and a significantly elevated ɛr value for water (Engman and Chauhan, 1995).

The significant increase in the dielectric constant, up to 20 times, has enabled the measurement of SM through the phenomenon of dielectric mixing within the soil. However, the presence of different types of water in the soil (gravitational or free water and water retention) leads to variations in dielectric permittivity. Specifically, retention water has a lower ɛ compared to free water due to the immobilization of water molecules absorbed on particle surfaces (Njoku and Entekhabi, 1996; Jackson and Schmugge, 1989; Wang and Schmugge, 1980). The dielectric mixing models introduced in the scientific literature, briefly reviewed, account for various contributions and recognize that the polarization of water molecules hinges on factors such as observation frequency and soil temperature (Heimovaara, 1994; Ulaby, 1986; Topp et al., 1980). For instance, ɛr decreases due to the disruption of dipole alignment resulting from thermal agitation.

It is essential to clarify that the study of dielectric mixing is intricate due to the non-linearity of the mixture, which does not correspond to a simple weighted average of its individual components. Topp et al. (1980) proposed an empirical multiple regression relationship between SM and the real part of dielectric permittivity (ε') valid within the frequency range of 1 MHz to 1 GHz:

$$\varepsilon' = 3.03 + 9.3\theta + 146.0\theta^2 - 0.76\theta^3 \qquad \text{Eq. 10}$$

$\theta$ is the water content.

The notable advantage of this formulation is its independence from soil density, texture, and salinity when considering the real part of the dielectric constant. On the contrary, the empirical model put forth by Wang and Schmugge (1980) for

describing the dielectric constant of a soil-water mixture within the frequency range of 1.4 to 5 GHz is built upon the known dielectric constants of air, ice, soil, and water. It also takes into account the respective volume fractions occupied by these constituents. The researchers identified a threshold of water content for each soil type (lower for sandy soils and higher for clay soils), marking a transitional point beyond which the dielectric constant rises sharply. Depending on whether the water content is above or below the threshold of the transition zone, the applicable formulas are denoted as (a) and (b), respectively:

$$\text{a) } \varepsilon = \theta\varepsilon_x + (P - \theta)\varepsilon_a + (1 - P)\varepsilon_r \quad \text{Eq. 11}$$

$$\varepsilon_x = \varepsilon_i + (\varepsilon_w - \varepsilon_i)\frac{\theta}{M_t}\gamma \quad \text{Eq. 12}$$

$$\text{b) } \varepsilon = \theta\varepsilon_x + (\theta - M_t)\varepsilon_w + (P - \theta)\varepsilon_a + (1 - P)\varepsilon_r \quad \text{Eq. 13}$$

$$\varepsilon_x = \varepsilon_i + (\varepsilon_w - \varepsilon_i)\gamma \quad \text{Eq. 14}$$

Where $\varepsilon_a$, $\varepsilon_w$, $\varepsilon_r$, $\varepsilon_i$ are respectively the dielectric constant of air, water, rocks and ice, while $\varepsilon_x$ is the dielectric constant of the absorbed water; P is the porosity of the dry soil; $\theta$ and $M_T$ respectively are the water content and the transition water content; finally, g is an experimental parameter.

The core concept underpinning this model is that the initial water that comes into contact with the ground is firmly adsorbed onto the surface of soil particles, hindering dipole rotation. As more water is introduced, it gains the ability to align freely. The transition from absorbed to free water is influenced by the soil's particle size: clayey soils exhibit higher absorption compared to sandy soils. Several other

models have been presented to describe dielectric mixing. For example, Hallikainen et al. (1985) used polynomial expressions in the frequency range 1,4-18 GHz:

$$\varepsilon = (a_0 + a_1 S + a_2 C) + (b_0 + b_1 S + b_2 C)\theta + (c_0 + c_1 S + c_2 C)\theta^2 \quad \text{Eq. 15}$$

With S and C, respectively, the percentage of sand and clay.

Indeed, Dobson et al. (1985) introduced both a semiempirical model and a theoretical model for describing dielectric mixing. The theoretical model dissects the soil-water mixture into two components: a portion of volume occupied by water retention, and another occupied by free water. This division aligns with the composition of the soil. The model employs a multiphase formula applicable to mixtures containing randomly orientated inclusions:

$$\varepsilon = \frac{3\varepsilon_s + 2V_{fw}(\varepsilon_{fw} - \varepsilon_s) + 2V_{bw}(\varepsilon_{bw} - \varepsilon_s) + 2V_a(\varepsilon_a - \varepsilon_s)}{3 + V_{fw}\left(\frac{\varepsilon_s}{\varepsilon_{fw}} - 1\right) + V_{bw}\left(\frac{\varepsilon_s}{\varepsilon_{bw}} - 1\right) + V_a\left(\frac{\varepsilon_s}{\varepsilon_a} - 1\right)} \quad \text{Eq. 16}$$

with s, $f_w$ and $b_w$ and a which indicate soil, free water, retention water and air, respectively. $V_i$ indicates the fraction of volume occupied by inclusions.

On the other hand, the proposed semiempirical model expresses the two components of the dielectric constant in the range 1.4-18 GHz as a function of soil temperature, soil moisture content, texture, and frequency of observation. Peplinski et al. (1995) have extended the previous model of Dobson et al (1985) validating it over the entire frequency range between 0.3 and 18 GHz. These are still the most widely used methods to describe dielectric mixing.

### 2.4 Ground-based measurements of soil moisture

The systematic monitoring of ground-based SM started in the 1930s within the Ex Soviet Union and subsequently extended to Mongolia, China, India, and Eastern Europe. In the United States, the first organized observations were established in

1980 (Robock et al., 2000; Hollinger and Isard, 1994). Various measurement techniques capitalize on monitoring stations and can be categorized as follows:

- Resistance-Based Methods: methods which involve resistance measurements, exemplified by the tensiometer.

- Capacitance-Based Methods: category which encompasses techniques utilizing electrical capacitance, such as the electrical capacitance probe (EC).

- Time-Domain Reflectometry (TDR) and Frequency-Domain Reflectometry (FDR): methods that are grounded in reflectometry principles and include both time-domain and frequency-domain variants.

- Radiation Measurements-Based Methods: techniques that rely on radiation measurements are incorporated here, including sensors like the gamma radiation sensor and the neutron radiation sensor.

The following are brief descriptions of some of the measurement approaches mentioned.

### 2.4.1 Tensiometer

Given the complex interactions of the soil forces, as mentioned above (Section 2.2), it is often more convenient to describe the movement of water within the soil referring to the energy released per unit of water than to the dominant forces. The resistance method uses the concept of water potential in a porous medium. This concept facilitates assessment of the state of water over time through the integrated system of soil, plant and atmosphere. This shift to potential-based characterization replaced the previous classifications that classified various forms of water in the soil (such as gravity water, capillary water, and hygroscopic water). By using this potential approach, we can better understand the water dynamics in soil.

$$\psi_t = \psi_g + \psi_p + \psi_o \quad \text{Eq. 17}$$

The Committee on Terminology of the International Society of Soil Science (ISSS) (Hillel, 2003) has precisely defined the total potential of water in soil as the work required, per unit quantity of pure water, to transport an infinitesimal amount of water reversibly and isothermally from a container of pure water, at a fixed elevation and atmospheric pressure, to the soil water at the specific point under consideration.

The tensiometer is constructed with a porous cup, often made of ceramic with very fine pores, linked to a vacuum gauge through a rigid tube filled with water. When the soil matrix potential is lower (more negative) than the pressure equivalent within the tensiometer cup, water moves from the tensiometer, driven by a gradient of potential energy, through the saturated porous cup and into the soil. This movement creates an aspiration detected by the gauge. Water continues to flow in the soil until equilibrium is established, and the aspiration within the tensiometer equals the soil's matrix potential, indicating dissipation of the driving force. In wet soil conditions, the flow can reverse, with groundwater entering the tensiometer until a new equilibrium is reached (S.U. et al., 2014; Or, 2001).

Primary advantages of the tensiometer include its high accuracy in measuring soil moisture at low water potentials and its sensitivity to changes in soil moisture within the range relevant to plant-water relationships. However, regular maintenance is required to prevent clogging of the tensiometer pores. This method has limitations when dealing with frozen or freezing soils, as well as challenges when measuring in soils with low water retention capacity.

### 2.4.2 Time Domain Reflectometry

Time Domain Reflectometry, TDR, has been widely used over time (Rao and Singh, 2011; Robinson et al., 2008; Hilhorst, 2000). It is based on the dielectric

capacities of the soil according to the modelling proposed by Topp et al. (1980). By inverting the Eq. 10 we obtain:

$$\theta = 4.3x10^{6}(\varepsilon')^{3} - 5.5x10^{-4}(\varepsilon')^{2} - 2.92x10^{-2}\varepsilon'^{-} 5 - 3x10^{-2} \quad \text{Eq. 18}$$

As extensively detailed in the Section 2.3, the variance between the dielectric constants of water and the other constituents of the soil leads to the dependence of the travel time of electromagnetic pulses on θ. Consequently, time-domain reflectometry (TDR) measures the delay between incident electromagnetic pulses and reflections propagating within the soil.

Originating from the formulation established by Topp et al. (1980), which underpins the operation of conventional TDR, Hilhost et al. (2000) introduced a modification to factor in porosity. This adjustment aimed to achieve a more precise determination of the real part of the dielectric constant (ε') and subsequently θ.

TDR boasts notable advantages including high temporal resolution, rapid data acquisition speed, and substantial availability of information. Moreover, it permits unattended operation, facilitating the recording of data over time without requiring constant supervision (Evett and Steiner, 1995). The effectiveness of TDR is well-established up to a frequency of 1 GHz. Topp et al. (1982) conducted a laboratory study using a 1-meter depth of loam clay soil and demonstrated that the variation from the gravimetric method (a destructive laboratory technique) was merely 3%. This finding underscores the accuracy of the TDR measurements. These probes are available in both mobile and stationary forms, and they can vary greatly in cost. The former is primarily utilized for agricultural applications. Mittelbach et al. (2012) conducted a comparison between three inexpensive sensors and one pricier. The less expensive sensors exhibited inconsistent performance, sensitivity limitations under certain humidity conditions, and spurious sensitivity to temperature changes. Nonetheless, there are some challenges associated with TDR. Repetitive

measurements are often required, leading to potential time consumption. Additionally, this type of measurement is more applicable on a smaller scale due to its localized nature (Schwartz et al., 2008). Another aspect is the estimation of θ through TDR, where the primary source of uncertainty has historically been associated with the determination of propagation time (Hook and Livingston, 1996; Pepin et al., 1995). However, more recent studies have shown that this type of probe can also be used to deduce other soil parameters, including dry density, porosity, and saturation (Rohini and Singh, 2004). This highlights the expanding utility and potential of TDR beyond its original scope.

### 2.4.3 Frequency Domain Reflectometry

The abbreviation FDR stands for Frequency Domain Reflectometry, a technique utilized to assess SM by exploiting the dielectric properties of the soil. Specifically, FDR determines the soil's dielectric constant by measuring the time it takes to charge a capacitor, with the soil acting as the dielectric medium (Minet et al., 2010; Robinson and Dean, 1993). This method is based on the principle that the dielectric constant of the soil affects the charging time of the capacitor. In FDR measurements, the equipment comprises two electrodes that form a capacitor, with the soil acting as the dielectric material. The soil's dielectric properties influence the time it takes for the capacitor to charge and discharge, creating an oscillating circuit. This circuit responds to variations in water content within the soil at frequencies ranging from 10 to 150 MHz. FDR's working principal shares similarities with TDR (Time Domain Reflectometry), as both methods involve sending signals through the soil and measuring their interactions. However, FDR distinguishes itself by utilizing a scanning frequency approach. This allows for rapid and non-destructive data collection across a wide frequency spectrum.

Lin (2003)demonstrated that while FDR's operation is akin to TDR, FDR often yields more accurate results. This observation was further supported by Rao and

Singh (2011), who established that FDR outperforms TDR when dealing with soils containing less than 5% volumetric moisture content. Therefore, FDR exhibits increased sensitivity, particularly in drier soil conditions.

### 2.4.4 Neutron diffusion and gamma ray techniques

Among the radioactive techniques commonly employed for soil moisture measurement, two prominent methods are the gamma radiation and neutron diffusion technique (S.U. et al., 2014). The neutron diffusion technique involves the use of a fast neutron source with an energy level around 5 MeV and a slow neutron detector with an energy level of about 0.025 eV at 27 ° C. Despite its efficacy in measuring a substantial soil volume, this technique carries inherent risks (Jarvis and Leeds-Harrison, 1987). Neutron diffusion methods come in two forms: surface probes and cylindrical probes designed to penetrate deeper into the soil. The latter are particularly valuable for agricultural and environmental applications.

Gamma radiation offers high-resolution measurements with a quick response time of approximately 1 minute. However, this methodology can be influenced by fluctuations in the apparent density of the soil, which can affect the accuracy of soil moisture measurements. While gamma radiation provides a non-destructive approach, it presents substantial limitations linked to its cost and the potential hazards associated with the emitted radiation. Notably, the level of radiation emitted by gamma radiation techniques is significantly higher compared to that of neutron diffusion techniques.

## 2.5 Microwave remote sensing technique

Numerous studies have demonstrated the feasibility of estimating SSM using remote sensing (RS) techniques. Among these techniques, those that utilize microwave (MW) frequencies have achieved significant success. Microwave Earth Observation (EO) leverages the electromagnetic radiation within the frequency range between 1 mm and 1 m on the electromagnetic spectrum. This range is

further subdivided into distinct bands, each designated by a specific letter (refer to Table 1).

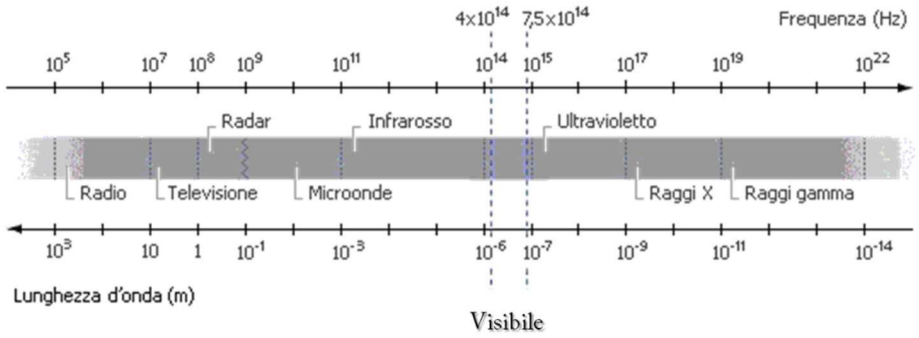


Fig. 11: Electromagnetic spectrum.

Table 1: Wavelength and frequency for each band in which the MW is subdivided.

| Band Designation | Wavelength (cm) | Frequency (GHz) |
|---|---|---|
| $K_a$ | 0.75 – 1.10 | 40.0 – 26.5 |
| K | 1.10 – 1.67 | 26.5 – 18.0 |
| $K_u$ | 1.67 – 2.40 | 18.0 – 12.5 |
| X | 2.40 – 3.75 | 12.5 – 8.0 |
| C | 3.75 – 7.50 | 8.0 – 4.0 |
| S | 7.50 – 15.0 | 4.0 – 2.0 |
| L | 15.0 – 30.0 | 2.0 – 1.0 |
| P | 30.0 – 100 | 1.0 – 0.3 |

In MW we distinguish between two main remote sensing system measurements made by active sensors (radar) and passive sensors (radiometers). The difference between them lies in the different sources of energy. All matter at a temperature above absolute zero emits electromagnetic radiation due to the motion of charged particles of its atoms and molecules (De Troch et al., 1996). Active sensors measure the electromagnetic radiation reflected (retrodiffuse) by the object being observed,

radiated by a source of energy artificially generated by the sensor itself (Sharkov, 2003), and defined by the backscatter coefficient.

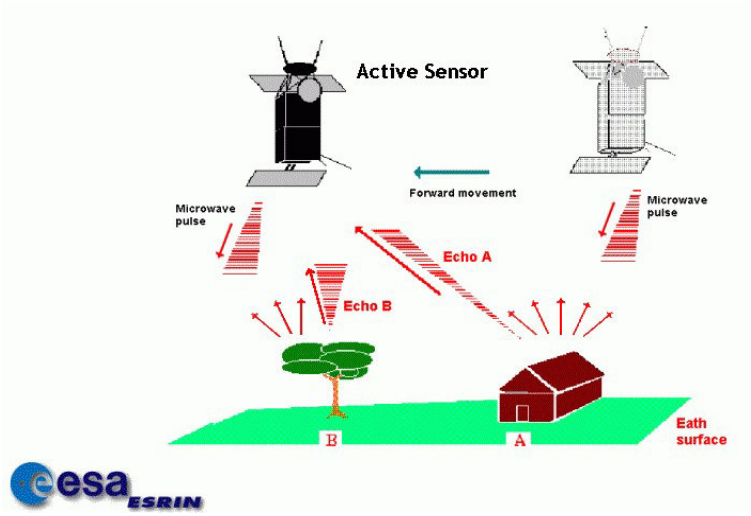


Fig. 12: Operation of active sensor according to European Space Agency. Data Source: https://www.esa.int/SPECIALS/Eduspace_IT/SEMTZSZRA0G_0.html.

Passive sensors or MW radiometers measure the emission properties of the object of observation, resulting from its characteristics and temperature.

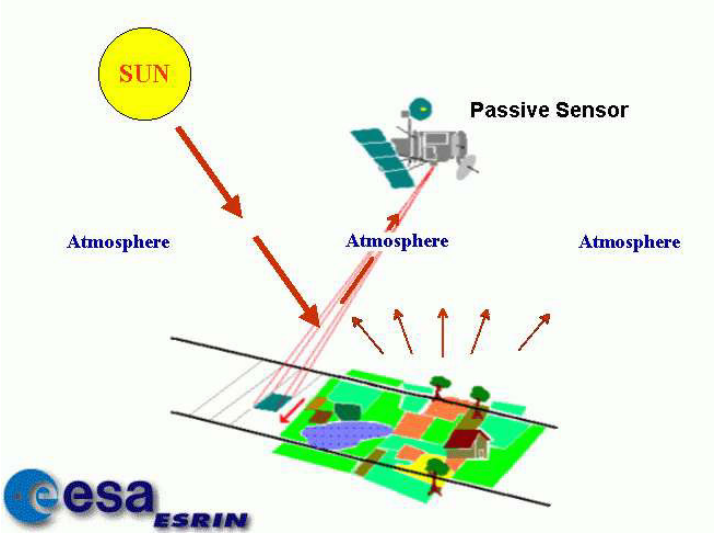


Fig. 13: Operation of passive sensor according to European Space Agency. Data Source: https://www.esa.int/SPECIALS/Eduspace_IT/SEMTZSZRA0G_0.html.

The use of microwave (MW) measurements, which involve capturing the natural electromagnetic radiation emitted by objects or, in the case of active systems, the retrodiffused radiation resulting from an energization, offers several advantages. One key benefit is their capability to be conducted at any time of day or night (Malnes et al., 2005; Jackson et al., 1996). Moreover, they are unaffected by weather conditions (Malnes et al., 2005): in the MW range, the attenuation of the signal received by sensors due to atmospheric gases and clouds is minimal for frequencies below 10 GHz (Elachi, 1987). When comparing active and passive sensors, apart from the distinction in the measured parameter, there are significant differences in spatial and temporal resolution. Specifically, active sensors excel in providing high spatial resolutions on the order of a few meters. However, this advantage comes with heightened sensitivity to surface roughness, topographical features, and vegetation. Additionally, active sensors tend to have long revisiting times (approximately spanning several months). Passive sensors, on the other hand, are

characterized by a more frequent temporal repetition (of the order of the hours) and spatial resolutions typically of the order of tens of kilometers. They too are sensitive, with less intensity than the active ones, to variations in surface roughness and the presence of vegetation.

The main differences are summarized in the Table 2; in general, the MW RS (both active and passive) exploit the dielectric capacity of the soil (Section 2.3) to measure $\theta$.

Table 2: Main differences between active and passive sensors.

| Characteristic | Passive Microwave | Active Microwave |
|---|---|---|
| Property Observed | brightness temperature<br>dielectric properties<br>soil temperature | backscatter coefficient<br>dielectric properties |
| Noise Sources | roughness<br>vegetation cover<br>temperature | roughness<br>surface slope<br>vegetation cover |
| Signal to Noise | fair – good | good – very go |
| Data Rate | Low | very high |
| Spatial Resolution | 10 – 100 km | 10 m |
| Swath Width | Wide | narrow – moderate |
| Vegetation Effect | Moderate | moderate – serious |
| Roughness Effect | Slight | Serious |
| Topographic Effect | Slight | Serious |
| Revisit Time | Good | poor – moderate |

### 2.5.1 Active microwave remote sensing technique

Active sensors utilize a radar antenna, which can be classified as either real aperture or synthetic aperture. These antennas emit pulses of electromagnetic waves towards the Earth's surface and capture the resulting backscattered signal, referred to as return signal. The strength of this retrodiffused signal varies based on the properties of the target and radar system, and it is quantified by the sensor. The

sensor itself can take the form of an imaging device, such as synthetic aperture radar (SAR), or a non-imaging device like scatterometers.

The intensity of the retrodiffused signal is defined by the backscattering coefficient (Schmugge, 1983). This coefficient represents the radar cross-section (measured in square meters, $m^2$) of a specific ground pixel per unit area of that pixel. Generally, it is expressed in decibels (dB) using the following formula (Ulaby et al., 1996):

$$\sigma^o_{dB} = 10 \log_{10} \sigma^o \qquad \text{Eq. 19}$$

The ability of the soil to retrodiffuse the incident electromagnetic radiation increases as the dielectric constant increases with non-linear growth so that it is greater for low values of $\varepsilon$. Champion (1996) empirically determined the backscattering coefficient $\sigma_0$from the $\theta$:

$$\sigma^0(db) = A + B\theta \qquad \text{Eq. 20}$$

where, A is the coefficient of retrodiffusion for a completely dry surface and B is the sensitivity of $\sigma o$ in measuring changes in the water content of soils.

The dispersion of a given soil is a function of its water content; in fact, a part of the incident impulse in a dry soil will penetrate the surface of the soil itself, while the same signal in a wet soil will increase the intensity of the retrodiffused signal. Variations in the backscattering coefficient are affected by dielectric and geometric properties, such as surface roughness, plant cover and object topography, and radar characteristics, such as wavelength, angle of incidence, polarization (Schmugge, 1983).

In greater detail, surface roughness plays a crucial role as a limiting factor in SM estimation (Wang et al., 1987). When surface roughness is excessively low

(corresponding to smooth surfaces), these surfaces function as mirror-like reflectors, resulting in a minimal return signal. Conversely, highly elevated surface roughness (very rough surfaces) causes surfaces to resemble Lambertian surfaces (Schmugge, 1983), scattering energy uniformly in all directions (Ulaby et al., 1982). In the former case, backscattering is significantly influenced by angles of incidence near the nadir (i.e., elevation angle close to 90°), while in the latter case, backscatter remains nearly angle-independent (Ulaby, 1986). The presence of vegetation overlying soil introduces additional complexity. Vegetation both absorbs and scatters a portion of incident microwaves, as well as microwaves reflected from the underlying surface. The extent of absorption is correlated with the moisture content within the vegetation, while scattering is impacted by the geometry and structure of the vegetation (Van de Griend and Engman, 1985). Studies have indicated that this effect can be mitigated but not completely eliminated (Su et al., 1997; Schmullius and Furrer, 1992; Van de Griend and Engman, 1985), achieved by selecting observation frequencies within the range of 1 to 5 GHz.

Vegetation notably influences active measurements in the case of vertical-vertical (VV) polarization in comparison to horizontal-horizontal (HH) polarizations. Recent research demonstrates a preference for cross-polarizations (Schumann et al., 2007; Henry et al., 2006; Solbø and Solheim, 2005; Horritt et al., 2003) over linear polarizations.

These active sensors, providing a measure of $\sigma^0$ made it is possible to trace $\theta$ given the linear relationship with the backscattering mentioned above (Ulaby et al., 1982). An approach to obtain this information is the change detection method proposed by Wagner (1998), which obtains the SM information by comparing $\sigma_0$ with the lowest value ( $\sigma^0{}_{dry}$ ) and highest value ( $\sigma^0{}_{wet}$) recorded extrapolated from a long series of measurements with a reference angle of 40 °.

$$SM = \frac{\sigma(40)^0 - \sigma(40)^0_{dry}}{\sigma(40)^0_{wet} - \sigma(40)^0_{dry}}$$ Eq. 21

This methodology has been widely applied both to old scatterometers (Wagner et al., 1999, European Remote Sensing Scatterometer, ERS Scatterometer) and to their new generation substitutes (Advanced scatterometer, ASCAT) of the European Space Agency; but also to SAR (Sentinel-1), from which originated the Surface Soil Moisture project 1 km of the Copernicus Global Land Service project.

The characteristics of SM products derived from active sensors are briefly reported.

#### 2.5.1.1 Main features of the Advanced SCATterometer

One of the instruments carried on board ESA's MetOp satellites (MetOp -A launched in 2006, MetOp -B launched in 2012 and MetOp -C launched in 2018) is the Advanced Scatterometer (ASCAT). Such a sensor operates in the C-band (5.3 GHz) with vertical polarization (VV). The MetOp satellites are ~50 min apart from each other with 09:30 a.m. descending and 09:30 p.m. ascending orbits, respectively. As said above, using a change detection method developed at the Institute of Photogrammetry and Remote Sensing (IPF), of the Vienna University of Technology (TU Wien), SSM data in degree of saturation (Wagner et al., 1999b) are retrieved from the backscattering measurements $\sigma^0$.

#### 2.5.1.2 Main features of the Sentinel-1 (S-1)

The Sentinel-1 constellation is made up of two identical satellites: Sentinel-1A, launched in 2014, and Sentinel-1B, launched in 2016. Both satellites are equipped with a C-Band Synthetic Aperture Radar (CSAR) instrument, enabling observations in one of four modes as illustrated in the Fig. 14:

- Stripmap (SM) - A standard SAR stripmap imaging mode.

- Interferometric Wide swath (IW) - Data is acquired in three swaths using the Terrain Observation with Progressive Scanning SAR (TOPSAR) imaging technique. This mode serves as the primary observation mode on the land and is particularly relevant for soil moisture retrieval.

- Extra Wide swath (EW) - Data is acquired in five swaths using the TOPSAR imaging technique. The EW mode provides extensive swath coverage but sacrifices spatial resolution.

- Wave (WV) - WV is the operational mode of Sentinel-1 over open ocean.

In the context of the SM application, the IW mode serves as the reference mode. IW mode data (with a spatial resolution of approximately 20 m) are provided as Level 1 Ground Range Detected products (L1-IWGRD), which serve as the input data for the Sentinel-1 Soil Moisture (SSM) 1 km processing chain. The IW mode primarily utilizes the VV polarization due to its enhanced sensitivity to soil moisture compared to cross-polarized observations in VH.

A derived product of the SM application from Sentinel-1 is the SSM 1 km CGLS. This product involves resampling data from the original 20 m resolution to 1 km resolution following the application of the soil moisture algorithm.

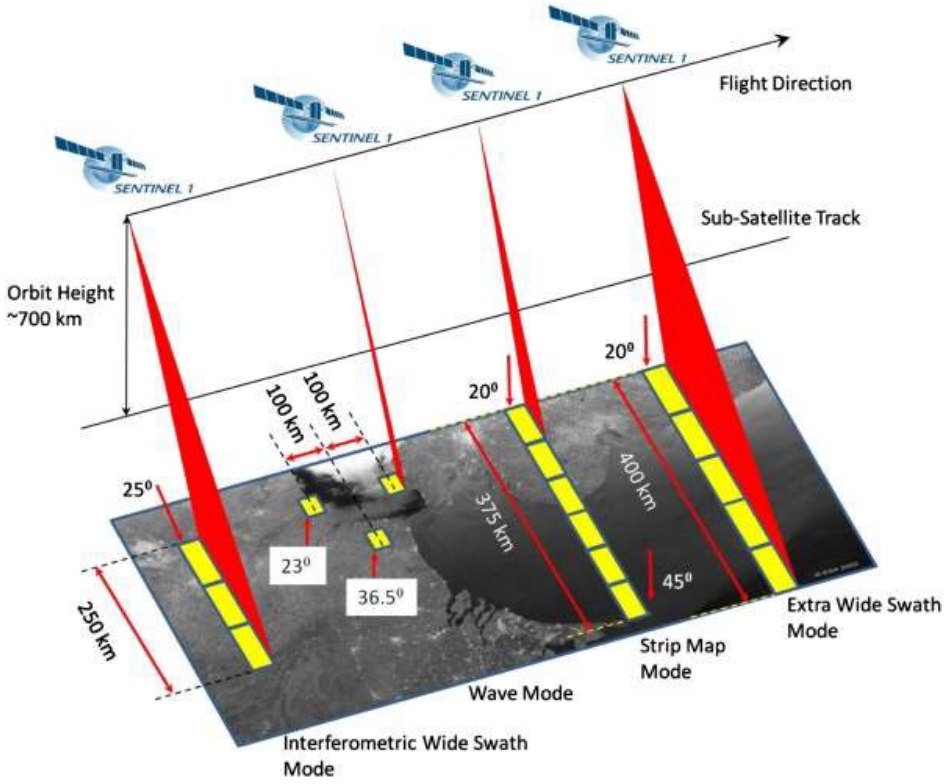


Fig. 14: Sentinel-1 acquisition modes. Data Source: https://Sentinels.copernicus.eu/web/Sentinel/user-guides/Sentinel-1-sar.

### 2.5.2 Passive microwave remote sensing technique

Radiometers are instruments used to measure electromagnetic radiation emitted and/or reflected from the Earth's surface within the spectral range specified in Table 1. The intensity of this radiation is typically quantified using the brightness temperature ($T_b$), which represents the temperature that a black body would need to have in thermal equilibrium with its surroundings in order to emit radiation at the observed intensity and wavelength.

The energy emitted from different points within the soil volume depends on both the dielectric properties of the soil (as discussed in Section 2.3) and the temperature of that specific point (Jackson et al., 1997). Similarly, to SAR observations,

radiometric measurements are also subject to the influence of surface roughness and vegetation, although to a lesser extent.

Starting from $T_b$ and normalizing with respect to body temperature, we can then derive the emissivity (e) of the soil. Subsequently, radiometers measure the product of soil temperature and its emissivity. This is based on the approximation of Rayleigh-Jeans (where h << kt) applied to Planck's law (Jackson et al., 1981).

$$T_{b_p} = \tau \cdot \left(\Gamma_p \cdot T_{sky} + e_p \cdot T_{soil}\right) + T_{atm} \qquad \text{Eq. 22}$$

where $\tau$ is the transmittance of the Earth's atmosphere, $\Gamma_p$ the surface reflectivity for polarization p, $e_p$ is the emissivity for polarization p. The first term within the bracket on the right side of this equation represents the radiation reflected from the sky, which varies with wavelength and atmospheric conditions. The second term relates to the emission from a bare ground surface, while the third term accounts for the contribution of the Earth's atmosphere between the surface and the receiver.

The emissivity of soil is notably influenced by its water content: a dry soil exhibits an emissivity of 0.95, which decreases to below 0.6 in the presence of water. Surface roughness enhances soil emissivity (Singh et al., 2003; Wang et al., 1983), narrowing the difference in $T_b$ measurements between dry and wet soils (Van de Griend and Engman, 1985). Vegetation has the most substantial impact on soil emissivity, as it can effectively mask the Earth's surface by absorbing electromagnetic radiation emitted by the soil. Subsequently, vegetation re-emits this radiation at its own temperature. For frequencies above 5 - 10 GHz, scattering effects within vegetation gain significance (Wigneron et al., 1998).

In the case of passive sensors are applied the radiation transfer models. Techniques belonging to this category can be classified as follows:

- Single Channel Algorithm (SCA): uses the acquired brightness temperature in horizontal polarization HH and makes use of ancillary data, which add additional errors in the estimation of SM.

- Multi - frequency or multi - polarized iterative algorithms: where the value of SM is iteratively "modified" in the calculations of $T_{bv}$ and $T_{bh}$ with a radiative transfer model (RTM) and compared with measurements at 6.9-18 GHz or 10-18 GHz (chosen according to radio frequency interference conditions) until the difference between the calculated and observed $T_b$ is minimal in square root terms.

- Algorithms based on polarization indices: linear regression is used to estimate soil moisture (Paloscia et al., 2001) and a polarization index to correct the effects of vegetation.

In general, the most reliable information of SM can be obtained from L-band measurements (Schmugge et al., 1988), where the SM sensitivity of radiometric measurements is maximum, surface roughness effects are minimal, vegetation can be considered semi-transparent and the information obtained is related to the deeper layers of the soil (Entekhabi et al., 1994). Among the main L-band radiometers, those on board of the European Space Agency, SMOS, or National Aeronautics and Space Administration., SMAP missions are the most important in the field of SM.

#### 2.5.2.1 Main features of Soil Moisture Ocean Salinity

The Soil Moisture Ocean Salinity (SMOS) mission was launched in November 2009 by the European Space Agency in collaboration with the French Centre National d'Études Spatiales (CNES) and the Spanish Centro para el Desarrollo Tecnológico Industrial (CDTI), as the first explorative mission able to provide observations of soil moisture and sea surface salinity exploiting the exchange in the Earth's water cycle between land and the atmosphere using MIRAS microwave L-

band (1.4 GHz) measurements. It consists of spaceborne interferometric radiometer able to provide global estimates of surface soil moisture with a sampling time step of 2-3 days at the equator and a ground resolution of 50 km (Kerr et al., 2001). It is the first satellite designed with the intention to measure soil moisture over land.

#### 2.5.2.2 Main features of Soil Moisture Active Passive

In 2015 the NASA Soil Moisture Active Passive satellite mission was launched to provide information on surface soil moisture, on the freeze/thaw state of the land surface, on root zone SM until 1 m (Derksen et al., 2017; Reichle et al., 2014), and net ecosystem exchange (NEE) of carbon. The SMAP satellite is equipped with a radiometer working in L-Band at a spatial resolution of ~36 km and a radar that functioned only for a few months in 2015 at a frequency of 1.26 GHz and a spatial resolution of ~3 km.

### 2.6 Combined measurements: the European Space Agency Climate Change Initiative

The combined European Space Agency Climate Change Initiative (ESA CCI-SM) product blends scatterometer-based (ERS- ½, Metop A/B ASCAT) and radiometer-based SM information (SMMR, SSM/I, TMI, AMSR - E, WindSat, AMSR2, and SMOS), utilizing a weighted normal technique with the loads being relative to signal to noise ratio (SNR) assessed by the triple collocation investigation of every item (Gruber et al., 2019a; Dorigo et al., 2017). A CDF matching procedure is used before integrating all datasets to scale the SM into the Noah land surface model by the Global Land Data Assimilation System (GLDAS) (Rodell et al., 2004). The day-by-day information provided concerns VWC (m3/m3) at a spatial resolution of 0.25° × 0.25°, distributed in NETCDF format.

### 2.7 Hydrological model

The purpose of hydraulic soil modelling is to provide a simplified view of complex hydraulic patterns within the soil (Brown and Heuvelink, 2006) because the

necessary data are often difficult or impossible to obtain directly from detailed field measurements, being costly and time consuming to collect for each new application (McNeill et al., 2018). Modelling can be divided into empirical modelling and models derived from hydrological modelling.

### 2.7.1 Pedotransfer function (PTF)

The first type of modelling is a well-established approach that has been used over time to estimate the hydraulic properties of the soil. This method uses mathematical functions by comparing field and laboratory measurements across various soils. This approach is grounded in the fact that the hydraulic properties of soils can be statistically derived from the physical and structural characteristics of soil horizons, including features such as texture, bulk density, organic matter content, and the mineralogy of the clay fraction (Romano and Santini, 1997).

The term "Pedotransfer function" (PTF), used to describe these mathematical functions (Vereecken et al., 1990; Bouma, 1989), refers to the techniques utilized to estimate hydrological parameters in the Van Genuchten (1980) and Brooks and Corey (1966) expressions using quicker and more cost-effective data collection methods.

A great number of PTFs exist in the literature (Saxton and Rawls, 2006; Scheinost et al., 1997; Vereecken et al., 1990; Rawls and Brakensiek, 1989; Saxton et al., 1986; Cosby et al., 1984; Brakensiek et al., 1984; Rawls et al., 1982; Gupta and Larson, 1979). The choice of which PTFs to employ depends on factors such as data availability, the nature of the survey, the scale of investigation, and the desired level of accuracy for the specific case.

Ungaro and Calzolari (2001) proposed a classification consisting of five PTFs:

- Level 1: particle size fractions (at least three), weaving classes.
- Level 2: particle size fractions (at least three), bulk density, or organic matter.
- Level 3: particle size fractions, bulk density, and organic matter.
- Level 4: particle size fractions, bulk density, organic matter and water content at -33 and -1500 kPa.

• Level 5: particle size fractions, bulk density, organic matter and saturation hydraulic conductivity Ks.

In detail, the PTF of Saxton et al., 1986, accepts as input the percentage of clay and sand and exploits the Brooks-Corey water retention curve, which represents the generalization of the Van Genuchten model. They are subject to applicability limits related to capillary potential range (1500-10 kPa), valid textural range (sand 5-30% and clay 8-58%; sand 30-95% and clay 5-60%).

Rawls et al. (1982) proposed a PTF, developed for ten discrete values of the water potential (10, 20, 33, 60, 100, 200, 400, 700, 1000, 1500 kPa), which also require the clay component [%] and the organic matter as inputs.

Rawls and Brakensiek (1989) have produced a formulation that adds to the percentage of sand and clay the value of porosity n (the ratio between the volume of voids Vv, volume not occupied by the solid phase, and the total volume of soil V) and has as limitation a textural range of sand 5-70% and clay 5-60%.

From the classification among the inputs typically essential for applying PTF, the information of soil texture is included. Based on the size of the soil particles we define gravel (> 2 mm), sand (0.05 ÷ 2 mm), silt (0.002 ÷ 0.05 mm) and clays (<0.002 mm). Gravel is the solid skeleton of the soil. The soil texture can be traced back to nomenclature. The most common classification is that of United States Department of Agriculture (USDA) (1951) represented graphically in a triangular diagram (Fig. 15). From the base of the triangle, the size classes of sand, silt and clay are arranged counterclockwise, while the percentage scale is increasing clockwise. In this way from the texture, it is possible to trace the type of soil and through the PTF mentioned above it is possible to derive the hydrological parameters of the soil.

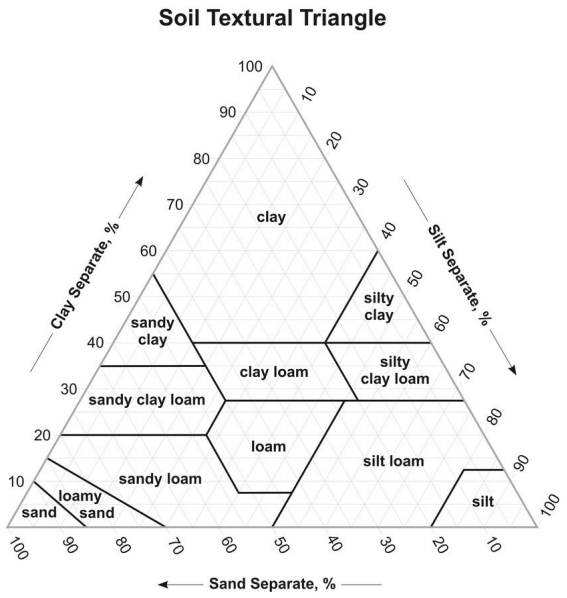


Fig. 15: USDA triangle texture. Data Source: Soil Survey Manual, YSDA Handbook 18, Washington, D.C.

In the Table 3 the mean value of porosity (n) with the range of variations, the saturation at WP ($s_w$) and the saturation at FC ($s_c$) for each type of soil according to the twelve classes USDA of Fig.15 was reported:

Table 3: n, $s_w$, $s_c$ for each soil type according to Rawls and Brakensiek, 1989 and Rawls et al., 1992.

| ID | Soil type | n [-] | $s_w$ | $s_c$ |
|---|---|---|---|---|
| 1 | Sandy | 0.437 (0.374-0.500) | 0.06 | 0.14 |
| 2 | Loamy sand | 0.437 (0.363-0.506) | 0.11 | 0.24 |
| 3 | Sandy loam | 0.453 (0.351-0.555) | 0.19 | 0.42 |
| 4 | Silty loam | 0.463 (0.375-0.551) | 0.27 | 0.57 |
| 6 | Loam | 0.501 (0.420-0.582) | 0.25 | 0.50 |
| 7 | Sandy clay loam. | 0.398 (0.332-0.464) | 0.34 | 0.62 |
| 8 | Silty clay loam | 0.464 (0.409-0.519) | 0.45 | 0.73 |
| 9 | Clay loam | 0.471 (0.409-0.519) | 0.40 | 0.67 |
| 10 | Sandy clay | 0.430 (0.370-0.490) | 0.51 | 0.75 |
| 11 | Silty clay | 0.479 (0.425-0.533) | 0.52 | 0.78 |

| | | | | | |
|---|---|---|---|---|---|
| 12 | Clay | 0.475 | (0.427-0.523) | 0.56 | 0.8 |

The ID derived from https://ldas.gsfc.nasa.gov/gldas/soils.

### 2.7.2 Hydrological balance modelling

Efforts to delineate the hydrological balance must take into account the scale of investigation. In fact, in order to provide a realistic description of the dynamics of SM in an analytically manageable way (Laio et al., 2001; Rodriguez-Iturbe et al., 1999) it is necessary to deepen the analysis of the climate-soil-vegetation system.

Although the variables involved are the same, their role changes depending on the spatial and temporal scale in which the phenomenon is observed: the spatial heterogeneity of the parameters that describe soil, vegetation and topography (e.g., radiation, precipitation or wind) make complex understanding of which component governs the partitioning of precipitation in transpiration, runoff, drainage and storage. The variability of SSM in the remotely detected surface layer (0,5 - 2 cm) is particularly high, since this is the active layer for evaporation, and because of the vertical and lateral redistribution which in turn are related to microtopography and changes in soil properties on the meter scale (Wagner et al., 1999b).

With the aim to describe the SM dynamic, Rodriguez-Iturbe et al. (1999) presented a probability modelling approach on a point scale searching links between the SM dynamics with climate, soil and vegetation. It is based on the steady-state solution of the stochastic differential equation for the water balance of the soil water balance, in which rain represents a stochastic forcing. In the absence of lateral contributions, the Eq.2 becomes in infinitesimal terms:

$$nz\frac{ds}{dt} = I(s,t) - E(s,t) - L(s,t) \qquad \text{Eq. 23}$$

Where n è is the porosity; z is the soil depth; s = $\frac{\theta}{n}$ the relative water content; I(s,t) is the precipitation infiltrated in the soil; E(s,t)evapotranspiration and L(s,t) is the part due to leakage and depth percolation.

Considering the precipitation as a poissonian stochastic process (Milly, 1993) (discrete stochastic process representing the random and independent arrival of events in an interval of time or space)on a large scale, they showed that it is related to SM due to regional feedback. They concluded that spatial dynamics needed to be further deepened to describe more accurately the dynamics of SM and the partitioning of the hydrological balance. Laio et al. (2001) attempted to make improvements to the theory of evapotranspiration and lateral losses and confirmed the applicability of its formulation in the work of Salvucci (2001), which evaluated the dependence between water content and leakage in Illinois.

However, hydrological problems are rarely addressed on a point scale, but rather on a basin scale, regional and global, hence the importance of distributed hydrological models (Abbott and Refsgaard, 1996). A distributed model is a model that considers each element of the grid (pixel) as a ground-vegetation system on which to simulate physical and biological processes (Chen et al., 2005).

These distributed models are used within general circulation models (GCM) for climate estimation and weather forecasting. In most cases, hydrological models are of the "bucket" type (Manabe, 1969), as in the case of the Simple Biosphere Model (SiB) (Sellers et al., 1986), a model that tries to represent the patterns of soil-vegetation-atmosphere transfer (SVATS). It is a model with high vertical but not spatial resolution (Wood, 1991 )and a large number of variables, which (Xue et al., 1991) attempted to reduce.

The Variable Infiltration Capacity (VIC) model was implemented in the Geophysical Fluid Dynamics Laboratory general circulation model (GCM) (Wood et al., 1992) and generalized by Liang et al. (1994). It used a two-layer scheme (Stamm et al., 1994) and an aerodynamic representation of latent and surface-sensitive heat flows. The soil representation is a simplified representation and allows for the simultaneous presence of different types of vegetation. The model of variable infiltration capacity (VIC) (Liang et al., 1996, 1994), and its updates (Bowling and Lettenmaier, 2010; Bowling et al., 2004; Cherkauer et al., 2003) have

been widely used ranging from water management to land-atmosphere interactions and climate change. VIC has been exploited both as a hydrological model and as a scheme of the Earth's surface coupled to GCM.

The Noah Land Surface Model (Ek et al., 2003) was developed at the National Centers for Environmental Prediction (NCEP), part of the National Oceanic and Atmospheric Administration (NOAA) in the United States. Its purpose is to improve the representation of surface processes, such as the water cycle and energy balance, within weather forecasting models and general circulation models, offering a detailed representation of the processes along the vertical profile. Over time, it has undergone updates and revisions, including increases from two to four layers of soil or changes to the formulation of crown conductance (Chen et al., 1996). This model is one of those embedded and run autonomously in modeling frameworks developed to enhance the ability to simulate surface processes, earth-atmosphere interaction, and other related phenomena.

The Land Information System (LIS) is a software framework that integrates the use of advanced models of the Earth's surface and calculation tools to accurately characterize the states and flows of the Earth's surface. LIS employs the use of scalable and high-performance data computing and management technologies to address the computational challenges of high-resolution Earth surface modeling (Kumar et al., 2006). It was used to develop the 25 km Global Land Data Assimilation System (GLDAS) (Rodell et al., 2004) and the 12.5 km North American Land Data Assimilation System (NLDAS) (Mitchell et al., 2004).

On the other hand, the Land Data Assimilation System (LDAS) also integrates observed data from stations as well as from satellite observations so as to provide constant updates that can mitigate model errors and improve the representation of the state of the Earth's surface in regions and periods with available observations (Albergel et al., 2017). These efforts have led to the production of a dataset of reanalysis ERA5-Land (Muñoz-Sabater et al., 2021; Copernicus Climate Change Service, 2019a, 2019b), which is based on the surface model of the European

Centre for Medium-Term Weather Forecasts (ECMWF): the Carbon Hydrology-Tiled ECMWF Scheme for Surface Exchanges over Land (CHTESSEL). CHTESSEL focuses on the representation of carbon exchange and hydrology processes on land and is an integral part of the Integrated Forecasting System (IFS), supporting a wide range of meteorological and numerical weather forecasting (NPW) applications (Boussetta et al., 2021).

#### 2.7.2.1 ERA5-Land dataset

ERA5-Land is a global dataset designed to enhance the terrestrial component of the fifth generation of the European ReAnalysis (ERA5), which is a crucial component of the European Commission's Copernicus Climate Change Service (C3S). This dataset encompasses approximately 50 variables that intricately describe the water and energy cycles occurring on land worldwide. These variables are captured every hour, offering a spatial resolution of 9 km, corresponding to the ECMWF triangular-cubic-octahedral operating grid (TCo1279) (Malardel et al., 2016). The primary objective is to provide a representation that spans from 1950 onwards. As of January 2020, the ERA5-Land dataset's available period has been extended from January 1981 to nearly the present, even if with a time delay of 2-3 months compared to real-time observations. This dataset offers a comprehensive portrayal of the land's water and energy cycles through a grid that faithfully mirrors the computational and three-dimensional nature of the Earth's surface.

To generate this dataset, various factors are incorporated, including land and sea masks, lake cover and depth information, soil and vegetation types, and vegetation cover. The reliability of the data has been validated through meticulous comparisons with numerous in situ observations, predominantly spanning the period from 2001 to 2018. Additionally, comparisons with other models have been carried out to further ensure data quality (Muñoz-Sabater et al., 2021, p. 5). ERA5-Land is a significant advancement beyond ERA5, with which it shares the majority of parameters that underscore cutting-edge surface modeling techniques applied within numerical weather forecasting (NWP) models. Key distinctions lie in the

dataset's focused emphasis on fundamental ground processes and the considerable enhancement in spatial resolution, globally refining it to 9 km compared to ERA5's 31 km. Despite these differences, both datasets maintain an identical temporal resolution, featuring hourly data points.

### 2.7.3 Hydrological modelling along soil profile

Numerous studies have attempted to estimate the SM along the soil profile from SSM (Ragab, 1995; Entekhabi et al., 1994) as the deepest layer is the layer through which the vegetation draws sustenance and transpiration takes place. The models proposed above (e.g., Section 2.7.2.1) also consider the modeling along the vertical profile: the ERA5- Land provides SM [$m^3/m^3$] for four different layers of soil: 0-7 cm; 7-28 cm; 28-100; 100-289 cm. Another type of RZSM dataset is obtained through the application of a surface model to a product deriving from the SMAP mission (Section 2.5.2.2, i.e., SMAP L4, which will be discussed in Section 3.3.3). But this is a given averaged on a thickness of one meter. Generally, in the assimilation techniques the major disadvantage is related to the representation of variables and how physical processes are modeled (Sabater et al., 2007). Alongside these datasets, over time semi-empirical modeling has been proposed: the exponential filter, (Wagner et al., 1999a) and the mathematical modeling Kalman's filter (Walker et al., 2001) are still applied today to transmit SM satellite information of surface into deep layer.

#### 2.7.3.1 The exponential filter

The physical processes governing the interaction between SSM-RZSM (Sabater et al., 2007; Houser et al., 1998) have long been central to deriving regression coefficients based on site-specific characteristics (Jackson, 1986). Soil water content exhibits heterogeneity in size and variability on a small scale due to soil properties and hydrological patterns. This complexity is emphasized on a larger scale by the intricate nature of vegetation, further complicating interpretation.

Wagner et al. (1999) introduced a low-pass filter technique that smooths information at surface level in favor of that of deeper layers. The basis is a

simplified two-layer soil budget, in which the second layer is treated as a reservoir. The flow between these layers is directly proportional to the difference in SM between them:

$$nz\frac{ds_2}{dt} = C[s_1(t) - s_2(t)] \quad \text{Eq. 24}$$

with n porosity, z depth of the layer, $s_1$ water content of the first layer, $s_2$ water content of the second layer and finally C is the pseudodiffusivity, which should encompass all the heterogeneous characteristics of the soil and related to hydrological processes. By introducing the characteristic length time $T = \frac{nz}{C}$, assuming the hydraulic conductivity of the soil is constant, t is time and $\tau$ integration variable, Eq. 24 becomes:

$$s_2(t) = \frac{1}{T}\int_{-\infty}^{t} s_1(\tau)\exp\left[-\frac{(t-\tau)}{T}\right]d\tau \quad \text{Eq. 25}$$

Discretizing Eq.25, it could be written in terms of Soil Water Index (SWI), calling $s_1$ as SSM:

$$SWI_m\ (t_n) = \frac{\sum_i^n SSM\ (t_i)e^{-\frac{t_n - t_i}{T}}}{\sum_i^n e^{-\frac{t_n - t_i}{T}}} \quad \text{Eq. 26}$$

Eq. 26 was subsequently made recursive by Albergel et al. (2008) yielding the recursive estimate of the Stroud (1999) exponential filter:

$$SWI_{m(n)} = SWI_{m\,(n-1)} + K_n\ (SSM_m\ (t_n) - SWI_{m(n-1)} \quad \text{Eq. 27}$$

Where:

$$K_n = \frac{1}{1+\sum_i^n e^{-\frac{t_n - t_i}{T}}} \quad \text{Eq. 28}$$

And finally in the recursive formulation:

$$K_n = \frac{K_{n-1}}{K_{n-1}+e^{-\frac{t_n - t_i}{T}}} \quad \text{Eq. 29}$$

### 2.7.3.2 The exponential filter as fusion algorithm

As part of the Copernicus Global Land Service project, the exponential filter was applied for the creation of the CGLS Soil Water Index Version (SWI) product. SWI is calculated from the fusion of Sentinel-1 C (SAR) and the measurements of Metop ASCAT sensors. The data come with a daily time resolution and a different

spatial resolution (respectively 1 km or 0.1 degrees) depending on whether you consider the product "local", which uses, as mentioned, the information of ASCAT- Sentinel-1 (SCAT-SAR SWI) or the global product, which only uses ASCAT. The version of the soil moisture recovery algorithm is the version modified by (Naeimi et al., 2009), and the information of SWI (both superficial and deep to the variation of T) is provided as a daily information in saturation degrees. It is necessary to specify that the recursive formulation does not consider the weaving properties of the soil.

Bauer-Marschallinger et al. (2018) have developed a fusion algorithm to produce the SWI 1km product, after parameter creation, as a combination of ASCAT and Sentinel-1 SSM information. The algorithm is based on fundamental steps that are:

• Oversampling of the ASCAT grid to 1 km (through the python thin plate spline module) to have the same spatial resolution of the Sentinel-1 data.

• Generation of matching parameters (MP) through the application of the cumulative distribution function (CDF) at times using percentiles (ten percent intervals from 10% to 90%) at each point of the grid.

• Definition of a statistical weight that in Bauer-Marschallinger et al., (2018) is fixed at 1:1 (equal for both inputs), although this gives greater importance to ASCAT because of its greater amount of information.

• Application of Weighted Temporal Filtering recursive to obtain SWI high spatial and temporal resolution information, following the Eq.30:

$$SWI_T^W \quad (t_{i+1}) = \frac{SWI_T^W \quad (t_i)\frac{n+1}{n}\sum_i^n w_i(den_T(t_{i+1})-1)+SSM\,(t_{i+1})(n+1)w(t+1)}{\sum_i^n w(t_{i+1})den_T(t_{i+1})} \qquad \text{Eq. 30}$$

With $den_T(t_{i+1}) = 1 + e^{-\frac{t_n - t_i}{T}} den_T(t_i) = \frac{1}{K_{T(t_i+1)}}$.

### 2.7.3.3 Soil Moisture Analytical relationship (SMAR)

The exponential filter has proven to be a simple and effective method for obtaining insights into water content, but determining the appropriate parameter T, which encompasses a range of physical processes, presents challenges (Wang et al., 2017;

Albergel et al., 2008). This led Manfreda et al. (2014) to undertake an endeavor where they developed a model derived from the exponential filter formulation. This enhanced model takes into consideration soil properties. The foundation of this model relies on the conceptual division of the soil into two layers: an upper layer, typically spanning a few centimeters (5-10 cm), and a deeper layer, generally extending from 60 to 150 cm. By disregarding lateral flows and capillary rise, the interaction between these soil layers primarily involves infiltration. Under the assumption that movement between the two layers occurs solely when the water content surpasses the field capacity (FC), and employing the Green-Ampt approach for modeling soil moisture movement (Laio, 2006), the infiltration component can be expressed as:

$$n_1 z_1 y(t) = n_1 z_1 y(s(t), t) = n_1 z_1 \begin{cases} s_1(t) - s_{c1}(t) \\ 0 \end{cases} \quad \text{Eq. 31}$$

Where subscript 1 indicates everything related to the top layer, while subscript 2 refers to the bottom layer. y(t) is the fraction that infiltrates in the lower layer; $n_1$ the porosity of the first layer of soil; $z_1$ the depth of the first layer of soil; $s_{c1}$ is the saturation at the FC.

Thus, defined infiltration and exploiting a simplified form of the loss function, including both evapotranspiration and percolation (Rodríguez-Iturbe et al., 2006; Porporato et al., 2004), the budget equation (Eq. 23) is thus simplified through the introduction of $x_2$ and $w_0$.

$$x_2 = \frac{s_2 - s_{W2}}{1 - s_{W2}}$$

$$w_0 = (1 - s_{W2}) n_2 z_2$$

$$(1 - s_{W2}) n_2 z_2 \frac{dx_2(t)}{dt} = n_1 z_1 y(t) - V_2 x_2(t) \quad \text{Eq. 32}$$

With $V_2$ loss coefficient, which encompass both evapotranspiration and depth percolation and $s_{w2}$ saturation at wilting point (WP). Thus, introducing normalized coefficients a (related to losses) and b (related to depth and soil properties), Eq.32 becomes:

$$a = \frac{V_2}{(1 - s_{W2})n_2 z_2} \; b = \frac{n_1 z_1}{(1 - s_{W2})n_2 z_2}$$

$$\frac{dx_2(t)}{dt} = by(t) - ax_2(t) \quad \text{Eq. 33}$$

And finally:

$$s_2(t) = s_{w2} + \left(s_2\left(t_{j-1}\right) - s_{w2}\right)e^{-a\left(t_j - t_{j-1}\right)} + (1 - s_{W2})by\left(t_j\right)\left(t_j - t_{j-1}\right) \quad \text{Eq. 34}$$

The SMAR model introduces four physically based parameters ($s_{w2}, s_{C1}, a, b$). However, the parallelism between the characteristic length time T and a, which is also more difficult to determine than the other parameters, should be specified. For this reason, numerous subsequent studies have attempted to improve the formulation of SMAR by deepening the part related to losses (Baldwin et al., 2017; Faridani et al., 2017a, 2017b).

### 2.8 Soil moisture network

Ground-based measures have always played a central role in hydrological modelling, however with the launch of the first satellite missions an effort was required to create a standardized ground network of SM, that could be used in applications related to SM products.

#### 2.8.1 The International Soil Moisture Network (ISMN)

Since 2009, the ISMN has helped with calibration and validation efforts of SM retrievals (Dorigo et al., 2013, 2011), gathering and harmonizing data from diverse organizations and improving the integration of advanced quality control methods (Dorigo et al., 2013), provision of additional metadata, and ancillary variables (e.g., precipitation, soil and air temperature). The ISMN data are available at data host facility of TU Wien under supervision of the BfG Federal Institute of Hydrology (https://ismn.geo.tuwien.ac.at/).

### 2.8.2 The COSMOS-Europe network

Another SM network is the COSMOS-Europe network. This network is a European network of Cosmic-Ray Neutron Soil Moisture Sensors. It contains data from 66 cosmic-ray neutron sensors (CRNS) in 12 European countries (in alphabetical order: Austria, Denmark, France, Germany, Greece, Italy, Norway, Poland, Spain, Switzerland, Turkey, United Kingdom) (Bogena et al., 2021). The main difference with the ISMN is that the COSMOS-Europe uses as unique technology the cosmic ray, while the ISMN includes different stations all over the world and different technologies (TDR, FDR etc., Section 2.4). In addition, the SM measured by the cosmic ray refers to an area instead of a point, with a swath of hundreds of meters and a depth of order of 20 cm.

*Chapter 3*

# MATERIALS AND METHODS

In this section, all the materials and methods used for our elaboration are presented. The extensive variety of SM measurement types presented in Chapter 2, required a data exploration aimed at comprehensively grasping the distinctive characteristics inherent in each approach. This analysis was made in particular between the SM remote sensing data and the ground-based data at the ecoregion scale (Section 3.3), using also the ERA5-Land dataset. Therefore, the hosting at TU Wien facilitated a more concentrated investigation into the capabilities of active sensors (Section 3.2). This phase also involved a detailed examination of the algorithms outlined in Section 2.7, culminating into the development of an adaptation of the fusion algorithm between the enhanced S-1 SSM (not already public available) and ASCAT data record (Section 3.5.1). Utilizing the knowledge gained, an effort was made to create a complete framework capable of producing four-dimensional SM measurements introducing a physically based model to compute the RZSM (Section 3.5.2). This framework is important, especially in the context most affected by the effect of climate change, such as the Mediterranean area, as the major area subjected to ongoing climate change (Guo et al., 2023; L. Noto et al., 2023; L. V. Noto et al., 2023; Pompeu et al., 2023).

The data used in our study are listed below:

- Spaceborne remotely sensing data (Section 3.2.1): SMOS – IC, SMAP L4, ESA CCI, ASCAT (H115-H116), ASCAT (H119-H120), CGLS SSM 1 km, the improved S-1 SSM.

- Ground-based data: ISMN data belonging to the European Ecoregions (Section3.2.2.1) and COSMOS Alento network (Section3.2.2.2).

- Modelled data: ERA5-Land at its normal resolution 9 km and downscaled at 1 km (Section 3.2.3).

In the following, we explain the concept of ecoregions, which is the scale analysis for the investigation of SM type of measurements, before going into depth about the characteristics of each data set employed. Moreover, the reason of the choose of ecoregions as reference area will be explain in Section 3.3.

### 3.1 The European ecoregions

In 1996, the WorldWide Fund (WWF) for Nature launched the "Global 200 Initiative," a campaign to promote biodiversity conservation (Bulgarini et al., 2004), and making a digital map of 867 terrestrial ecoregions (https://ecoregions.appspot.com/). These ecoregions should be a priority for implementing conservation actions in relation to their outstanding biodiversity features in the terrestrial, freshwater, and marine realm (Olson and Dinerstein, 2002; Olson et al., 2001). Their boundaries have been determined using a combination of existing global maps, such as zoogeographic (Rübel et al.,1930), biotic provinces (Dasmann et al.,1974, 1973), and vegetation types (UNESCO 1969).

Dinerstein et al. (2017) improved the delimitation in the original Terrestrial Ecoregions (Ricketts et al., 1999; Olson and Dinerstein, 1998) to better highlight regions of the world that are highly distinctive and deserve greater attention for their peculiar habitats.

Europe belongs to the Palearctic biogeographic realm and contains six biomes (i.e., boreal forests/taiga; Mediterranean forests, woodlands & scrub; temperate

broadleaf & mixed forests; temperate conifer forests; temperate grasslands, savannas & shrublands; tundra) and 37 terrestrial ecoregions ranging from Mediterranean-climate woodlands and scrub to temperate rainforests or tundra. All together, these ecoregions span an area larger than the European territory, including a subset of north-west Asia. Hence, in this study, we refer to these areas as "continental" or "European" scale. Ecoregions are not equally represented both by the number of ISMN monitoring stations and by their spatial distribution over the area. Fig. 16 represents the ISMN ground-stations, aggregated using different symbols by local network managed by different individual organizations/institutes, above the ecoregions considered in this study identified by a unique code and color. For a detailed description of the ISMN network used, please see Section 2.1.1.

It is evident that there are a few ecoregions represented by ground-based stations concentrated only in a defined sub-sector. According to the SM temporal stability concept (Liu et al., 2011; Brocca et al., 2011; Loew and Schlenz, 2011; Brocca et al., 2009; Starks et al., 2006; Cosh et al., 2006; Vachaud et al., 1985), local SM signal can be representative of larger areas, considering that the temporal pattern of point SM data is closely related to the temporal pattern of its surrounding area (Brocca et al., 2011). This implies that persistent regional SM patterns can influence individual zones within a region, resulting in similar SM dynamics. Therefore, it is acceptable to use datasets that describe SM in the same way but are recorded at different scales. In line with this approach, we aggregated results from non-homogeneously or sparsely distributed ground stations (in terms of median values) to represent the entire ecoregion, following the methodology used by Baldwin et al. (2017) in the USA. Furthermore, it is worth noting that, as we said above, ISMN stations are randomly spatially distributed in Europe, with some of the EU ecoregions completely uncovered. Therefore, it was possible to make the comparison of SM satellite products and ground measurements only in 16 of the 37 above-cited ecoregions. The main features of the considered ecoregions,

including their specific Koppen-Geiger climate classification, are described in Table 4.

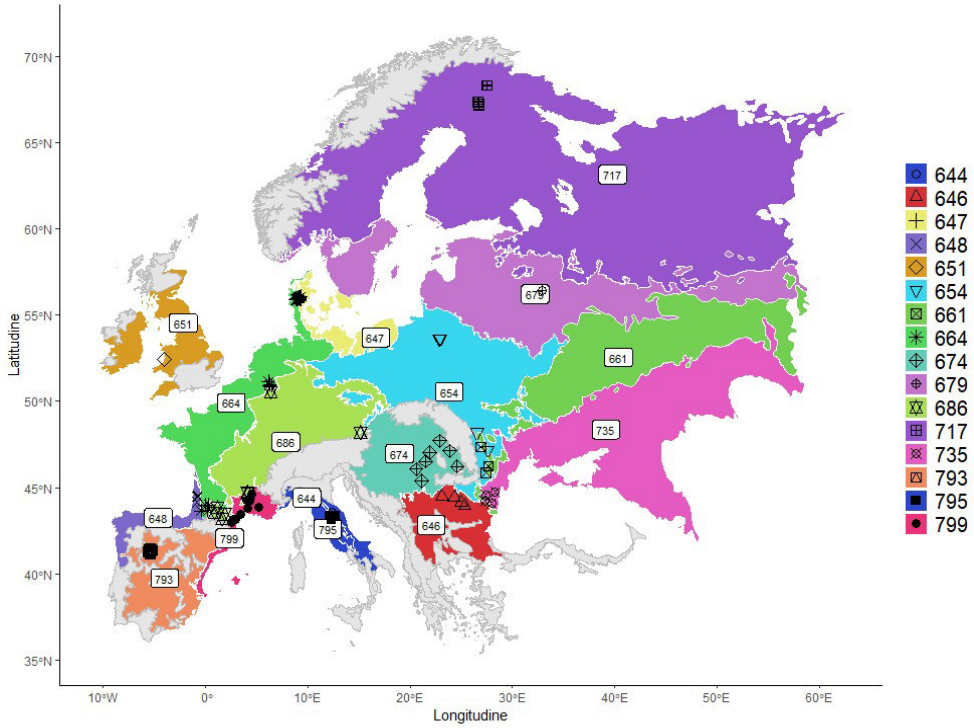


Fig. 16:Distribution of the 16 ecoregions considered in this study, spanning an area larger than the European territory, including a subset of north-west Asia and location of the used ISMN stations indicated using different symbols for each local network.

Table 4: European ecoregions considered for the intercomparison.

| Name | ID | Description | Koppen – Geiger climate[1] |
|---|---|---|---|
| Apennine deciduous montane forests: | 644 | remote preserved forests and montane grassland in central Italy with a very wet climate | Cfb[2] |
| Balkan mixed forests: | 646 | great biodiversity area characterized by strong seasonality; it presents a merge of Mediterranean and Continental climate influences | Cfa[3] |
| Baltic mixed forests: | 647 | forests with mild winters and frequent precipitation of low intensity | Cfb |
| Cantabrian mixed forests: | 648 | shrubs, dry heaths, wet heaths, and peatland areas with a warm Atlantic climate (oceanic winds exposure) | Cfb |
| Celtic broadleaf forests: | 651 | area with a warm temperate climate and strong maritime influence; its western part in the UK is characterized by humidity and frequent rainfall | Cfb |
| Central European mixed forests: | 654 | ecoregion with a predominantly continental climate | Cfb |
| East European forest steppe: | 661 | lowland area that extends to the foothills of the Carpathians in Romania | Cfb |
| European Atlantic mixed forests: | 664 | region stretching from the south of France to the northernmost tip of Denmark, influenced by the Gulf Stream (warm, humid air from the Atlantic) | Cfb |
| Pannonian mixed forests: | 674 | larger grassland surrounded by the Carpathian Mountains in the northeast which influence climate and prevent much rainfall from reaching its center | Cfb |
| Sarmatic mixed forests: | 679 | mixed forests with alternating rivers and lakes with a predominately continental climate although there is maritime influence along coastlines | Dfb[4] |

[1] (Kottek et al., 2006)

It is worth noting that the climate classification was based on the median climate classification of ground-based stations in each ecoregion.

[2] Cfb (warm temperate, fully humid, warm summer): Temperate oceanic climate or subtropical highland climate; coldest month averaging above 0 °C (32 °F) (or −3 °C (27 °F)), all months with average temperatures below 22 °C (71.6 °F), and at least four months averaging above 10 °C (50 °F). No significant precipitation difference between seasons (neither abovementioned set of conditions fulfilled).

[3] Cfa (warm temperate, fully humid, hot summer): Humid subtropical climate; coldest month averaging above 0 °C (32 °F) (or −3 °C (27 °F)), at least one month's average temperature above 22 °C (71.6 °F), and at least four months averaging above 10 °C (50 °F). No significant precipitation difference between seasons (neither abovementioned set of conditions fulfilled). No dry months in summer.

[4] Dfb (snow, fully humid, warm summer): Warm-summer humid continental climate; coldest month averaging below 0 °C (32 °F) (or −3 °C (27 °F)), all months with average temperatures below 22 °C (71.6 °F), and at least four months averaging

| | | | |
|---|---|---|---|
| Western European broadleaf forests: | 686 | ecoregions stretch on a large part of Western Europe with high value of mean annual rainfall | Cfb |
| Scandinavian and Russian taiga: | 717 | ecoregion covers the Northern Europe, presenting a cool, humid climate with a greater maritime influence | Dfc[5] |
| Pontic steppe: | 735 | extending across Southeast Romania having a temperate climate with appreciable winter rain | Cfa |
| Iberian sclerophyllous and semi-deciduous forests: | 793 | region covers the Iberian Peninsula exhibiting very hot and dry summers and relatively mild, subhumid winters | Csb |
| Italian sclerophyllous and semi-deciduous forests: | 795 | region gets around the Italian peninsula exhibiting Mediterranean climate (hot dry summers and humid, cool winters) | Cfb |
| Northeast Spain and Southern France Mediterranean forests | 799 | region embraces Southern France typically with very hot and dry summers and relatively temperate and humid to sub-humid winters | Cfa |

## 3.2 Datasets

### 3.2.1 Spaceborne remotely sensing data

**SMOS-IC:** The SMOS-IC v.02 at 25 km of spatial resolution is a globally products, available in both ascending (i.e., 06:00 a.m.) and descending (i.e., 06:00 p.m.) orbits. The SMOS-IC minimizes the use of auxiliary data (e.g., the Moderate Resolution Imaging Spectroradiometer (MODIS), Leaf Area Index (LAI)), exploiting the ISMN in situ observations and global maps of Parrens et al. (2016) to optimize the effective vegetation scattering albedo (ω) (Fernandez-Moran et al., 2017) and the roughness parameters, respectively. We have filtered out the signals affected by potential RFI contamination by masking out the ones when root mean square error between SMOS L3 and simulated Brightness Temperature ($T_B$-RMSE) were higher than 10 K (Wigneron et al., 2020; Al-Yaari et al., 2019) and the strong topography,

above 10 °C (50 °F). No significant precipitation difference between seasons (neither abovementioned set of conditions fulfilled).

[5] Dfc (snow, fully humid, cool summer): Subarctic climate; coldest month averaging below 0 °C (32 °F) (or −3 °C (27 °F)) and 1–3 months averaging above 10 °C (50 °F). No significant precipitation difference between seasons (neither abovementioned set of conditions fulfilled).

frozen scene, and contaminated scene (urban + ice + water bodies) by masking out scene flags (SF) <=1 (Wigneron et al., 2021; Li et al., 2021, 2020).

**SMAP L4**: Among the different available half-orbit SM products (e.g., SMAP L2, SMAP L3), we used the model assimilated product SMAP L4 v6 (Data Set ID: SPL4SMAU) at 3-h time resolution on the global 9 km modeling grid. The SMAP L4 assimilates the 36 km brightness temperature (from L1C_TB), the 9 km brightness temperature downscaled by the L2_SM_AP algorithm and freeze/thaw observations (from L3_FT_A) using an ensemble Kalman filter (EnKF, Reichle et al., 2014). No filter was applied on the product.

**ESA CCI**: The main features of the ESA CCI are already reported in Section 2.6. The day-by-day information provided concerns VWC ($m^3/m^3$) at a spatial resolution of 0.25° × 0.25°, distributed in NETCDF format. We refer to the ESA CCI v6 product, ending in 2020. Data related to pixel locations covered by snow or with temperatures below 0 °C or covered by dense vegetation have been filtered out.

**ASCAT (H115-H116)**: The first part of the study was conducted with the Metop ASCAT surface SM climate data records (CDRs), specifically, the H115 – Metop ASCAT SSM CDR2019 (H SAF, 2020) and its temporal extension H116, at a spatial resolution of 12.5 km, expressed in terms of degrees of saturation, converted to physical units in meters using a globally and high-resolution porosity map with average polygon size ~100 km (Gleeson et al., 2014). During our analysis, SSM was excluded when its value was lower than 0 or greater than 100, or the processing flags (PROC_FLAG) indicated that no retrieval was carried out (e.g., PROC_FLAG > 1) or the surface state flag (SSF) indicated the following soil surface conditions: unknown, unfrozen, frozen, temporary melting/water on the surface or permanent ice.

**ASCAT (H119-H120)**: The H119 ASCAT SSM CDR v7 12.5 km and its temporal extension H120 ASCAT SSM CDR v7 12.5 km (H SAF, 2021) have the same properties as the H115-H116, but with a different temporal extension. In fact, we used a period spanning from 2017 January to 2022 July for our second part of the work, i.e., fusion and the creation of a four-dimensional SM framework. On the other hand, the first half (H115–H116) focused on the period from 2015 to 2020. Additionally, we did not convert the data into VWC because we needed the data in terms of saturation for this second section.

**CGLS SSM 1 km**: The Copernicus Global Land Service (CGLS) has "a multi-purpose service component" providing a series of bio-geophysical products on the status and evolution of land surface at global scale, such as the SSM CGLS 1 km, namely surface soil moisture (in terms of saturation degree) at 1 km (1°/112) spatial sampling. The SSM CGLS 1 km is derived from microwave radar data observed by the Sentinel-1 SAR satellite sensors (C- band) with a temporal resolution over Europe of 1.5-4 days starting from 2016 (the temporal resolution was about 3-8 days before 2016), when both Sentinel 1A and B became available.
The Sentinel-1 backscatter value, terrain-geo-corrected and radiometrically calibrated, is used to obtain soil moisture applying an adaption of the TU-Wien-Change-Detection (Wagner, 1998). The algorithm modified by Pathe et al. (2009), has been used both for low resolution ERS and ASCAT data and for higher resolution SAR validating it over Australia, Africa and large parts of South America (Algorithm Theoretical Basis Document CGLS SSM 1 km, Bauer-Marschallinger et al., 2019).

**Improved S-1 SSM:** an enhanced version of a 1 km SSM dataset, obtained by applying a change to the original method on S-1 data, was made available for this study from the Department of Geodesy and Geoinformation of TU Wien. The improvements derived from the application of Quast et al. (2019) generic first-

order radiative transfer model on S-1 data. With this model authors have tried to represent the scattering as combination of bare soil $\sigma^0_s$, soil covered by vegetation $\gamma^2\sigma^0_s$, vegetation $\gamma^2\sigma^0_v$and their interaction scattering $\sigma^0_{int}$, as shown in Fig. 17.

$$\sigma^0 = \sigma^0_s + \gamma^2\sigma^0_s + \gamma^2\sigma^0_v + \sigma^0_{int} \quad \text{Eq. 35}$$

Where $\gamma$ is a factor of attenuation.
A parameter accounting for the "effective bare-soil fraction" is included in order to take into account all of these contributions as well as the fact that the observed scene often encompasses both areas of intense vegetation-cover and effectively bare soil sections. Additionally, the bidirectional reflectance distribution function (BRDF) of the soil surface is used to describe the bare soil contribution using parametric functions.

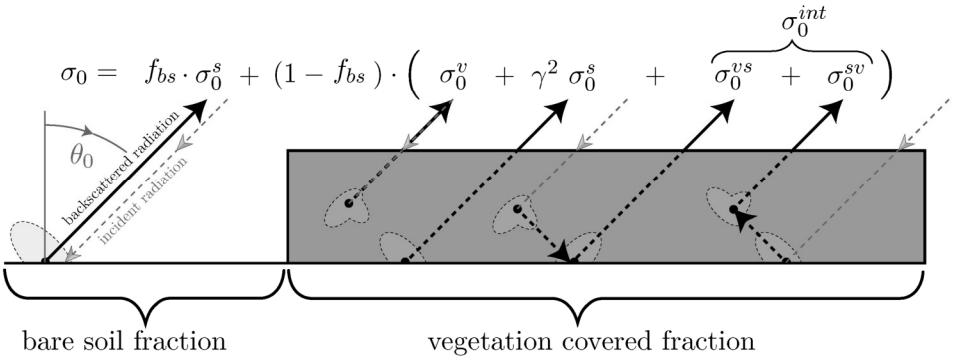


Fig. 17: Contributions to the backscattered signal.
Data Source: Quast et al., 2019.

The creation of a backscattering model must take into account both the coarse spatial resolution (in the order of kilometers) and the constrained computing complexity (that may be employed to undertake large-scale simulations over lengthy time periods). Therefore, it is obvious that the functional representation of the scattering behavior must inevitably subsume many different aspects of both soil and vegetation into a constrained set of parameters given the coarse resolution of scatterometers and the constrained number of independent observables.

The solution proposed by Quast et al. (2019) on the basis of their previous works (Quast and Wagner, 2016) utilized a linear combinations of generalized Henyey and Greenstein (1941) (HG), defined as function of a single parameter, which could be used to mimic the pattern of an isotropic. In particular, they have tested the model on 158 sites in France and on ASCAT retrievals using for the vegetation scattering a linear combination of three HG a forward-scattering contribution, a bounce-off contribution in specular direction, and an isotropic contribution. Also, for the BRDF, thus for the bare soil contribution of coarse-resolution monostatic scatterometer measurements within reasonable accuracy, they provided a parametric description that can be obtained by adjusting the HG function.

$$BRDF(N,t,a) = \frac{N}{R_0(t,a)} HG(t,\widetilde{\Theta}_a) \quad \text{Eq. 36}$$

- $N$ is Nadir hemispherical reflectance of $BRDF$. This information is linked with the SM: N =$s_2$SM, where $s_2$ is constrained by ensuring that the resulting range of $N$ remains physically plausible.
- $R_0(t,a)$ is the Hemispherical Reflectance.
- $\widetilde{\Theta}$ is the scattering angle.
- $a$ is additional parameter belonging to [-1;1].
- $t$ is asymmetry-factor of the used BRDF representation which regulates the pattern (e.g., t =0 rough).

Therefore, the data not already free available for the period 2017 January – 2022 July are in terms of Nadir hemispherical reflectance (N) and in Equi7grid.

#### 3.2.1.1 Equi7grid

The Equi7grid format emerged from the necessity to efficiently store high-resolution satellite information while maintaining geometric accuracy. This format has been designed to strike a balance between data volume and acquisition time. It identifies seven global continental zones, each based on an equidistant azimuthal

projection system (ellipsoidal WGS84 datum). These zones are not necessarily aligned with traditional continental boundaries such as "Europe" but are defined based on the basis of equidistant azimuthal projection zones that cover different parts of the Earth's surface. Each continental zone within Equi7grid has its own reference system based on the Equidistant Azimuthal projection. Metric coordinates in the projected plane are referenced to the lower-left corner of the respective zone. The Equi7grid format comprises three levels of grids, each with its own extent and sampling resolution (Bauer-Marschallinger et al., 2014):

- T6 Grid Level: This level covers an extent of 600 km and supports sampling ranging from 1000 meters down to 64 meters.

- T3 Grid Level: Encompassing a 300 km extent, this level supports sampling ranging from 60 meters down to 20 meters.

- T1 Grid Level: With an extent of 100 km, this level supports sampling ranging from 16 meters down to 1 meter.

The definition is available at https://github.com/TUW-GEO/Equi7Grid.

### 3.2.2 Ground-based data

#### 3.2.2.1 The European ISMN network

The European ISMN network is composed of 28 station networks that are not evenly distributed and some of which are not operational (Dorigo et al., 2021). SM data are provided at several depths depending on the site in terms of VWC $m^3/m^3$ and are accompanied by quality flag indicators. We chosen only the ISMN stations within the selected ecoregions having SM measurements at a depth of 5 cm (assumed as satellite microwave sensing depth (Qiu et al., 2016)), from January 2015 to December 2020. In addition, only measurements flagged as "good" and with the VWC between 0-0.6 $m^3/m^3$ were considered (Dorigo et al., 2013; Al-Yaari

et al., 2019). Among the existing networks, nearly 200 ground stations are available representing the 16 ecoregions reported above (Fig. 16). Table 5 summarizes some features (Dorigo et al., 2021) of the chosen networks (name, location, number of gauge stations and activity status).

Table 5: Local networks included in the ISMN that have been adopted in the intercomparison.

| Name | Location | n.stations | Status |
|---|---|---|---|
| WSMN | UK | 8 | Running |
| UMBRIA | Italy | 13 | Running |
| TERENO | Germany | 5 | Running |
| SMOSMANIA | France | 22 | Running |
| Ru_CFR | Russia | 2 | Running |
| RSMN | Romania | 20 | Running |
| REMEDHUS | Spain | 24 | Running |
| HYDROL NET_PERUGIA | Italy | 2 | Running |
| HOBE | Denmark | 32 | Inactive |
| HOAL | Austria | 33 | Running |
| FR_Aqui | France | 5 | Running |
| FMI | Finland | 27 | Running |
| BIEBRZA_S-1 | Poland | 30 | Running |

The ISMN is given by the combination of several networks which are managed by individual institutes or agencies. This leads to a heterogeneous distribution of the monitoring stations which are clustered in specific locations. In the following more details are included for each ecoregion and relative ground stations local network(s) that fall within:

- The Italian sclerophyllous and semi-deciduous forests (795) share the Umbria network with the Appenine deciduous montane forests (644), which also contain the HYDROL-NET_PERUGIA. In both cases stations are located in the Central part of Italy.

- The Romanian monitoring network, RSMN, covers five ecoregions: the Balkan Mixed forests (646), the Pannonian mixed forests (674), the Pontic steppe (735), the East European forest steppe (661), and the Central European mixed forests

(654). The ground-based monitoring stations are located respectively on the border with Bulgaria; between Romania and Hungary; in the Black Sea region of Romania and finally on the border with Moldova for both the 661 and 654 ecoregions. In addition, the Central European mixed forests (654) host the BIEBRZA_S-1 network, located in northern Poland.

- The Celtic broadleaf forests (651) is described by the WSMN network which is located in the United Kingdom.

- The European Atlantic mixed forests (664) overlap with the Baltic mixed forests (647) in the Hobe monitoring network and with the Northeast Spain and Southern France Mediterranean forests (799), Western European broadleaf forests (686), and Cantabrian mixed forests (648) in the SMOSMANIA network. Furthermore, the European Atlantic mixed forests and Western European broadleaf forests (686), which encompasses the HOAL monitoring network, also share the TERENO network. The SMOSMANIA network extends to the Mediterranean coasts (799) and covers the Occitania (664) and Aquitaine (686 and 648) regions, while the HOBE network is centered in Denmark and the HOAL network is centered in Austria. The Aquitaine region has additional monitoring capabilities through the Fr_Aqui network, which is integrated into the Cantabrian mixed forests (648).

- The Sarmatic mixed forests (679) encompass the Ru_CFR network which belong to Russian area.

- The Scandinavian and Russian taiga (717) include the FMI network which covers a northern part of Finland.

- The Iberian sclerophyllous and semi-deciduous forests (793) is monitored by the REMEDHUS network, mostly located in the northern part of Spain.

### 3.2.2.2 COSMOS- Alento network

The COSMOS Alento network, comprising stations situated within the Alento River Catchment (ARC). The ARC represents a long-term ecological infrastructure network that forms a constituent part of the TERENO (TERrestrial ENvironmental Observatories) long-term ecosystem infrastructure network. This network is located in the southern Italy's Campania region, as outlined in the works of (Nasta et al., 2020a, 2020b). In alignment with the objectives of this study, two specific sub-catchments within the Upper Alento River Catchment (UARC) were selected. The UARC is a mountainous section of the ARC characterized by a drainage area of approximately 102 $km^2$. Its downstream limit is defined by the presence of the earthen dam known as "Piano della Rocca," as detailed in the findings of (Nasta et al., 2017). The chosen sub-catchments are denoted as MFC2 and GOR1. These sub-catchments exhibit the subsequent measured attributes:

Table 6: Man features of the two subcatchments MFC2 and GOR1.

| Station | Lon | Lat | $d_1$[mm] | $n_1$ | $n_2$ | $d_2$ | WP | FC | P[mm/year] |
|---|---|---|---|---|---|---|---|---|---|
| GOR1 | 15.229 | 40.311 | 50 | 0.652 | 0.652 | 27 | 0.215 | 0.384 | 1255 |
| MFC2 | 15.184 | 40.365 | 50 | 0.56 | 0.56 | 21 | 0.262 | 0.38 | 1215 |

All parameters utilized in this study were derived from the comprehensive basin analysis as detailed in Nasta et al. (2020a). In the instance of porosity, a mean value was reported alongside the minimum and maximum values encompassing the range. Nevertheless, our decision was to utilize the mean value for both layers.

### 3.2.3 Modelled data: ERA5-Land dataset

The development of a technique for parameter extraction and later validation of the produced products was required for the study's second phase, i.e., the SCAT-SAR SWI SMAR application. This goal's fulfillment required the use of the ERA5-Land dataset. We may get a wide variety of data thanks to the features of this

dataset, which are discussed in Chapter 2. Notably, it provides crucial details like precipitation, which is necessary for the SMAR application to define losses, as well as data on soil moisture at various depths. Additionally, a downscaling procedure was carried out utilizing RStudio's KrigR package (Davy and Kusch, 2021; Kusch and Davy, 2022) for regional-scale confirmation of our results. By taking this step, we were able to improve the localized accuracy of our evaluation and the SM data going from a resolution of 9 km to 1 km.

KrigR is an R studio toolbox for statistical downscale which takes as covariates some soil parameters from the global dataset of the Land Atmosphere Interaction Research Group at Sun Yat-sen University. The Land Atmosphere Interaction Research Group (Dai et al., 2013) dataset was derived from multi-PTFs (pedotranfer functions) estimation. It includes the parameters in the Clapp and Hornberger Functions (FCH) (Clapp and Hornberger, 1978), and in thermal dynamic equations, respectively. The median of the estimation is provided. The vertical variation of soil property was captured by eight layers to the depth of 2.3 m (i.e., 0- 0.045, 0.045- 0.091, 0.091- 0.166, 0.166- 0.289, 0.289- 0.493, 0.493- 0.829, 0.829- 1.383 and 1.383- 2.296 m). The parameters are:

Table 7: Parameters for the ERA5-Land downscaled from 9 km to 1 km implemented in krigR package.

| Parameter | Symbol | Units |
|---|---|---|
| Saturated water content of FCH | $\theta_s$ | $cm^3/cm^3$ |
| Saturated capillary potential of FCH | $\psi_s$ | cm |
| Pore size distribution index of FCH | $\lambda$ | - |
| Saturate hydraulic conductivity of FCH | $K_s$ | cm/day |
| Heat capacity of soil solids | $c_{soil}$ | J/ ($m^3$ K) |
| Thermal conductivity of saturated soil | $\lambda_{SAT}$ | W/ (m K) |
| Thermal conductivity for dry soil | $\lambda_{DRY}$ | W/ (m K) |

The approach implemented in the R package follows a two-stage process. In the first stage, variograms are fitted to the variable of interest and native covariates at

a resolution of 9 km. This involves estimating the spatial correlation between the target variable and the covariates at the given resolution using variograms. In the second stage, target covariates at a 1 km resolution are combined with the functions estimated in the first stage to obtain the downscaled variable (in this case, ERA5-Land at a 1 km resolution). The use of variograms and covariate functions can be a useful approach to estimate the target variable at the desired resolution. However, it is important to note that the accuracy of the estimate depends on the quality of the covariates used and their spatial correlation with the target variable.

### 3.3 Intercomparison of recent Microwave satellite Soil Moisture Products

Apart from a large series of works focused on the comparison between remote and in situ SM measurements at the single scale of the satellite pixel encompassing the ground station/s (Lacava et al., 2012), others have been conducted at a regional and/or global scales (Ray et al., 2017; Brocca et al., 2011), extending at the selected larger spatial scale achievements related to the ground-based measurements, regardless of their often heterogeneous spatial distributions. Among the works that focus on narrow specific areas such as in Spain, Italy, France or USA (El Hajj et al., 2018; Cui et al., 2017; Brocca et al., 2011), many of them present comparisons of different SM datasets with in-situ data, showing not homogeneous results, depending on the data considered, as well as on the specific site-condition of the area analyzed. For example, ASCAT performed better than AMSR-E in Spain, Italy, and France (Brocca et al., 2011), SMAP was found better than the other sensors in Spain and USA by Cui et al. (2017), while the work by El Hajj et al. (2018) highlighted the relevant impact of Radio Frequency Interference (RFI) on SMOS product performances.

Other studies at continental/global scale (Min et al., 2022; Liu et al., 2019; Colliander et al., 2017) tried also to include in the analysis factors, such as climate and/or vegetation characteristics, that might change on the basis of the considered

scale of investigation and cause the above-mentioned discrepancies among different regions (e.g., Al-Yaari et al., 2014). In particular, Al-Yaari et al. (2019) conducted a global study at three levels considering: the five continents first, the Koppen- Geiger climatic zones (Rubel et al., 2017) and finally at the vegetation scale, referring to International Geosphere-Biosphere Programme (IGBP) land cover classification (Friedl et al., 2010). The study evidenced that satellites have variable performance in Europe, which deserves further investigation. However, Min et al. (2022) evidenced that one issue that may significantly affect the comparison in Europe is represented by the Radio Frequency Interference - RFI.

It is worth saying that while climate and soil can be considered as external factors, the soil moisture dynamics (Section 2.7) depends on the reciprocal links between vegetation and water availability (Porporato and Rodriguez-Iturbe, 2002), hence the analysis carried out considering separately variables such as vegetation or climate did not allow to fully assess SM performances. On the contrary, taking into account the combination of climate and vegetation could allow to better understand which one or which combination of factors introduces errors in the microwave SM products, as well as justifying why Europe (EU) had poor (in same cases) and a diversity of performance in previous studies.

In addition, the choice of the reference scale is also a critical issue which may impact on the performance assessment. For instance, the field scale appears too specific to guide on the choice of a satellite product, while global intercomparisons generalize the problem too much, making comparison not always easy. By contrast, the first phase of the present study, starting from the results of Al-Yaari et al. (2019), investigates the behavior of SSM products in EU by implementing an intercomparison assessment in areas delineated according to the combination of different flora, fauna, and climatic characteristics, i.e., the EU ecoregions. Indeed, the study aims to advance in the assessment of the different role of the above-

mentioned factors and of their relationships in EU, trying to provide indications for the SM satellite retrievals in Europe for various applications at scale of ecoregion. Thus, the area of the intercomparison is bigger than the Mediterranean area, but the cluster chosen allows to preserve the peculiarity. Effectively, ecoregions are defined as relatively large land areas characterized by a peculiar assemblage of natural communities and species, with boundaries that approximate the original extent of natural communities prior to major land-use change (Olson et al., 2001). The use of ecoregions for SM assessment, here for the first time applied in Europe, has been already tested in USA by Baldwin et al.(2017), demonstrating its feasibility, because the variability of SM with respect to the ground measurements within each ecoregion was found lower that the one from neighboring ecoregions.

The SM satellite products analyzed are SMAP L4, SMOS-IC, ASCAT (H115 & H116), the CGLS SSM 1 km and the ESA CCI, each of them was selected as the most up-to-date version of the products at the time of investigation and representative of different technologies (i.e., active or passive sensors) and approaches (i.e., modelled and/or blended) at different spatiotemporal resolution in the period from January 2015 to December 2020. Two years of measurements were at least available for all the considered SM products in such a 5-year temporal interval.

Our analysis compares the SM time series extracted from the original grids (e.g., 9 km for SMAP L4, 25 km for SMOS-IC) for those pixels that correspond to each station separately (based on its latitude and longitude). It is possible that some stations in a dense network correspond to the same passive (SMAP, and SMOS), blended (CCI) pixel and several active (ASCAT) pixels. SM satellite retrievals were matched with instantaneous in situ measurements within a time window of 1 h and the pairs are aggregated in a "daily" time step. The metrics between satellite data

and the in-situ observations were then computed separately for each station. Finally, the median of each metric for all stations within an ecoregion was calculated.

It is notable to mention that the different re-mapping grids of satellite data (e.g., WARP, SMOS, Quarter-Degree-Grid) as well as the scale discrepancies between in situ and satellite data, might have impacted the uncertainty of our results, in addition to the aggregation at ecoregion scale (as the largest homogeneous area potentially investigated) accordingly with the concept of temporal stability already discussed in Section 3.1. However, this issue is out of the scope of the present work and, therefore, it isn't further investigated here.

Three main scores, widely used within the SM community (Zheng et al., 2022; Peng et al., 2021; Al-Yaari et al., 2019; Entekhabi et al., 2010), were considered to evaluate remotely sensed SM products accuracy: Pearson Correlation Coefficient (r), bias, and unbiased root mean square error (ubRMSE). r is unconcerned with any bias in the mean or magnitude of the variations; while the ubRMSE is a measure of accuracy after removing of sensitivity to distortions in both mean and amplitude of fluctuations, exploiting bias. This latter metric incorporates the RSME, which removes only the amplitude of fluctuation (Entekhabi et al., 2010). Please, see Zheng et al., 2022; Peng et al., 2021; Al-Yaari et al., 2019 for the formulation.

The performance of the analysis carried out considering an historical series may be positively affected by the seasonal cycle (K Scipal et al., 2008). Therefore, we have also considered to evaluate SM anomalies, computed, for example, as proposed by Rodriguez-Fernández (2016) on the basis of a 35-day moving window (w) (Brocca et al., 2011) in order to better assess the accuracy of the SM products.

$$\mathrm{SM(t)}_{\,\mathrm{ANOM}} = \frac{\mathrm{SM(t)} - \overline{\mathrm{SM(t-17:t+17)}}}{\mathrm{sigma_{SM}(t-17:t+17)}} \qquad \text{Eq. 37}$$

where the anomalies ($\mathrm{SM(t)}_{\,\mathrm{ANOM}}$) could be generically referred to the satellite (SAT) or the in situ (ISMN) SM time-series, and computed as deviation of a measured

acquired at time (t) from the SM mean $\overline{\overline{SM(t)}}$ evaluated on a temporal interval ranging from previous 17 day before (t) and next 17 days after (t). Such a deviation is weighted by the SM standard deviation (sigmaSM) computed on the same period. Such a formulation allows for a rough reduction of seasonality effects, and hence to analyze short-term variations. To completely remove the seasonality, we should consider a long-term analysis that will be proposed in a companion study.

SM anomalies are first exploited to detect outliers, finding, and discarding the outer fences of the satellite SM anomalies dataset with the quartiles method (Walfish, 2006). Then, consistently with previous SM assessment, the metric such as the Pearson Correlation Coefficient ($r_{ANOM}$) are evaluated on a single station and then aggregated at the ecoregions scale using as a reference value the median.

### 3.4 Seasonality effects on the intercomparison of satellite Soil Moisture products

The intercomparison of Section 3.3 will give results, which allow us to ask how seasonality can influence the performance of microwave satellite SM products. Thus, the study of seasonality could better explain the ecoregions pattern.

In long term analysis, the SM signal can be considered the sum of two main factors: a seasonal one due to the natural fluctuations caused by the rainfall and evaporation cycle, and anomalies caused by extreme weather conditions, land management, or human activities. In signal decomposition, SM anomalies are residuals which can be categorized as short-term or long-term variations depending on their relationship with seasonality (i.e., on how the seasonality is computed). Short-term anomalies are considered to be higher-frequency, sub-seasonal SM variations that represent short-term drying and wetting events. In contrast, long-term anomalies contain information about both short-term drying and wetting events and seasonal deviations from the long-term mean seasonal cycle, referred to as SM climatology (Gruber et al., 2020). SM climatology is an important consideration for spatial models of SM and long-term temporal variations (Chakravorty et al., 2016).

Calculating the long-term SM variation to remove seasonality completely requires historical data records spanning several decades (Dorigo et al., 2012), which are often not available. Therefore, in the literature, short-term variations are usually investigated when comparing SM satellite products. One widely recognized approach in the SM community is the use of a moving window, typically spanning several weeks (Chen et al., 2017; Albergel et al., 2012), although this approach does not allow for complete removal of seasonality. Current research has estimated biases and uncertainties assuming that SM data are stationary (i.e., constant over time). However, the quality of SM data can vary greatly from season to season, and many applications could benefit greatly from temporally varying information.

In addition, because of the strong link between the quality of SM data and vegetation (Gruber et al., 2019b; Van der Schalie et al., 2018; Zwieback et al., 2018), the study of its temporal/seasonal variation is an open field of remote sensing research.

This is important for our research since each ecoregion is a relatively large area, and its climate variability is influenced by plant growth and transpiration, i.e., by the soil-plant system. Therefore, it is necessary to include an analysis of plant phenology, the development of vegetative and reproductive plant organs (Haugaasen and Peres, 2005), focusing especially on the timing of bud break, active growth, growth cessation, and dormancy release. Vegetation phenology has been widely studied at a large scale through remote sensing using spectral indices to investigate its relationships with the climate system (Keenan et al., 2014; Myneni et al., 1997). However, there are few studies linking SM and phenology, due to the inherent limitations of acquiring reliable SM data when dense vegetation is present. In summary, the effect induced by the phenological cycle on SM dynamics should affect its seasonality in long-term time series.

Two parallel lines are developed in this part of the study: first, the Robust Satellite Techniques (RST - Tramutoli, 2007) approach, that has been applied to the long-term series of the SM products to completely remove seasonality, and then the

achieved results, namely the performance of the detected anomalies with in-situ measurements, have been compared with those already obtained by computing signal anomalies in the 35-day moving window. RST is an advanced methodology for the multitemporal analysis of satellite data that has already been applied to microwave data to provide useful information on SM variability at different spatiotemporal scales (Manfreda et al., 2011; Lacava et al., 2005). By analyzing satellite data acquired under homogeneous observational conditions (i.e., same location, same month of the year, same acquisition time), the approach is able to effectively separate the climatological signal from short-term signal fluctuations (Di Polito et al., 2016; Tramutoli, 2007). The choice of this methodology over others is related to the fact that for its proper application three years of continuous measurements at monthly scale are enough (Koeppen et al., 2011).

Concerning the second line, focusing instead on seasonality (without its removal), and considering that vegetation preserves the memory of soil moisture, a more in-depth analysis of the relationship between the hydrological process and the phenological cycle for the ecoregions has been carried out. This allowed us to assess if the combination of SM dynamics and macro-scale analysis of the phenological cycle resulted in a better understanding of satellite remote sensing ability in ecoregion detection. The study has considered the average growth and dormancy phase for each ecoregion to investigate the occurrence of wet or dry soil conditions, taking into account the different weight of hydrological processes depending on daily, seasonal or interannual fluctuations. Fig. 18 shows the general workflow.

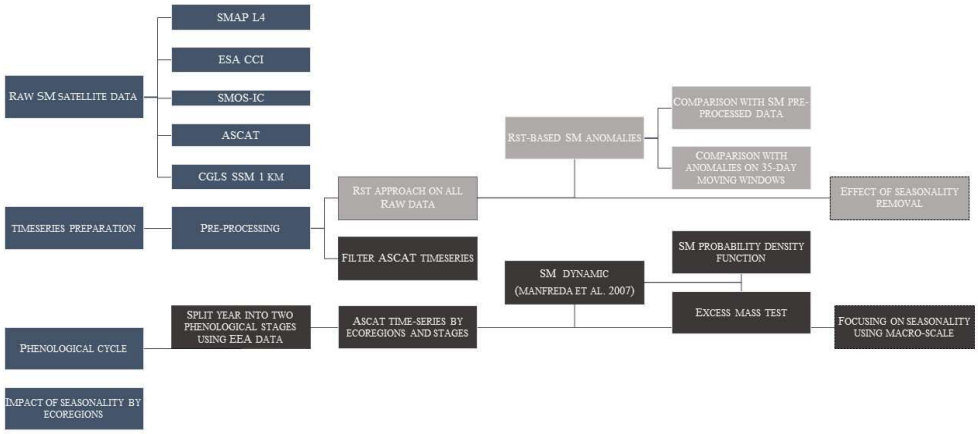


Fig. 18: General workflow of the study of effect of seasonality on the intercomparison.

The dark blue boxes highlighted the common parts to both the analyses, while the light grey steps/outputs for the first line and finally the dark gray for the second. The core steps thus have included: i) data preparation; ii) the RST application and iii) the comparison of the RST-based anomalies with both the original data obtained after the pre-processing for each satellite product and with the 35-day moving window anomalies; iv) the detection of growth and dormancy phases through the European Environment Agency (EEA) data and the evaluation of SM dynamic by phases and ecoregions on ASCAT data.

### 3.4.1 The Robust satellite technique approach

The RST approach is a general satellite data analysis methodology, already applied with successful results for the mitigation of different environmental and natural hazards, and also related to the hydrogeological cycle (Lacava et al., 2010, 2019). Two main steps form the basis of RST implementation: i) the long-term characterization of the signal under investigation in terms of expected value and normal variability and, ii) a change detection step aimed at identifying statistically significant signal anomalies. The first step requires the preliminary collection of

long-term satellite data records acquired under homogenous conditions (same month of the year, same hour of the day) at pixel (x,y) level, which are later analyzed to identify the normal signal behavior, usually expressed in terms of temporal mean with its natural variability represented by the standard deviation. The second step involves the implementation of the Absolute Variation of Local Change of Environment (ALICE) Index, as described in the following equation (Tramutoli, 1998):

$$\otimes_V (x,y,t) = \frac{V(x,y,t)-V_{REF}(x,y)}{\sigma_{REF}(x,y)} \quad \text{Eq. 38}$$

where, in our specific case, the signal V is the SM measurement for each pixel of the investigated scene at (x,y) location and time (t); $V_{REF}$ and $\sigma_{REF}$, respectively, are the SM temporal mean and standard deviation computed on the investigated dataset for the same pixel. $V_{REF}$ and $\sigma_{REF}$ were computed considering data acquired over a long period in the same temporal domain (i.e., at a monthly scale) of the image under investigation. In our case, we considered the 2015-2020 period, hence, at the end of the analysis we generated 24 reference fields (1 temporal mean + 1 standard deviation for each calendar month). As already said, for reliable results, a time series of measurements spanning at least three years is required (Koeppen et al., 2011). As the ALICE index exhibits Gaussian behavior with mean ~ 0 and standard deviation ~ 1, the higher the absolute value measured, the lower the probability of occurrence (Tramutoli, 1998). Considering long-term time series under the same date-time-weather-climatic conditions allowed us to overcome possible site effects, known or not. During the generation of reference fields, values of signal outside the outer fence were excluded by a quartile analysis for each time-series (±3IQR), as done for anomalies on moving-window of 35 days.

We applied this technique to both ISMN ground-based measurements and satellite SM retrievals time-series used in Section 3.3. Subsequently, we computed the Pearson Correlation Coefficient, $r_{ALICE}$, and compared it with r and $r_{ANOM}$ from our previous study, to assess satellite performance using in situ data, and short- and long-term variations.

### 3.4.2 SM distribution analysis considering phenological cycle

The use of the probability density function to describe SM dynamics is a well-known approach in the scientific community (Laio et al., 2001; Rodriguez-Iturbe et al., 1999), with several works focused on extracting RZSM information from surface data. For instance, Manfreda et al. (2007) evaluated the conditional probability distributions of the deeper layer versus the saturation values of the surface layer (ranging from 15% to 100%) for an area in Oklahoma (USA). They identified three types of behavior: dry soil (bimodal distribution for saturation values below 45%), normal soil (Gaussian distribution below a saturation of 70%), and very wet soil (right skewed distribution for all other values). This led to the main conclusion that the uncertainty in predicting RZSM from SSM increases as the water content of the surface layer decreases.

Thus, using soil moisture distribution (i.e., the SM probability density function) we could better characterize ecoregion behavior based on the relationship between SM dynamics, vegetation, and water availability. Using the approach of Manfreda et al. (2007), we expected to better describe those ecoregions characterized by dry soil conditions, being able to infer information about the conditional probability of deep layer saturation. Indeed, in those ecoregions, the increased microwave penetration depth should allow us to obtain information from deeper layers (Singh et al., 2019; Lakhankar et al., 2009). On the other hand, ecoregions where soil is extremely wet or "normal" conditions are present, might not be clearly described by this approach. In any case, because measurements of RZSM and SSM are correlated, we could assume that the probability distribution of SSM saturation values is similar to that of RZSM, and therefore we can associate the surface layer with a Gaussian distribution under normal conditions and a distribution with strong right skewness under wet conditions.

Assuming these three behaviors based on SSM (dry/normal/wet), we evaluated the ASCAT SM probability distribution for each ecoregion by considering the

whole period under investigation as well as the growth and dormancy phases to better assess the relationship between phenology and soil moisture dynamics.

Plant growth stage was obtained by combining information about the start time of the vegetation growing season in the period 2000-2016 (https://www.eea.europa.eu/data-and-maps/data/annual-start-of-vegetation-growing) with data about the length of the vegetation growing season for the same temporal period (https://www.eea.europa.eu/data-and-maps/data/annual-above-ground-vegetation-season). The dormancy phase was considered the remainder of the year.

The start of the growing season 2000-2016 (SVGS) is a time series of daily raster files separated on the basis of the corresponding day of the year (DOY) and the derived linear trends (in day/year). This time series is based on the time series of the Plant Phenology Index (PPI) value, a vegetation index derived from the MODIS BRDF-Adjusted Reflectance product (MODIS MCD43 NBAR)(Jin and Eklundh, 2014). The PPI index is optimized for efficient monitoring of vegetation phenology and is derived from the acquired MODIS data using radiative transfer solutions applied to the reflectance in visible-red and near-infrared spectral domains. The product provides reflectance data for the MODIS "land" bands (1-7) adjusted using a bi-directional reflectance distribution function. This function models values as if they were collected from a nadir-view to remove so-called cross-track illumination effects. The start of season indicator is based on calculating the start of the vegetation growing season from the annual PPI temporal curve using the TIMES AT software for each year between 2000 and 2016. Vegetation growing season length 2000-2016 (VGSL) is a time series of raster files of the annual above-ground growing season length and the derived linear trends for the period 2000-2016. In this case, the considered signal is the PPI. The VGSL helped to detect the end of the growing season (EOS).

Finally, once we obtained the growth and dormancy phases, we tested the ASCAT SM distributions by applying the excess mass test, which assumes the multimodality

of the distribution as the null hypothesis, following the formulation of Ameijeiras-Alonso et al. (2019) in R programming language.

### 3.5 SCAT-SAR SWI SMAR application

The principal core of our work made during the period at TU Wien englobed the merging of ASCAT and enhanced S-1 SSM to produce the daily SCAT-SAR SWI dataset and the subsequent application of the SMAR model (SCAT-SAR SWI SMAR). The SCAT-SAR SWI SMAR is four-dimensional SM information with a daily temporal resolution and a 1 km spatial resolution for the surface and the root zone (30 cm). As said, it is required for many applications since the extreme and most relevant effects of climate change on natural hazards are directly linked to SM variability, whose spatiotemporal evolution can only be analyzed using information with adequate resolution. In fact, currently, there are no satellite SM products capable of providing indications with high temporal and spatial resolution, especially when studying large-scale areas and RZSM.

Thus, our SCAT-SAR SWI SMAR could address this gap by merging a high-temporal-resolution product (low spatial resolution) with a high-spatial-resolution product (low temporal resolution) to obtain high spatiotemporal resolution information to integrate into a physically based model. The SMAR application to go inside the soil profile is chosen since it is related to the soil properties (Section 2.7.3.3), which are essential to the hydrological-hydraulic processes. The potentiality of this framework will also rely on the use of open-source data to provide a product with the characteristics that are freely available.

Fig. 19 reports the workflow of the fusion with the SWI formulation and the subsequent application of SMAR.

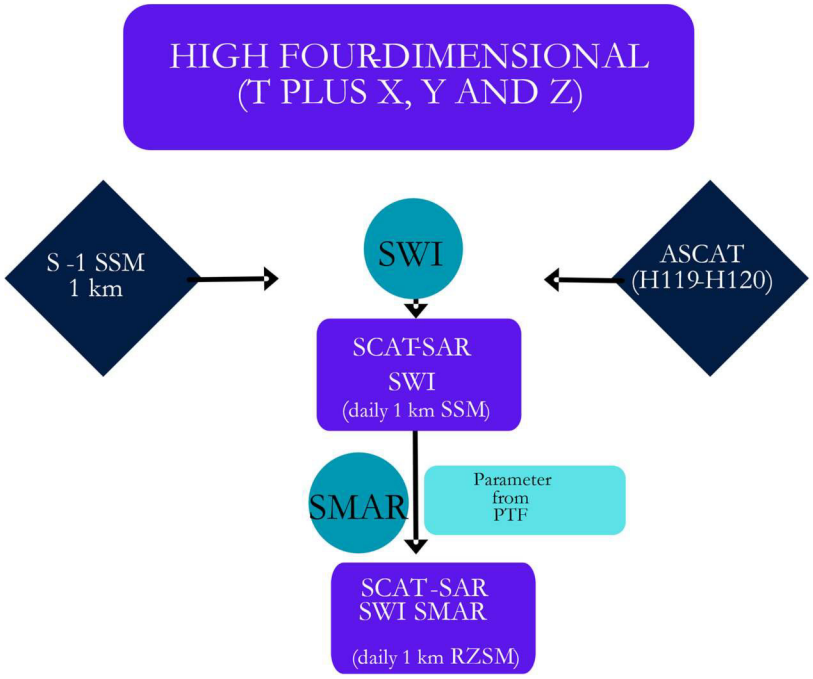


Fig. 19: Workflow of the SCAT-SAR SWI SMAR creation.

### 3.5.1 Fusion of ASCAT and SAR SSM

The concept of temporal stability in SM (Section 3.1; Section 3.3) is crucial, involving a strong correlation between a local signal and a regional signal from the surrounding area. Bauer-Marschallinger et al. (2018) based their algorithm modifications on this principle, as discussed in Section 2.7.3.2, building on the algorithm proposed by Wagner et al. (1999). As previously mentioned, their algorithm begins by assessing the matching parameters using CDF matching (Klaus Scipal et al., 2008). This step considers and corrects systematic biases that may arise from sensor and retrieval specifics, as well as complexities at the original scale that resemble land cover patterns (Fig. 20b). Subsequently, Eq. 30 is applied for fusion, followed by the masking of certain pixels, such as those corresponding to ice cover. In the work of Bauer-Marschallinger et al. (2018), ASCAT data (H101, https://hsaf.meteoam.it/Products/Detail?prod=H101 and H16,

https://hsaf.meteoam.it/Products/Detail?prod=H16) were resampled to a distance of 500 m to achieve a nominal spatial resolution of 1 km, matching that of S-1 SSM. This resampling was accomplished using the thin plate spline from the Python SciPy library.

However, our study involved a different approach. We have developed a code that initially operated at a point scale and was subsequently modified to adapt the data to a regional scale, operating on all the pixels of the specified area. The point-scale algorithm took the enhanced S-1 data (Section 3.2) in terms of N, normalized (using mix e max of the series) it to derive the improved S-1 SSM, and employed this as input alongside ASCAT H119-H120. The decision to utilize ASCAT as an input was supported by its utilization of the MW band (band C, similar to S-1) and the application of a change detection method (Section 2.5.1) to extract SSM information from backscattering.

In more detail, following the normalization of enhanced S-1 N to obtain the improved S-1 SSM, each pixel in the Equi7grid (x, y) was associated with the nearest ASCAT data record based on the grid point locator (GPI, https://dgg.geo.tuwien.ac.at/) corresponding to the pair (x, y), obviating the need for resampling. Consequently, moving from a point scale to a regional scale, we made the same step of N normalization and then generated the ASCAT time series of reference for each pixel, employing an average of its four neighboring GPIs weighted by their inverse distances, doing something similar to the resampling. Fig. 20 reports all the steps of the process (a) and the description of the utility of cdf-matching (b).

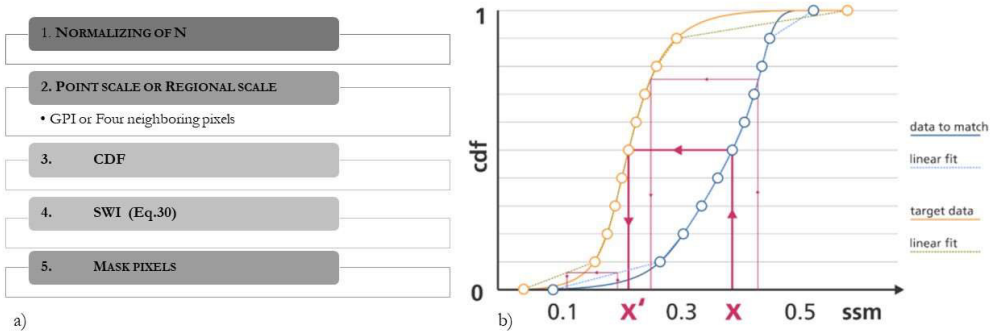


Fig. 20: Summary of the methods (a) and focus on the concept of CDF-matching for two time series at one pixel location (b). Data Source: CGLOPS1_ATBD_SWI1km-V1_I1.30.pdf.

### 3.5.2 SMAR model application

The application of the SMAR model, as discussed in Section 2.7.3.3, used physically based parameters ($s_{w2}, s_{c1}, a, b$), which can be empirically defined using soil texture. Specifically, $s_{c1}$, $s_{w2}$, and n are parameters that are closely linked to the characteristics of the soil texture. In the context of a two-layer soil profile, these parameters can be defined for both the surface soil (subscript 1) and the deeper soil (subscript 2).

At the point scale level, this distinction can be made when in situ measurements of porosity, WP or FC are available for both layers. However, for the sake of simplicity, we extracted these parameters (or the missing parameters among available) empirically from Table 3 of the Section 2.7.1, using USDA soil texture data (https://ldas.gsfc.nasa.gov/gldas/soils) for our area of interest. Consequently, we assumed that both layer 1 and layer 2 shared the same characteristics. With $s_c$, $s_w$, and n known, we can then derive the parameters 'a' and 'b' (as defined in Eq. 33). The parameter 'a' is derived under the assumption that all precipitation (mean annual precipitation) contributes to losses, while also considering a minimum rate

of $2\frac{cm}{year}$. This assumption was already used by Baldwin et al., 2019 as starting value to calibrate SMAR parameters in the Shale Hills Catchment.

$$V_2 = (Precipitation[cm]/365 + 2) \quad \text{Eq. 39}$$

At regional scale, precipitation data are obtained from the ERA5-Land dataset and oversampled at a 1 km resolution using the Python language. Once obtained these parameters, the SMAR algorithm is implemented within the cascade framework (Python language) of the previously mentioned fusion algorithm SCAT-SAR SWI (Section 3.5.1).

*Chapter 4*

# RESULTS AND DISCUSSION

In the previous chapter, we analyzed in detail the methodology applied in this work. We studied currently available SM measurement techniques on Eurasia to encompass the entire Mediterranean area. With the expertise acquired in the field of active sensors in the MW spectrum, we developed a high spatial and temporal resolution product over some areas of southern Italy. This estimation could contribute to mitigating the effects of climate change by intervening in the forecasting phase.

To emphasize the value of utilizing a physically based model, we will contrast the application of SMAR to acquire RZSM information with the use of SWI to obtain RZSM information.

This chapter is divided into three sections:

- Results of the intercomparison of SM satellite products versus ISMN ground-based measurements in the European ecoregions, covering Europe and some parts of Asia. This part involved data from the period 2015-2020.

- Building on the preceding results, we further investigate specific ecoregions that exhibit distinct patterns with a focus on seasonality. Our approach involves initially eliminating these patterns and subsequently analyzing them in the context of the phenological cycle, as outlined in Chapter 3. The datasets used in this section are consistent with those employed in the earlier phase of this study.

- Initially, we operate at a point scale using Alento COSMOS stations. Subsequently, we extended our analysis to a regional scale, leveraging data provided by TU Wien, which have not yet been made public. The temporal scope of this analysis spans from 2017 to 2022.

**4.1 Intercomparison on European ecoregions: the performance assessment**

The performances of SMAP L4, ESA CCI, SMOS-IC, ASCAT (H115 & H116) and the CGLS SSM 1 km with respect to in situ measurements from ISMN by ecoregions are shown in Fig. 21 in terms of median values of r, bias and ubRMSE using as refence period 2015-2020.

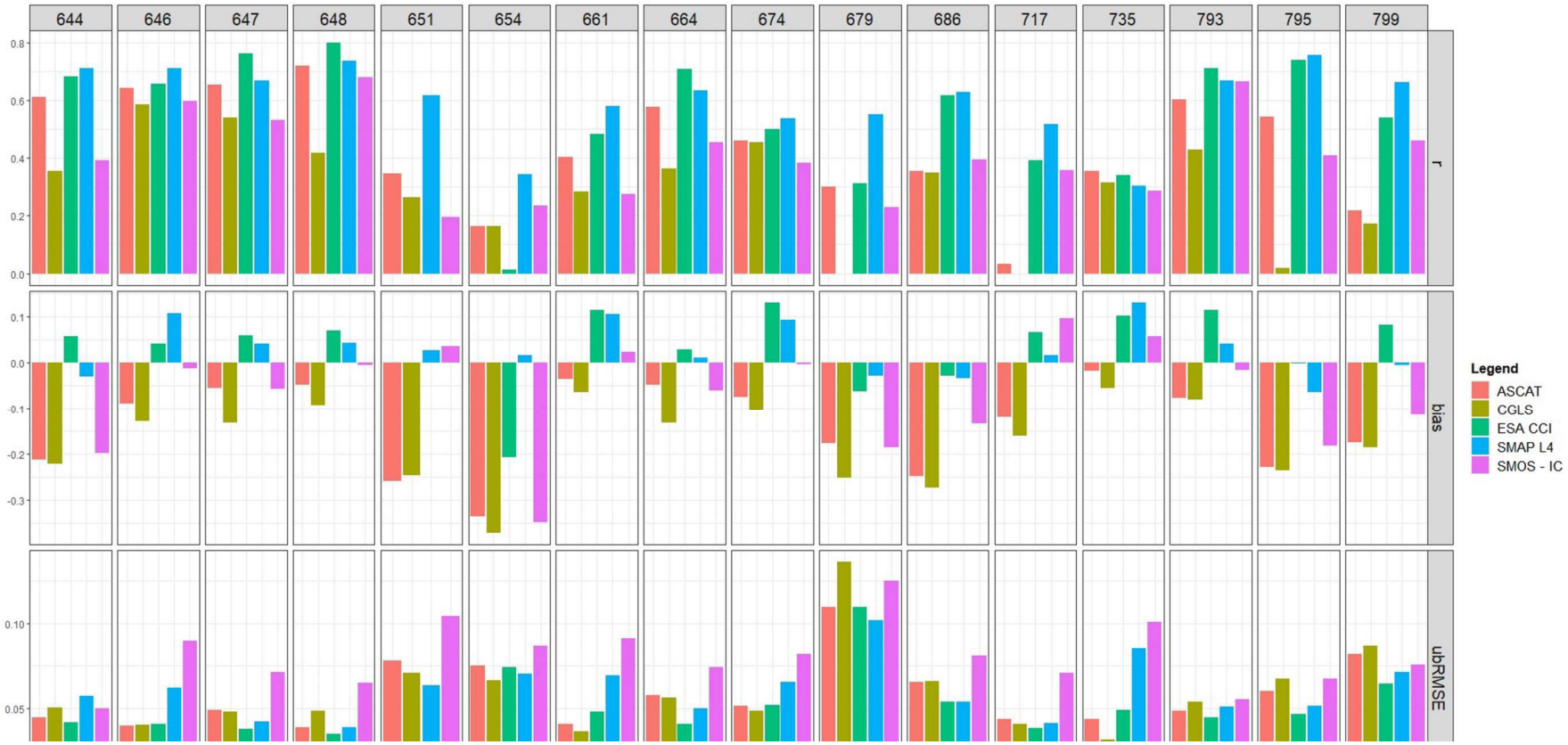


Fig. 21: Satellite products performances for each ecoregion: top panel r, middle bias and low ubRMSE.

The overall analysis demonstrated that the performances of each satellite product are strongly influenced by ecoregions' spatial heterogeneity, climatic conditions and land cover. All satellite products show weak performances for all metrics on i) the Pontic steppe ecoregion (735) and ii) the Central European mixed forest (654). It is worth mentioning that the ecoregions 735 and 654 are contiguous. In the following, we present the results of intercomparison between different RS products detailed for each metric. In terms of Pearson Correlation Coefficient, SMAP L4 showed the best performance in the most part (i.e., eleven) of ecoregions, ESA CCI in four and ASCAT performed better than the other satellite products on the Pontic steppe ecoregion (735), providing a correlation value of 0.36. On the other hand, CGLS SSM 1km showed the lowest correlations with ground data in the most part (i.e., ten) of ecoregions, SMOS-IC on five ecoregions and ESA CCI on the ecoregion 654 (where, as we said above, all SM products have weak performances). The CGLS SSM 1 km did not show any correlation in Sarmatic mixed forests (679) and Scandinavian and Russian taiga (717) ecoregions, obtaining an r close to 0. The SMOS-IC had variable correlations, with a value greater than 0.5 only on four of the 16 ecoregions considered in this study. Moreover, it is necessary to clarify that ESA CCI did not provide SM measurements for the considered period on the Celtic broadleaf forests ecoregion (651), where generally all SM satellite retrievals had unsatisfactory correlation except SMAP L4 ($r = 0.62$); and that we obtained meaningful correlation ($r>0.5$) for all satellite products in the Balkan (646) and Baltic (647) mixed forests.

SMAP L4 exhibited the lowest values of bias (in absolute terms ranging 0.03-0.05) on eight ecoregions, except for Balkan mixed forests (646), East European Forest steppe (661), Pannonian mixed forests (674), and Pontic steppe (735) where its performance fairly decreases until reach the worst performance in 735 respects to

all other satellite products. However, SMAP L4 confirmed its good performance also on Celtic broadleaf forests (651), i.e., the bias value was around 0.03, where other remote sensing products showed higher bias values. On three ecoregions (i.e., 646, 686 and 795) ESA CCI showed a complementary behavior to SMAP L4, obtaining the lowest value of bias. ASCAT achieved an overestimation on all ecoregions and had a better bias (i.e., close to 0) than the others on the Pontic steppe ecoregion (735) but it obtained the worst bias (- 0.26) in Celtic broadleaf forests (651). SMOS-IC achieved the best performance in terms of bias only in four ecoregions (648, 661, 674, 793), while CGLS SSM 1 km had the worst values in most part of ecoregions, with a maximum value of – 0.37 on Central European mixed forest (654). More in general, a negative bias for all products was found for Sarmatic mixed forests (679) and Western European broadleaf forests (686). Instead, all remotely sensed products have a bias close to 0 in Cantabrian mixed forests (648).

In terms of ubRMSE, ESA CCI showed the best performance in most part of ecoregions as reported in Table 9; the SMAP L4 maintained a ubRMSE always comparable to ESA CCI, achieving the lowest ubRMSE in the 651 and 679 ecoregions. SMOS-IC achieved the worst bias in the most part (eleven on 16) of the ecoregions, while ASCAT and the CGLS had variable performances according to the ecoregions.

Furthermore, we also evaluated the correlation between SM anomalies ($r_{ANOM}$) computed using a moving window of 35 days, both calculated on situ and satellite data, to assess whether seasonality could have affected results in the different ecoregions. SMAP L4 achieved a meaningful correlation on anomalies ($r_{ANOM}>0.5$) in five ecoregions (644, 646, 648, 654, 674). ESA CCI had a positive correlation on three of ecoregions (647,648,795), ASCAT on one (664), and the others had non-

meaningful correlation. The SMOS-IC and the CGLS SSM 1km had a nonpositive correlation.

Focusing specifically on comparing r and $r_{ANOM}$ (hereafter referred to as $r/r_{ANOM}$), Table 8 displays the Pearson Correlation Coefficients achieved for anomalies ($r_{ANOM}$) for each sensor in each ecoregion, in comparison with those achieved on the original time-series data (r). It's worth noting that the r values in Table 8 may differ slightly from those in Fig. 21, as they were recalculated after removing outliers with the quartiles' method (as described in methodology section). Previous studies (Brocca et al., 2011, Scipal et al., 2008) have shown that, when high seasonality is present, r tends to be greater than $r_{ANOM}$. As expected, removing the seasonal effect typically resulted in a decrease in correlation, with $r_{ANOM}$ being lower than r (as shown in the white rows of Table 8). On the other hand, an increase in the correlation between $r_{ANOM}$ and r is indicative of high signal variability or poor sensor quality in detecting SM-related signals (as shown in the dark gray rows of Table 8), considering the adopted screening out of anomaly-outliers. In Table 8 we have also reported the values of r and $r_{ANOM}$ for each satellite aggregated at the EU continental scale, aggregating correlations by median. Examining this median value of the r and $r_{ANOM}$ by satellite, the effect due to the procedure of screening out anomaly-outliers, was lost on the aggregation at European scale (see last line of Table 8). It confirms that the ecoregion scale is optimal for obtaining valuable information about the performance of satellites that would otherwise be lost. Probably, this is due both to the scale, neither too large nor too small but also to the combination of the factors from which the ecoregion originates (e.g., climate or vegetation

Table 8: Performance obtained on each ecoregion in terms of r and $r_{ANOM}$. The increasing in the correlation between $r_{ANOM}$ and r is colored in dark gray.

| | ASCAT | | CGLS | | ESA CCI | | SMAP L4 | | SMOS-IC | |
|---|---|---|---|---|---|---|---|---|---|---|
| Ecoregions | r | $r_{ANOM}$ | r | $r_{ANOM}$ | r | $r_{ANOM}$ | r | $r_{ANOM}$ | r | $r_{ANOM}$ |
| 644 | 0.6121 | 0.3629 | 0.3576 | 0.2112 | 0.6788 | 0.4204 | 0.71 | 0.5177 | 0.3905 | 0.3209 |
| 646 | 0.642 | 0.4058 | 0.5762 | 0.4163 | 0.6577 | 0.4842 | 0.7111 | 0.5466 | 0.5868 | 0.3496 |
| 647 | 0.6532 | 0.4435 | 0.5443 | 0.2468 | 0.7602 | 0.5467 | 0.6685 | 0.4547 | 0.5293 | 0.3165 |
| 648 | 0.721 | 0.5907 | 0.4663 | 0.424 | 0.7991 | 0.6105 | 0.7364 | 0.5866 | 0.6957 | 0.5079 |
| 651 | 0.2919 | 0.3228 | 0.037 | 0.3589 | No data available | No data available | 0.6224 | 0.4311 | 0.1536 | 0.1993 |
| 654 | 0.1892 | 0.3586 | 0.1636 | 0.2695 | 0.0446 | 0.313 | 0.343 | 0.5462 | 0.1771 | 0.4713 |
| 661 | 0.3988 | 0.4834 | 0.2801 | 0.4592 | 0.4806 | 0.4814 | 0.5797 | 0.4899 | 0.2726 | 0.3763 |
| 664 | 0.5773 | 0.4121 | 0.3565 | 0.3085 | 0.7132 | 0.4781 | 0.6341 | 0.4359 | 0.4626 | 0.2466 |
| 674 | 0.4576 | 0.4156 | 0.4564 | 0.3988 | 0.4903 | 0.4477 | 0.5394 | 0.5056 | 0.379 | 0.3113 |
| 679 | 0.2946 | 0.1712 | 0 | 0.3657 | 0.3125 | 0.2821 | 0.5514 | 0.3718 | 0.2362 | 0.1796 |
| 686 | 0.351 | 0.2202 | 0.3417 | 0.113 | 0.6107 | 0.357 | 0.6262 | 0.3772 | 0.3876 | 0.2175 |
| 717 | 0.0409 | 0.0859 | 0 | 0.0915 | 0.4043 | 0.3705 | 0.5845 | 0.4175 | 0.3162 | 0.3473 |
| 735 | 0.3551 | 0.2198 | 0.3422 | 0.1061 | 0.3467 | 0.4258 | 0.3129 | 0.3863 | 0.2611 | 0.3797 |
| 793 | 0.6014 | 0.364 | 0.4513 | 0.2298 | 0.7083 | 0.4576 | 0.6681 | 0.4458 | 0.6669 | 0.3662 |
| 795 | 0.5443 | 0.479 | 0.0353 | 0.3431 | 0.7331 | 0.5038 | 0.7551 | 0.4286 | 0.4166 | 0.3876 |

| | | | | | | | | | | |
|---|---|---|---|---|---|---|---|---|---|---|
| 799 | 0.2233 | 0.1167 | 0.1582 | 0.1598 | 0.5365 | 0.2344 | 0.6618 | 0.3385 | 0.46 | 0.2359 |
| Median at EU scale | 0.4282 | 0.36345 | 0.34195 | 0.289 | 0.6107 | 0.4477 | 0.63015 | 0.44085 | 0.38905 | 0.3341 |

Table 9 shows the RS product that obtains best performance when comparing with in-situ measurements for each ecoregion using the different metric investigated. The overall results (please see last column) show a slightly higher performance of SMAP L4 and ESA CCI, probably due respectively to the use of ancillary data such as meteorological forcing and parameterization schemes (Tavakol et al., 2019) within advanced models or due to the combination of different satellite data. The overall lowest performance of SMOS-IC and of the high spatial resolution product CGLS SSM (1km) could be influenced by the strong RFI in Europe (Mohammed et al., 2016; Oliva et al., 2012) as reported in the literature by Bircher et al. (2012), El Hajj et al. (2018) and Ma et al. (2019), as well as surface effects (i.e., surface roughness, land-cover heterogeneity within the pixel) usually smoothed when observing at larger scale.

As showed in Fig. 21 and Table 8 (and in their summary in Table 9), in terms of Pearson's correlation coefficient, it was highlighted the complementarity SMAP L4 and ESA CCI in agreement with those found by Ma et al. (2019) at the global scale. However, we found in line with Cui et al. (2017) that SMOS-IC had good and comparable correlation over the REMEDHUS network used to describe the 793 ecoregion and in Denmark within the 647 ecoregion.

Table 9: Summary results of all performance (r, bias, ubRMSE, comparison between r and $r_{ANOM}$).

| Ecoregions | r | bias | ubRMSE | $r/r_{ANOM}$ | Overall |
|---|---|---|---|---|---|
| 644 | SMAP L4 | SMAP L4 | ESA CCI | SMAP L4 | SMAP L4 |
| 646 | SMAP L4 | SMOS-IC | ~~ASCAT~~ ESA CCI | SMAP L4 | SMAP L4 |
| 647 | ESA CCI | SMAP L4 | ESA CCI | ESACCI | ESACCI |
| 648 | ESA CCI | SMOS-IC | ESA CCI | ESACCI | ESACCI |
| 651 | SMAP L4 | SMAP L4 | SMAP L4 | SMAP L4 | SMAP L4 |
| 654 | SMAP L4 | SMAP L4 | CGLS | - | - |
| 661 | SMAP L4 | SMOS-IC | CGLS | SMAP L4 | SMAP L4 |
| 664 | ESA CCI | SMAP L4 | ESA CCI | ESACCI | ESA CCI |

| | | | | | |
|---|---|---|---|---|---|
| 674 | SMAP L4 | SMOS-IC | CGLS | SMAP L4 | SMAP L4 |
| 679 | SMAP L4 | SMAP L4 | SMAP L4 | SMAP L4 | SMAP L4 |
| 686 | SMAP L4 | ESA CCI | SMAP L4 / ESA CCI | SMAP L4 | SMAP L4 |
| 717 | SMAP L4 | SMAP L4 | ESA CCI | SMAP L4 | SMAP L4 |
| 735 | ASCAT | ASCAT | CGLS | - | - |
| 793 | ESA CCI | SMOS-IC | ESA CCI | ESACCI | ESA CCI |
| 795 | SMAP L4 | ESA CCI | ESA CCI | ESACCI | ESA CCI |
| 799 | SMAP L4 | SMAP L4 | ESA CCI | SMAP L4 | SMAP L4 |

In terms of ubRMSE, in line with the concept of complementarity, ESA CCI was superior to the SMAP L4. Consistent with Al-Yaari et al. (2019) who obtained lower performances of most remotely sensed SM products in "cold climate" areas (e.g., Koppen-Geiger D), we observed in Fig. 21 for ecoregion 679 an ubRMSE greater than 0.1 for all satellite products, as expected due to the effects of snow, frozen conditions and landscape. However, we should mention that the concurrence of disturbing factors, such as dense vegetation or mountains, could further alter the analysis performance in some of the ecoregions.

Concerning to the bias, SMAP L4 and ESA CCI tend to overestimate the in situ ISMN SM, SMOS-IC and CGLS is prone to underestimate in situ SM. It is worth noting that the use, in our study, of Gleeson's porosity map to rescaled CGLS and ASCAT measurement units for a consistent comparison with other satellite products, as highlighted by Fascetti et al. (2016), can influence the results.

What particularly stands out from the $r/r_{ANOM}$ comparison, as showed in Table 8, was the confirmation of the best results in addition to other performance metrics for all the remote sensing products in the case of the Baltic mixed forests (647) or Balkan mixed forests (646) but also Iberian sclerophyllous and semi-deciduous forests (793).

On the other hand, all SM satellite products showed the high signal variability due to the screening of anomaly outliers ($r_{ANOM}$ greater than r) in the central European mixed forest ecoregion (654). Moreover, SMAP L4, which has proved to be the

most accurate SM product in our analysis, showed a similar effect in performance also for the Pontic steppe (735) ecoregion, as well as it has been shown in the case of ESA CCI. This indicates that Central European mixed forest ecoregion (654) and Pontic steppe (735) ecoregions are critical areas to obtain accurate SM assessment via the selected satellite products.

Focusing on all results metrics of SMAP L4 (Fig.22), it achieved correlation around 0.7, the best values of ubRMSE and the highest performance in terms of $r/r_{ANOM}$ on the ecoregion group (cluster 1) constituted by 644, 646, 647 and 648. Similarly, the ecoregions of Mediterranean area (cluster 2: 793, 795 and 799) showed all a quite high performance with r around 0.66, ubRMSE around 0.07 and $r > r_{ANOM}$. Meanwhile, as said above, on the group (cluster 3) of 654 and 735, SMAP L4 reached low performances. Due to similar performances and as geographically contiguous areas, 679 and 717 could be considered as another group (cluster 4), shown in Fig. 22. In the rest part of ecoregions, it demonstrated also significative performances ($r> 0.5$ and $r > r_{ANOM}$) but without a particular common pattern (cluster 5).

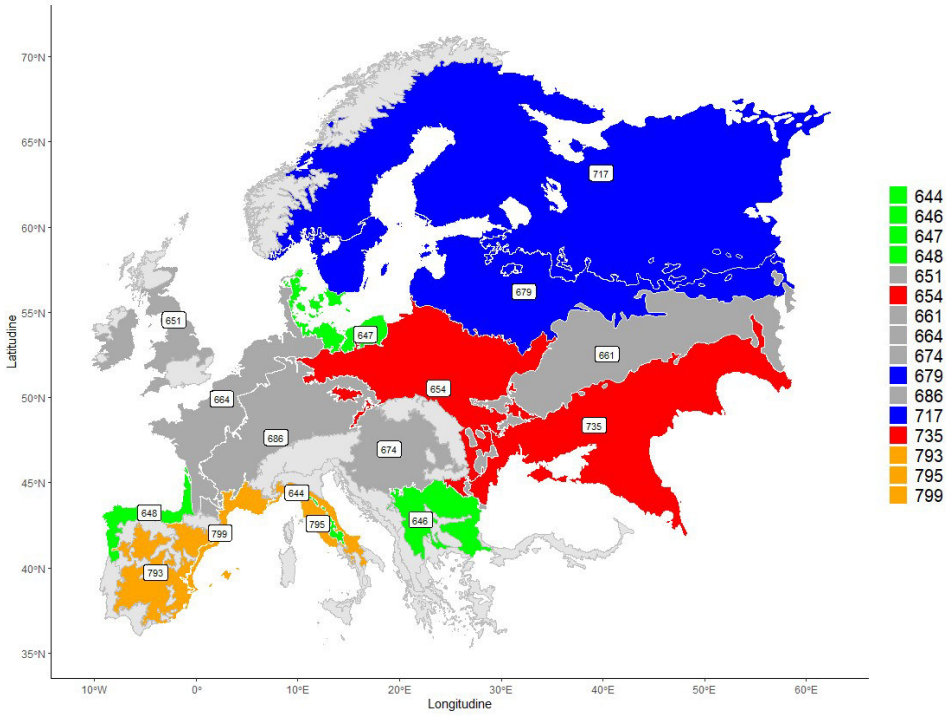


Fig. 22: Ecoregions grouped by clusters derived from performances (especially r using the top performer SMAP L4).

Hence, we used the ERA5-Land data, a reanalysis dataset providing at ~9km grid spacing and covering the period from 1950 to 2-3 months before the present, to find similarity inside each cluster or dissimilarity from one cluster to other that can support performances' results. The core of ERA5-Land, i.e., a reproduction of the land component of the ERA5 climate reanalysis, forced by the ERA5 weather fields, is the Tiled ECMWF Scheme for Surface Exchanges over Land that incorporates land surface hydrology (H-TESSEL). It uses the CY45R1 version of the IFS (https://confluence.ecmwf.int/display/CKB/ERA5-Land%3A+data+documentation). In particular, we have downloaded the data for each month of the period 2015-2020 for air temperature (2m_temperature: temperature of air at 2m above the surface of land, sea or in-land waters),

precipitation (total_precipitation: sum of large-scale precipitation and convective precipitation), evaporation (total_evaporation: accumulated amount of water that has evaporated from the Earth's surface) and Leaf Area Index of high and low vegetation (leaf_area_index_high_vegetation, leaf_area_index_low_vegetation). Thus, we have computed for each variable the annual mean, maximum and minimum.

The first cluster of ecoregions (644-646-647-648), where SMAP L4 showed the highest performance for most part of the metrics, was characterized by heavy rain, intermediate vegetation level and moderate evaporation (the air temperature did not give additional information). The ecoregions 793,795 and 799, were all in the Mediterranean and were characterized by low precipitation and evaporation and high temperature.

The remaining part of ecoregions presents a diversity of results in terms of metrics without a common pattern in the ERA5-Land data. An exception is the cluster 4 (679-717), in which only SMAP L4 obtained fair good results and the ERA5-Land indicates the coldest climates among all ecoregions (3-6 degrees average) and lowest evaporation. In addition, in those areas, there are few stations to characterize large areas where soils are cold and sparsely vegetated.

The Central European mixed forest (654) and Pontic steppe (735) ecoregions (cluster 3) were areas in which we cannot obtain accurate SM assessment via the selected satellite products, and apparently, they seem to do not have any common characteristics in terms of vegetation and climate. However, if we look at the comparison in terms of SM using SMAP L4 satellite product with both in situ and ERA5-Land SM (volumetric_soil_water_layer_1: volume of water in soil layer 1 for a depth that goes from 0 to 7cm), as showed in Fig. 23, we highlighted that SMAP L4 and ERA5-Land SM were good correlated in these ecoregions (graph in the middle). But similar to SMAP L4 vs ISMN correlation (on the left of Fig.

23), the ERA5-Land vs ISMN correlation (on the right of Fig. 23) was very low. This can suggest a possible inconsistency or a high uncertainty in the in-situ data. Moreover, there could be additional climatic and physical factors, e.g., subsurface scatterers, which may be the causes of uncorrelation. Wagner et al. (2022) recently demonstrated how in more temperate climatic regions, strong subsurface scatterers (e.g., karstic rock) may become detectable during dry spells, especially when they are near the soil surface, adding uncertainty in the retrieved SM value. Our results, indeed, indicate for sure problems in some areas that affected the continental scale analysis performed (please see last row of Table 9). In fact, the inclusion of these areas can affect the overall performance of SM products, hence producing the variegate results that several past studies have found in Europe.

It was nothing as for some of the ecoregions was more complicated to extract a clear picture of their behavior since an ecoregion is for its nature a combination of climate, soil, vegetation and results of remote sensing inter-comparison does not show a marked trend or a singular direction. However, this part of the work provides useful insights about SM products performance not achievable when regional, continental or global scale are considered and should support future studies in ranking various SM products for various application in different location of Europe.

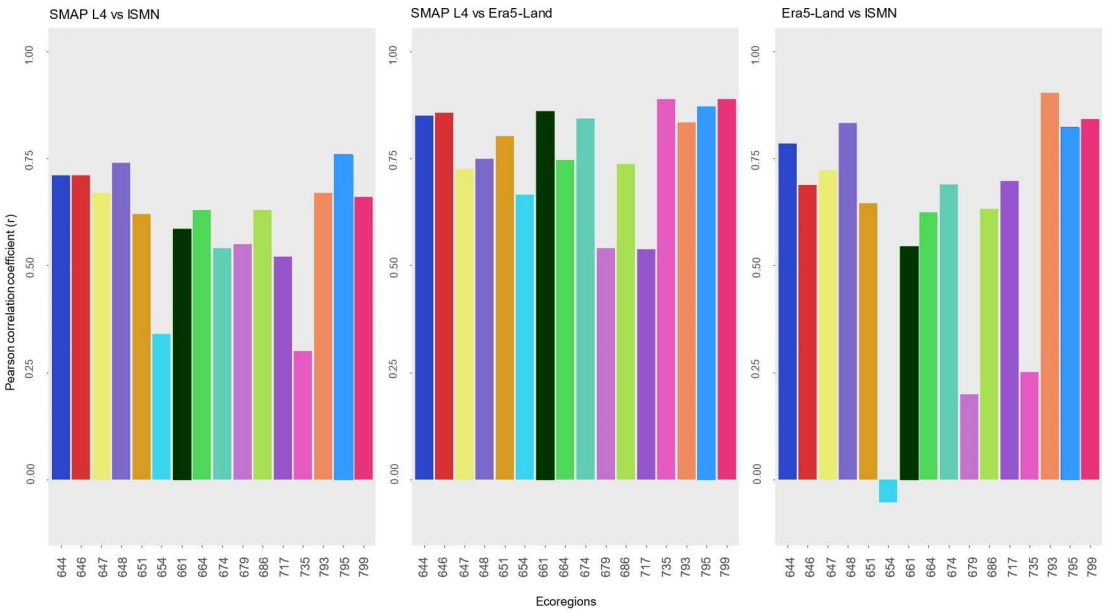


Fig. 23: Comparison of Pearson Correlation Coefficient across ecoregions on SM values between SMAP L4 and ISMN (on the left), SMAP L4 and ERA 5 LAND (in the middle), and ERA 5 LAND and ISMN (on the right).

## 4.2 The impact of seasonality

The results of the intercomparison have shown that there are some ecoregions which are undescribed regardless of satellite even if they shared the same ISMN network with other ecoregions which highlighted good performances. For these reasons, we focused on the effect of seasonality in the intercomparison on ecoregions covered by the RSMN network (Fig. 24).

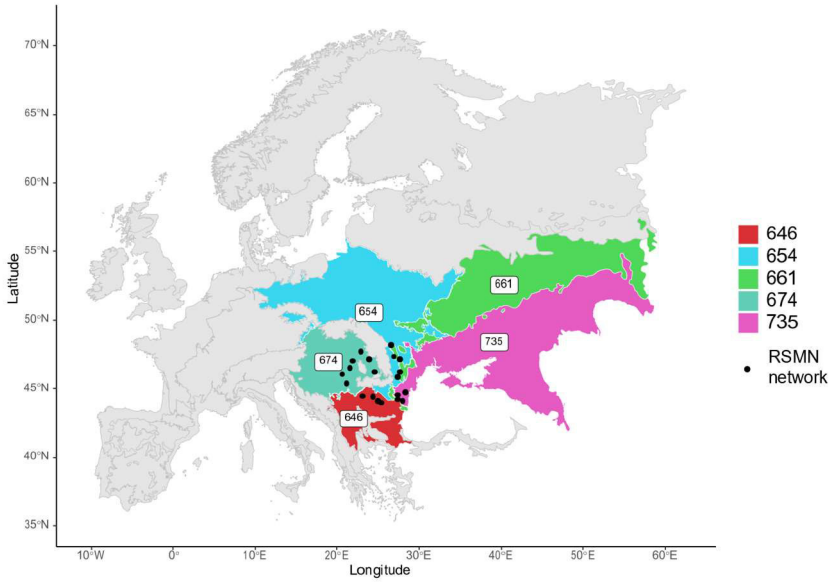


Fig. 24: Ecoregions analyzed in this part of the study and the Romanian Soil Moisture Network (RSMN).

As anticipated in Chapter 3, the seasonality was investigated following two parallel lines: first, completely removing the seasonality using the RST approach ($r_{ALICE}$); and then considering SM distribution and the phenological cycle.

Note that to provide an overview of the influence of short-term versus long-term variations, the first analysis we made was the comparison in terms of the Pearson Correlation Coefficient on raw data (r), on short-term SM anomalies as detected by using the 35-day moving window ($r_{ANOM}$), and by the RST approach ($r_{ALICE}$), as described in Section 3.4.1.

Once known the ability and inability of SM satellite retrievals in raw data, short- and long-term variation, we focused on the effect of seasonal variations on the dynamic behavior of the ASCAT SM retrievals.

### 4.2.1 The remotion of long-term variation in SM

Table 10 compares the performance of each considered product in terms of r between SM ISMN in-situ data and SM satellite data, SM anomalies ($r_{ANOM}$) evaluated on a moving window of 35 days, and the ALICE index ($r_{ALICE}$). The correlation already achieved considering the long-term series SM measurements (i.e., $r_{ANOM}$), after outlier removal, as done in the previous part of the work is presented. Those ecoregions where an increase in correlation was observed moving from the historical series analysis to the anomalies (both on the ALICE index and/or on the 35-day moving window) are highlighted in dark grey. As stated in Section 4.1, such an increase is unexpected, because seasonality increases the correlation, hence its occurrence should indicate a poor capability of the sensor and/or product to detect SM-related signals.

Our purpose was to verify if the SM satellite performance assessment changed when long-term variation was considered instead of short-term variation for the case study ecoregions. Overall, the results are in line with those reported in Section 4.1, since the SMAP L4 was the top performer, followed by the ESA CCI while the CGLS SSM was the worst.

In focusing on the long-term variation, we found that SMAP L4 and ESA CCI each obtained $r_{ALICE} \geq 0.5$ in two ecoregions and ASCAT and CGLS SSM in one. All four products had $r_{ALICE} \geq 0.5$ in the Balkan Mixed forests (646).

SMOS – IC was not able to describe any of the considered ecoregions (always $r_{ALICE} < 0.5$), maybe due to strong radio frequency interference (RFI) over Europe (de Nijs et al., 2015; Kerr et al., 2012; Naeimi et al., 2012; Parinussa et al., 2011). There were additional ecoregions in which one satellite reached a value of correlation greater than 0.5, (e.g., SMAP L4 for the Central European mixed forests (654), but these ecoregions were distinct since $r < r_{ALICE}$.

A correlation performance inversion (i.e., when r is lower than $r_{ALICE}$ or r is lower than $r_{ANOM}$), occurred in two regions with SMAP L4 and ESA CCI; and in three regions with ASCAT, CGLS and SMOS -IC. In all cases, these included the Central European mixed forests (654) and the Pontic steppe (735). Thus, $r_{ALICE}$ enhanced a particular behavior in ecoregions already underlined for the active sensors (ASCAT/CGLS).

Taking into account both $r \geq r_{ANOM}$ and $r \geq r_{ALICE}$, SMAP L4 and SMOS – IC similarly described short- and long-term variation by ecoregions. In fact, we see the inversion in both comparisons (r vs $r_{ANOM}$ and r vs $r_{ALICE}$) and for the same ecoregions. We expected the active SM products, i.e., ASCAT and CGLS would better describe the short-term variation in the Pontic steppe (735).

Interestingly, the Balkan Mixed forests (646) were well-described in both short and long-term variation ($r \geq r_{ALICE}$ and $r \geq r_{ANOM}$) regardless of SM satellite retrievals. In addition, it achieved $r_{ALICE} \geq 0.5$ for all products except SMOS – IC.

These results are in line with another study on the RSMN network (Ontel et al., 2021), which demonstrated that the correlation between C-band satellite products i.e., SWI (Https://land.copernicus.eu/global/products/swi) and the RSMN network, is high on the Getico Plateau, corresponding to ecoregion 646. Very low correlation values were observed close to the Romanian Plain and the Dobrogena Plateau, corresponding to the Pontic Steppe (735) and the Central European mixed forests (654). Generally, a good correlation was detected for those stations located on soils with a high percentage of sand and a low percentage of clay. Hydraulic phenomena due to soil texture, in addition to the possible presence of vegetation, may be the reason for this behavior. Soil texture influences the availability of soil particle surfaces for adsorption as well as the number of pores, and therefore, the availability of free water, the parameter which affects microwave emissivity. The ALICE index and the subsequent r computation among the ALICE index applied

to satellite SM retrievals and ground-based measurements allowed us to obtain a complete description of the intercomparison of SM products and confirmed the results reported in Section 4.1.

Table 10: Comparison between r, $r_{ANOM}$ and $r_{ALICE}$.

| | ASCAT | | | CGLS | | | ESA CCI | | | SMAPL4 | | | SMOS-IC | | |
|---|---|---|---|---|---|---|---|---|---|---|---|---|---|---|---|
| Ecoregions | r | $r_{ANOM}$ | $r_{ALICE}$ | r | $r_{ANOM}$ | $r_{ALICE}$ | r | $r_{ANOM}$ | $r_{ALICE}$ | r | $r_{ANOM}$ | $r_{ALICE}$ | r | $r_{ANOM}$ | $r_{ALICE}$ |
| 646 | 0.642 | 0.4058 | 0.505 | 0.5762 | 0.4163 | 0.5245 | 0.6577 | 0.4842 | 0.568429 | 0.7111 | 0.5466 | 0.5759 | 0.5868 | 0.3496 | 0.4401 |
| 654 | 0.1892 | 0.3586 | 0.3144 | 0.1636 | 0.2695 | 0.2602 | 0.0446 | 0.313 | 0.367018 | 0.343 | 0.5462 | 0.5004 | 0.1771 | 0.4713 | 0.3356 |
| 661 | 0.3988 | 0.4834 | 0.4226 | 0.2801 | 0.4592 | 0.4681 | 0.4806 | 0.4814 | 0.500792 | 0.5797 | 0.4899 | 0.4598 | 0.2726 | 0.3763 | 0.358 |
| 674 | 0.4576 | 0.4156 | 0.4087 | 0.4564 | 0.3988 | 0.4226 | 0.4903 | 0.4477 | 0.470375 | 0.5394 | 0.5056 | 0.4948 | 0.379 | 0.3113 | 0.3252 |
| 735 | 0.3551 | 0.2198 | 0.4157 | 0.3422 | 0.1061 | 0.4671 | 0.3467 | 0.4258 | 0.457066 | 0.3129 | 0.3863 | 0.4624 | 0.2611 | 0.3797 | 0.3786 |

### 4.2.2 Effect induced by the phenological cycle on SM dynamics

In the previous section, we analyzed the different behaviors of the considered SM products by removing the dependence on seasonality and considering SM anomalies. Overall, results corroborated that there could be particular hydraulic conditions or effects e.g., subsurface scatterers, in the Central European mixed forests (654) and Pontic steppe (735). This analysis relied exclusively on satellite data, was free from ground-based inaccuracy, and assisted in the discovery of new issues, i.e., ecoregions undescribed independently by satellite. To have a different look at the role of seasonality, we combined information from the analysis of SM distribution with information related to plant phenology.

As described in Section 3.4.2, the two main phenological phases, namely the growing and dormancy phases, were examined for each ecoregion using information provided by the European Environmental Agency (EEA).

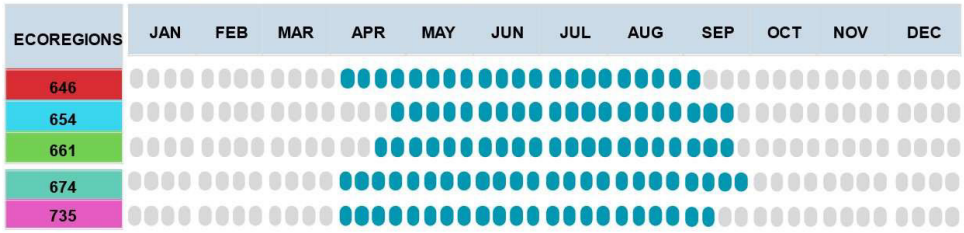


Fig. 25: Growth (blue) and dormancy (light gray) phases in each ecoregion.

Each phenological stage was identified for each RSMN station and then aggregated to calculate the median at the ecoregion scale during 2000-2016 (Fig. 25). From a phenological point of view, the dormancy phase, when water is not used by vegetation for growth, can be associated with a wet period, and the growing phase is therefore associated with a dry period. For each ground-based station, we first calculated the correlation between the SM measurements in the growth phase and

then in the dormancy phase. Box plots of the Pearson Correlation Coefficient (overall, growth and dormancy phases) computed among ASCAT timeseries and ISMN measurements by ecoregion are shown in Fig. 26.

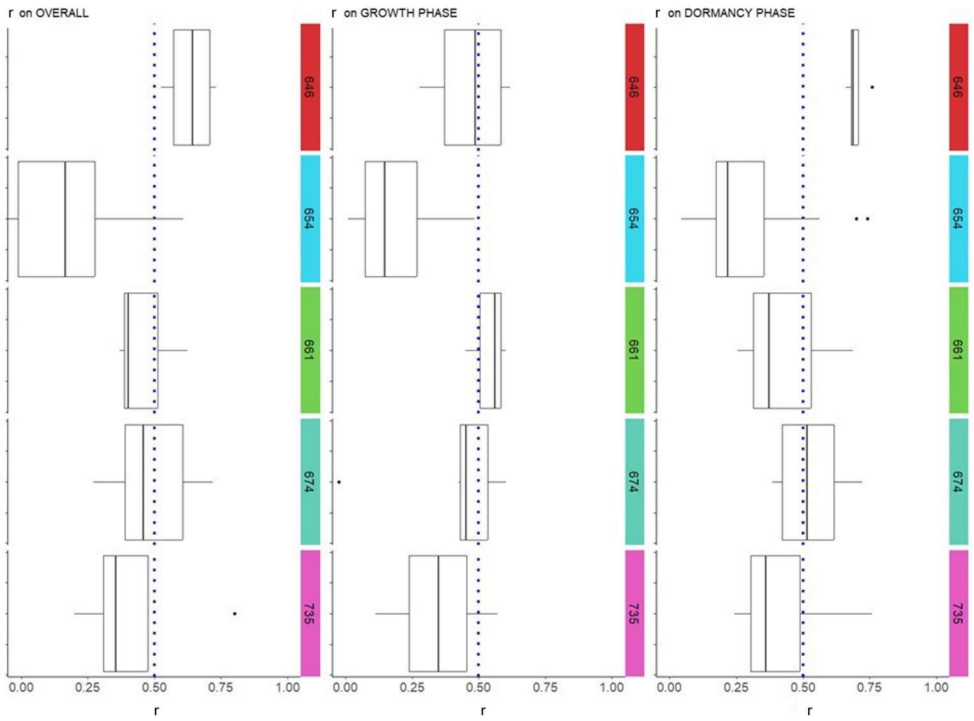


Fig. 26: Boxplot of Pearson Correlation Coefficient computed among ASCAT timeseries and ISMN measurements on Balkan mixed forests (646), Central European mixed Forests (654), East European forest steppe (661), Pannonian mixed forests (674) and finally on the Pontic steppe (735).

The correlation increased in the dormancy phase in the 646 and 674 ecoregions (Fig. 26). In the case of the Balkan Mixed Forests (646) there is a clear correlation increase (mean from 0.5 to 0.7) and a reduction in variability, with the first and third quartiles of the boxplot very close to the average values. This was well in agreement with the Balkan Mixed Forests (646) ecoregion description

(https://ecoregions.appspot.com/). The area is indeed characterized by a strongly seasonal climatological spatiotemporal variability, with northern areas experiencing high temperatures and rainfall in June, and the Thracian and Danubian Plains somewhat drier with slight peaks in rainfall in early summer and winter (https://www.oneearth.org/ecoregions/balkan-mixed-forests/). This result indicates a fairly clear relationship between phenology and soil moisture variability that we used in combination with information about the soil dynamics in terms of soil saturation, to better explain ecoregions behavior.

Focusing only on the ASCAT timeseries, we tried to find the behaviors based on SSM (dry/normal/wet) as described in Section 3.4.2.

Fig. 27 shows the SM distribution of ASCAT saturation data in the growth and dormancy stages and overall, for the considered ecoregions as well as examples of SM distributions taken from Manfreda et al. (2007). We emphasize our interest in the shape of the distribution; hence, in Fig. 27 we have employed a different maximum y-value depending on the distribution to avoid losing details of the shape. Analyzing the graphs on the left (i.e., those related to the overall and growth phase SM distributions), we see that the Balkan Mixed Forests (646), the East European forest steppe (661) and the Pannonian mixed forests (674) ecoregions seemed to show a Gaussian distributions. The Central European mixed forests (654) had two peaks in both graphs, while it is more difficult to classify the behavior of the Pontic steppe (735), as it shows an intermediate behavior with respect to the others. It could be an ecoregion borderline between dry and normal conditions. Moving to the analysis of the wet phase (i.e., the dormancy phase), the distributions show high frequency variability due to the greater presence of water (for all ecoregions). Generally, distributions have no predominant peaks in the 646, 661 and 674 ecoregions; while in the 735 ecoregion there is a peak before a saturation of 0.75. Ecoregion 654 shows the same behavior regardless of the phenological

stage, confirming the multimodality, with a clearer separation of the two peaks during dry, wet and normal conditions. Such a feature seems to be confirmed by comparing the graphs on the basis of phenology. The comparison of the growth and dormancy phases was in line for all ecoregions except for the Pontic steppe (735): a clear multimodality but with a large peak to lower values is present in the growth phase, while in the dormancy phase a large peak to highest values has been identified. This means that the overall distribution was multimodal.

One possible explanation for the multimodality (overall and growth phase) is that in dry conditions, the satellite products reflect the soil moisture of the root zone, a soil depth which is decoupled from the topsoil to which the ISMN measurements belong.

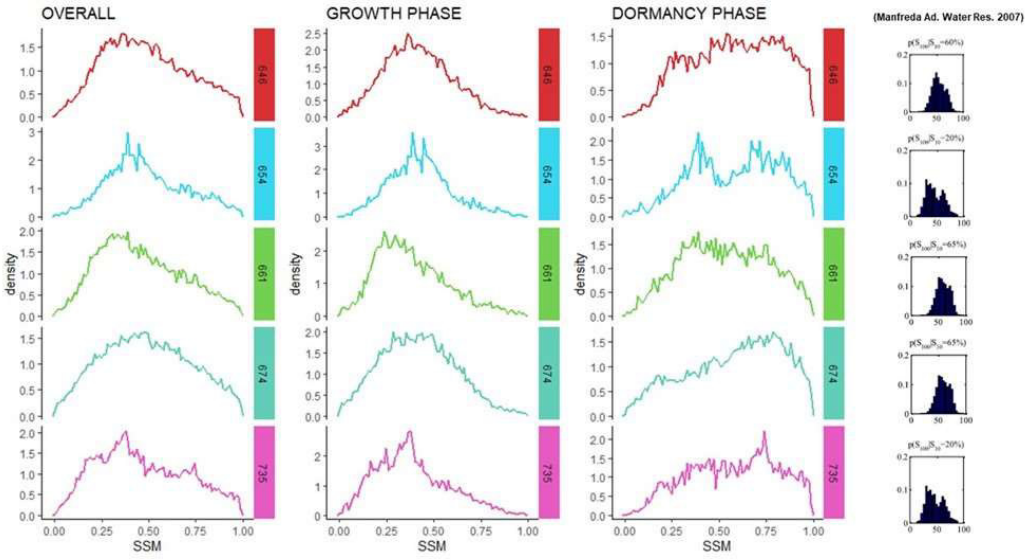


Fig. 27: Overall, dormancy phase and growth phase surface soil moisture (SSM) dynamics in Balkan mixed forests (646), Central European Mixed Forests (654), East European forest steppe (661), Pannonian mixed forests (674) and the Pontic steppe (735).

Table 11 shows the excess mass test results, useful to statistically verify multimodality (Ameijeiras-Alonso et al., 2019), computed considering the growth and dormancy phases and the whole period. According to the null hypothesis, if the p-value is less than 0.05, the distribution is multimodal; in addition, a smaller p-value ($p<<0.05$) brought greater results significance. In the dormancy phase, all ecoregions except 661 exhibited a p-value lower than 0.05, making it easier to find a multimodality pattern even if in some cases it was not too strong (e.g., in the case of the Pannonian mixed forests).

From the multimodality test, the Central European mixed Forests (654) had a strong multimodal distribution in both growth and dormancy phases (p-value < 2.20E-16), as did the Pontic steppe (735). On the other hand, we cannot reject the null hypothesis in the other ecoregions.

Table 11: Overall multimodality and multimodality test by stage of the five ecoregions.

| Ecoregions | Overall (p-value) | Growth (p-value) | Dormancy(p-value) |
|---|---|---|---|
| 646 | 0.244 | 0.068 | 2.20E-16 |
| 654 | 2.20E-16 | 2.20E-16 | 2.20E-16 |
| 661 | 0.074 | 0.008 | 0.096 |
| 674 | 0.032 | 0.002 | 0.014 |
| 735 | 2.20E-16 | 2.00E-03 | 2.20E-16 |

Taken together, these results suggest a relationship between the SM dynamic and the lack of correlation of SM satellite retrievals in certain ecoregions, i.e., the Central European mixed forests (654) and Pontic steppe (735).

Overall, these results suggest that merging SM dynamics with phenology, revealed that the challenging SM detection issues within the Central European mixed forest (654) and Pontic steppe (735) might stem not solely from ground-based

measurement station issues (difficulties in probe calibration and validation), as hypothesized in Section 4.1, but also from specific conditions giving rise to prolonged drought phases. Thus, the proposed approach seems to detect problems that could be in the SM microwave remote sensing retrievals at a landscape scale.

### 4.3 SCAT-SAR SWI SMAR results

As clarified in Chapter 3, the SWI approach, serving as an algorithm for merging ASCAT (H119-H120) with improved S-1 SSM, was chosen for its ease of application. The reliance on a single parameter i.e., the pseudodiffusivity T, although challenging to determine, is inversely proportional to the depth of the soil under consideration. consequently, the choice for SSM products can be simplified to T = 1 since the soil reference layer goes from 0 to a maximum 10 cm.

On the other hand, the SMAR approach, stemming from the same two-layer soil water balance but grounded in physical principles, enables the derivation of model parameters from soil properties. Therefore, the SWI-SMAR approach is expected to provide an accurate measure of Soil Moisture (SM) at the selected depths.

This section illustrates the results of the fusion of SCAT-SAR SWI data and the subsequent development of the RZ SCAT-SAR SWI SMAR product at a 30 cm scale, initially at a point scale and then at a regional scale.

#### 4.3.1 Point-scale

The outcomes presented in this section concern the two ground-based COSMOS stations in the ALENTO river basin. The overlap between the SM saturation histograms (%) obtained from the enhanced S-1 SSM product, ASCAT (H119-H120), and the ASCAT product modified to the initial dataset using CDF-matching through piecewise-linear matching (discussed in Sections 2.7.3.2 and 3.5.1) is shown in Fig. 28 (for COSMOS Alento station of Gorga on the left and

COSMOS Alento Monteforte on the right). The primary objective of this operation is to bring the two data distributions into convergence, ensuring they share the same cumulative distribution function or are at least aligned. When distributions are aligned, it indicates that they exhibit the same fundamental behavior and can be considered similar or equivalent. Thus, this correction, which reduces sensor-induced noise changes, is essential for the SCAT-SAR SWI product creation, shown in Fig. 29.

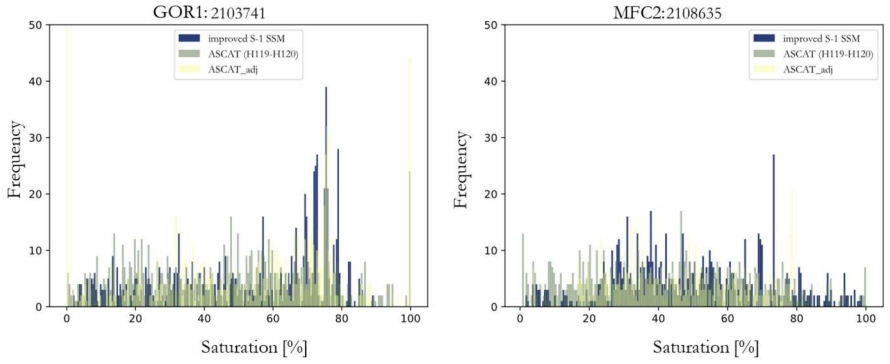


Fig. 28: Comparison between SSM distribution of the improved S-1 SSM, ASCAT (HH19-H120) and the ASCAT adjusted on the improved S-1 SSM for the two COSMOS stations in the Alento basin (Gorga on the left and Monteforte on the right).

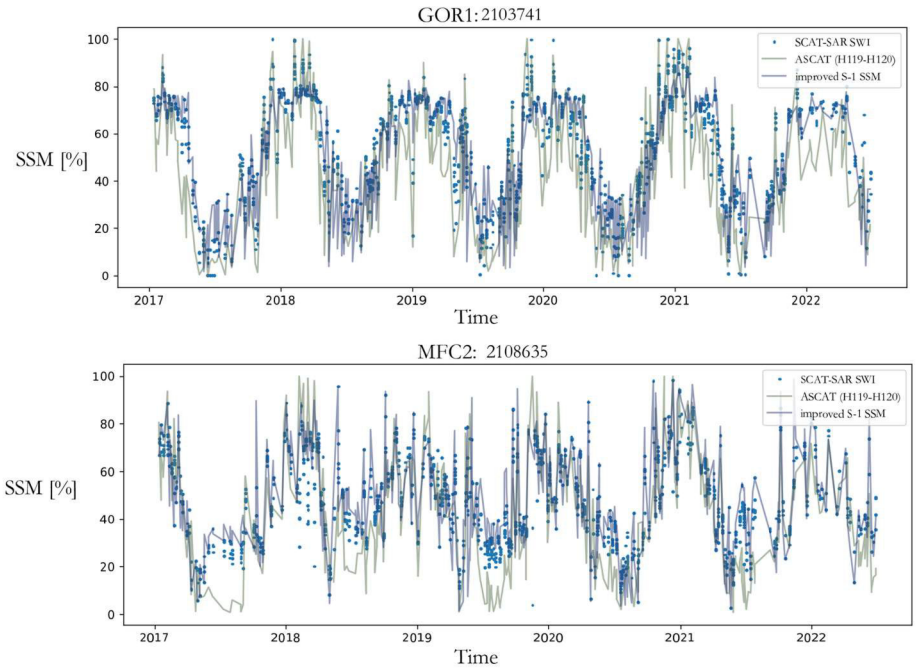


Fig. 29: Comparison between SSM timeseries of the improved S-1 SSM, ASCAT (HH19-H120) and the derived SCAT-SAR SWI for the two COSMOS stations in the Alento basin (Gorga on the top and Monteforte on the bottom).

Since both products (ASCAT and improved S-1 SSM) were given a weight of 1:1 throughout the development of the SWI fusion algorithm, it follows that the ASCAT product should be given more weight in the result due to its sub-daily resolution. However, the improved S-1 SSM achieved greater peaks of saturation in timeseries respect to ASCAT, while the SCAT-SAR SWI is generally in between the two, as can be observed from Fig. 29 (for instance, have a look at Monteforte's graph in the area between 2019 and 2020).

Once the daily 1 km SSM (SCAT-SAR SWI) was obtained using the measured parameters outlined in Table 3 of Chapter 3, the SMAR model was applied, resulting in the SCAT-SAR SWI SMAR product. Fig. 30 demonstrates the significant potential of this approach. The comparison between SCAT-SAR SWI and SCAT-SAR SMAR SWI revealed not only signal reduction but also

modification, with variations observed in the peaks. Moreover, SCAT-SAR SMAR SWI exhibited a plateau around 0.2, corresponding to the WP, due to the model's construction. The significance of incorporating physical parameters becomes further evident in Fig. 31, where the SCAT-SAR SWI SMAR was compared with the SCAT-SAR SWI SWI, i.e., the RZSM through the SWI model application, changing T. Specifically, results are depicted for T=10, T=15, and T=20.

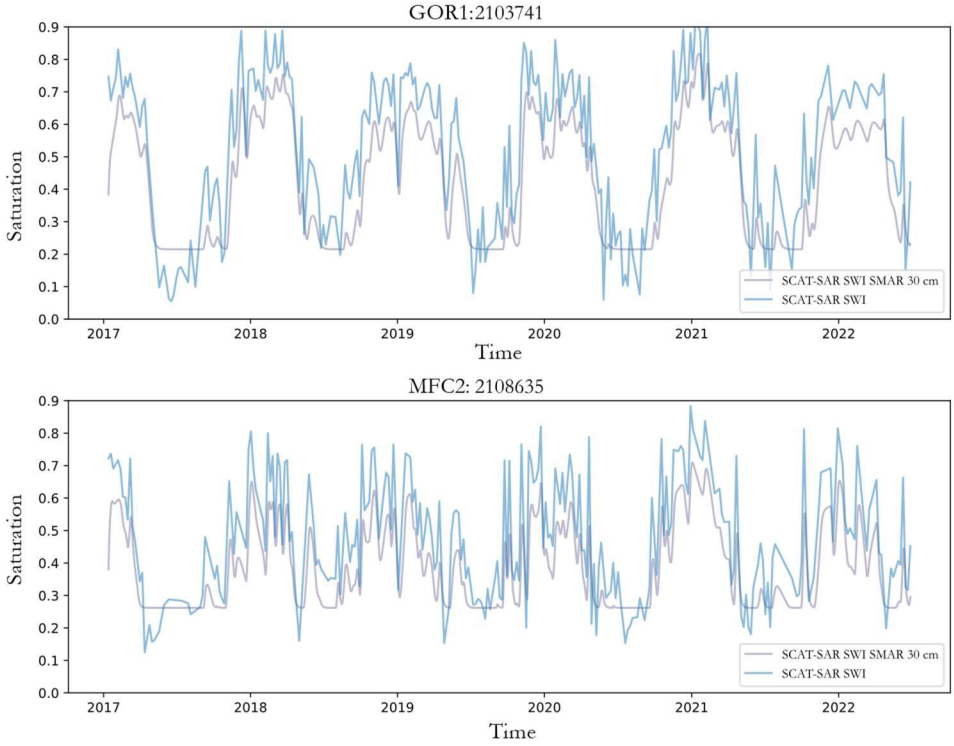


Fig. 30: Comparison between the SCAT-SAR SWI in terms of saturation and the SCAT-SAR SWI SMAR.

In the case of the SCAT-SAR SWI SWI, there are no significant changes observed during the transition from one time series to another, despite the variations in T

that account for different depths. The shape of the time series remains consistent, with peaks shifting directly in proportion to the increase in T.

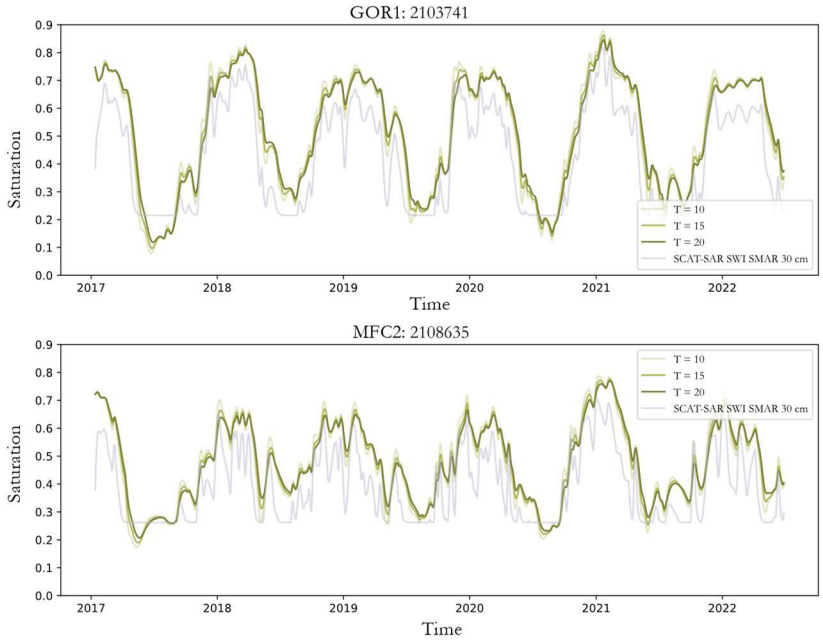


Fig. 31: RZSM information in terms of saturation: comparison between SCAT-SAR SWI SMAR at 30 cm and SCAT-SAR SWI SWI changing T (10,15,20).

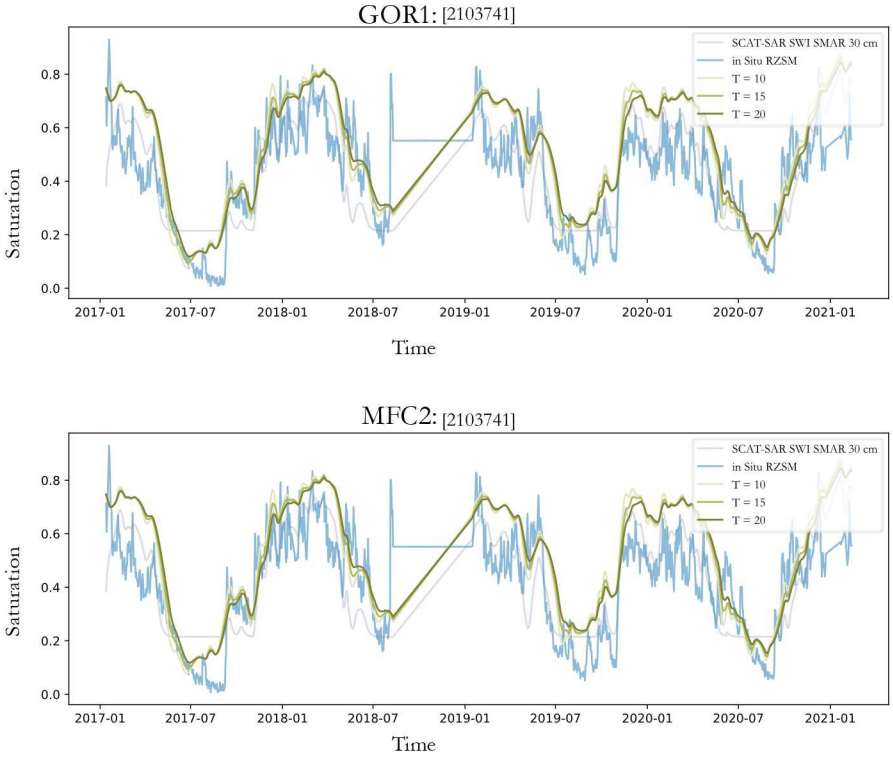


Fig. 32: Comparison between the available RZSM from the COSMOS stations and data reported in Fig.31 clipped on the in Situ availability. On the left of each graph are reported the performance in terms of correlation and RMSD.

Table 12: Performance in terms of R and RMSD between in situ RZSM and SMAR, SWI changing T (10;15;20).

| | GOR1 | | MFC2 | |
|---|---|---|---|---|
| RZSM method | r | RMSD | r | RMSD |
| SMAR | 0.81 | 0.012 | 0.82 | 0.03 |
| SWI (T=10) | 0.80 | 0.1 | 0.79 | 0.05 |
| SWI (T=15) | 0.80 | 0.1 | 0.78 | 0.05 |
| SWI (T=20) | 0.80 | 0.1 | 0.77 | 0.05 |

In Fig. 32 and Table 12, we show the comparison of Fig. 31 with the time series of in situ measurements. Note that we considered only the information available at the same time in order to calculate the r-correlation and RMSD. For both stations, the SCAT-SAR SWI SMAR had the lowest value of RMSD in comparison to the SCAT-SAR SWI SWI (T=10; 15; 20). On the other hand, considering r, both RZSM datasets exhibit a good correlation around 0.8.

These results demonstrated that the SCAT-SAR SWI SMAR is a good source of daily information at 1 km using measured parameters. In the following section, we have derived the physical parameters using a coarse-resolution dataset and tested the results at a regional scale.

### 4.3.2 Regional scale

We opted to broaden the scope of our inquiry after showcasing the point-scale method's capabilities because area information is essential for SM applications. Finding a method to determine the parameters (n, a, b, $s_w$, $s_c$) was the next challenge we faced. In this section, we will begin by presenting the SCAT-SAR SWI product obtained at the Basilicata scale. Subsequently, we will discuss the parameters employed in the derivation of the SCAT-SAR SWI SMAR product at a 30 cm resolution. Finally, we will perform a comparative analysis between SCAT-SAR SWI SMAR and SCAT-SAR SWI SWI concerning variations in T.

**SCAT-SAR SWI**

The use of the modified recursive exponential filter required the selection of a parameter T. It was set to 1, as it should describe the surface layer of the soil, given that the pseudo-diffusivity should be inversely proportional to depth; thus, lower T is more representative of the surface. In this way, a time series of SCAT-SAR SWI images for Basilicata was generated from 2017 to 2022. Since the input data

is in terms of saturation, the output is also expressed in terms of saturation, ranging from 0 to 1. Fig. 33 shows the maps for the same day for each of the analyzed years. The algorithm also internally utilizes masks from the S-1 SSM product to exclude results in cases where an area is masked due to reasons such as frozen terrain or others. The histograms in each figure allow for an examination of the distribution trend, which appears quite Gaussian for the days considered, consistent with theoretical soil moisture distributions. This implies a good fusion between the two input products.

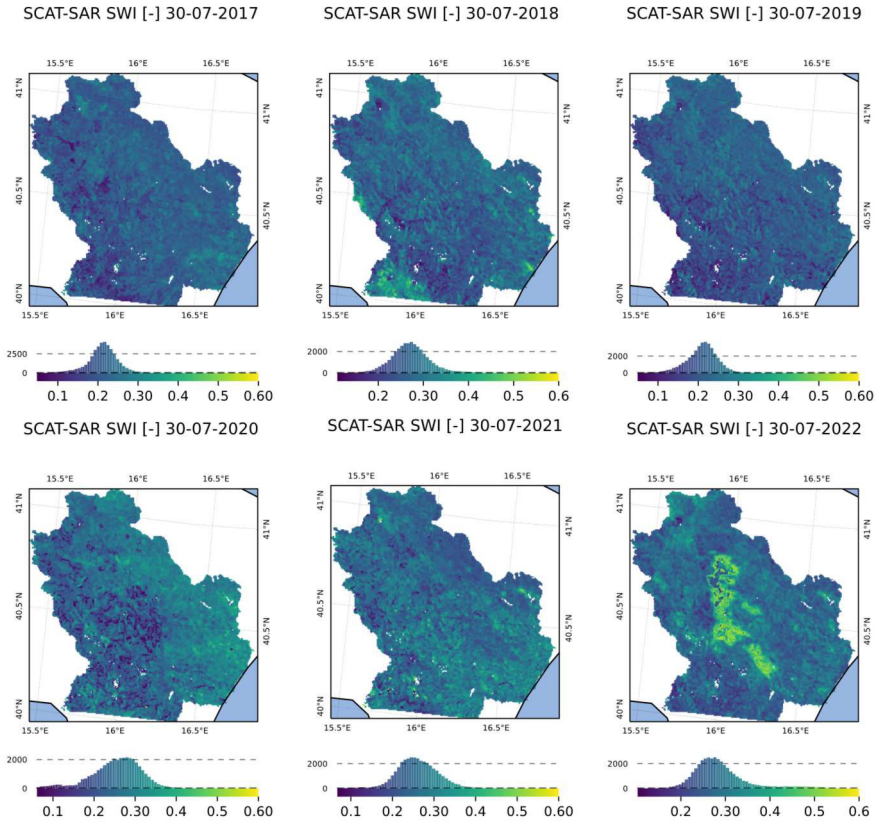


Fig. 33: SCAT-SAR SWI on Basilicata for July 30 (2017-2018-2019-2020- 2021-2022).

Despite the selection of a summer day (July 30), which typically experiences dry conditions (in fact, the saturation values are consistently maintained, peaking around 0.3 - 0.4), substantial year-to-year differences are evident, particularly in the western and south parts of the region.

Gained an overall perspective on Basilicata, we extracted the time series at one of the points within the domain of interest:

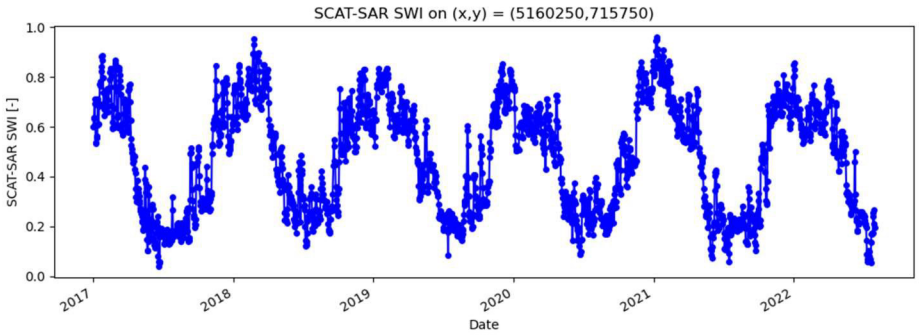


Fig. 34: SCAT-SAR SWI on the point (x,y) = (5160250,715750)

Note that the point locations are expressed in terms of Equi7grid coordinates (x, y), which correspond to (lon, lat) = (16.121, 40.039) in the south part of Basilicata. For more detailed information about the grid, please refer to Chapter 3. The time series appears promising, with acceptable saturation values and a discernible annual seasonality pattern.

We have used ERA5-Land 0 - 7 cm data as the ground truth for the SCAT-SAR SWI product. Fig. 35 shows the ERA5-Land 0 - 7 cm downscaled at 1 km for the same dates as Fig. 33.

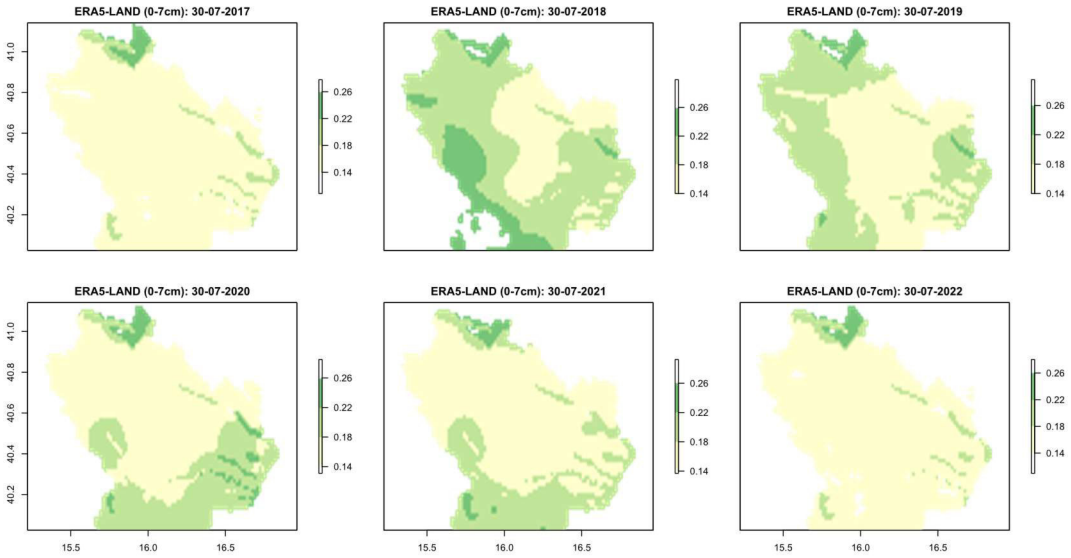


Fig. 35: ERA5-Land SSM downscaled at 1 km on Basilicata for July 30 (2017-2018-2019-2020-2021-2022).

In general, Fig. 35 seems to return a drier part corresponding to the eastern part of the region and a wetter part corresponding to the western part of the region.

Since ERA5-Land product is provided in terms of VWC, in order to compare it with the SCAT-SAR SWI product, we have transformed the ERA5-Land 0-7 cm surface product into saturation assuming that it represents the 95th percentile of measurements within a Gaussian distribution. Subsequently, the correlation is computed in Fig. 36:

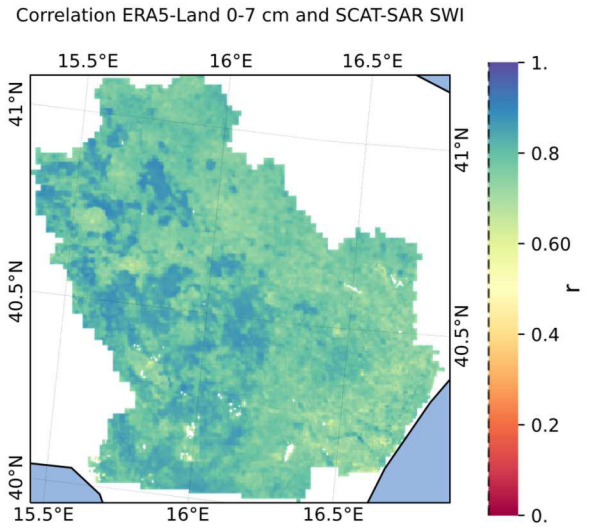


Fig. 36: Correlation between ERA5-Land 0-7 cm and SCAT-SAR SWI.

The mountainous region, corresponding to the western part of the area and also the wetter part, can be observed to exhibit a stronger correlation (Fig. 36). This is likely due to the more consistent precipitation patterns, as indicated by the following precipitation map (Fig. 37).

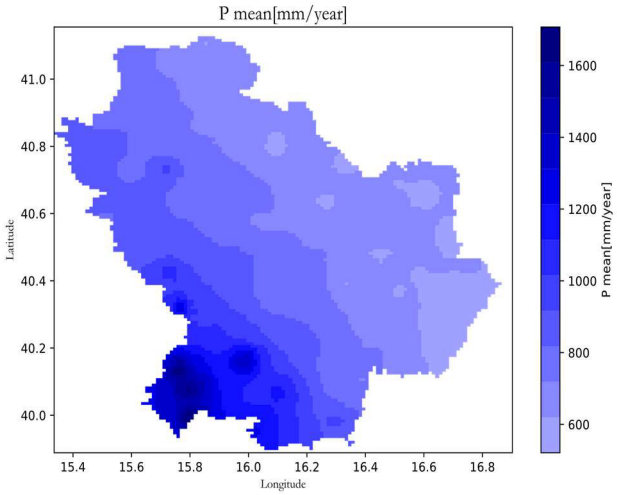


Fig. 37: Annual mean precipitation (2017-2022) on Basilicata from ERA5-Land dataset.

**SCAT-SAR SWI SMAR**

In order to utilize the SMAR approach to compute the RZSM from the SCAT-SAR SWI product, it was necessary to estimate the physical parameters of the model, according to its description (Section 3.5.2).

From Table 3 of Chapter 2, we have seen that the PTF proposed by to Rawls and Brakensiek, 1989 and Rawls et al., 1992 are associated with the FAO soil texture, some IDs. The world map of the soil texture at resolution of 0.1 degrees is available on the sites of NASA (https://ldas.gsfc.nasa.gov/gldas/soils). Thus, we have oversampling at a fine resolution (approximately 1 km), joined with the available particle size available online for the Basilicata region (http://dati.regione.basilicata.it/catalog/dataset/carta-granulometrica) subsequently using the Table 3 said before we have created new map of n, FC and WP. Combining this information with the mean monthly precipitation from ERA5-Land downscaled at 1 km we have obtained the parameter of losses "a".

Finally, from both layers' depth, n and WP parameters we derived the parameter "b". Fig. 38 shows these parameters for the whole Basilicata.

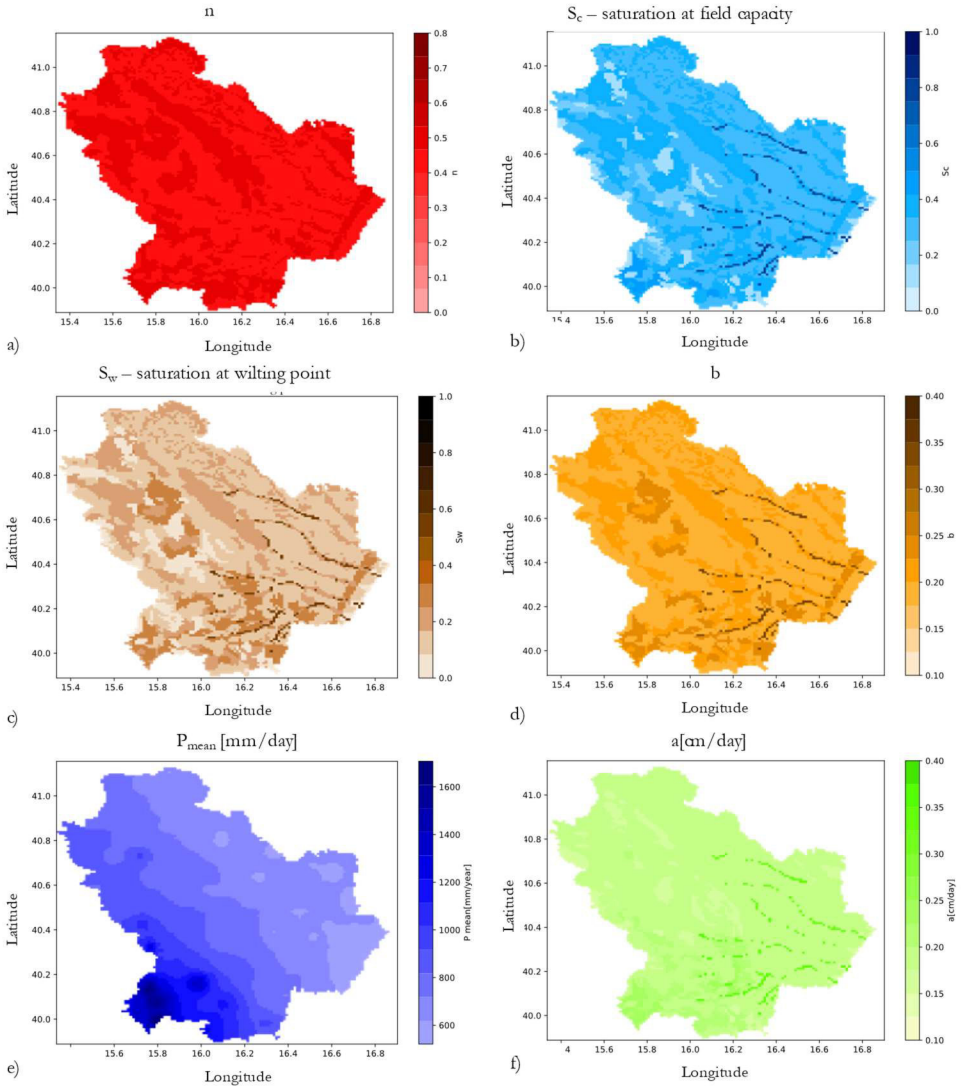


Fig. 38: Parameters required for the SMAR application: a) porosity; b) saturation at field capacity; c) saturation at wilting point; d) coefficient "b"; e) precipitation used to derive the losses coefficient "a"; f) coefficient "a".

Focusing on the parameters, they seem to have the same cluster of soil properties. In addition, deriving the coefficient "a" from precipitation and soil properties gave us the possibility to consider the link with soil depth. This could lead to the option of deriving different "a" and "b" based on the changes in depth. Parameters reported in Fig. 39 have been evaluated, referring to a top layer around 5 cm and a deeper layer of 30 cm, following the hypothesis of two soil layer's profiles.

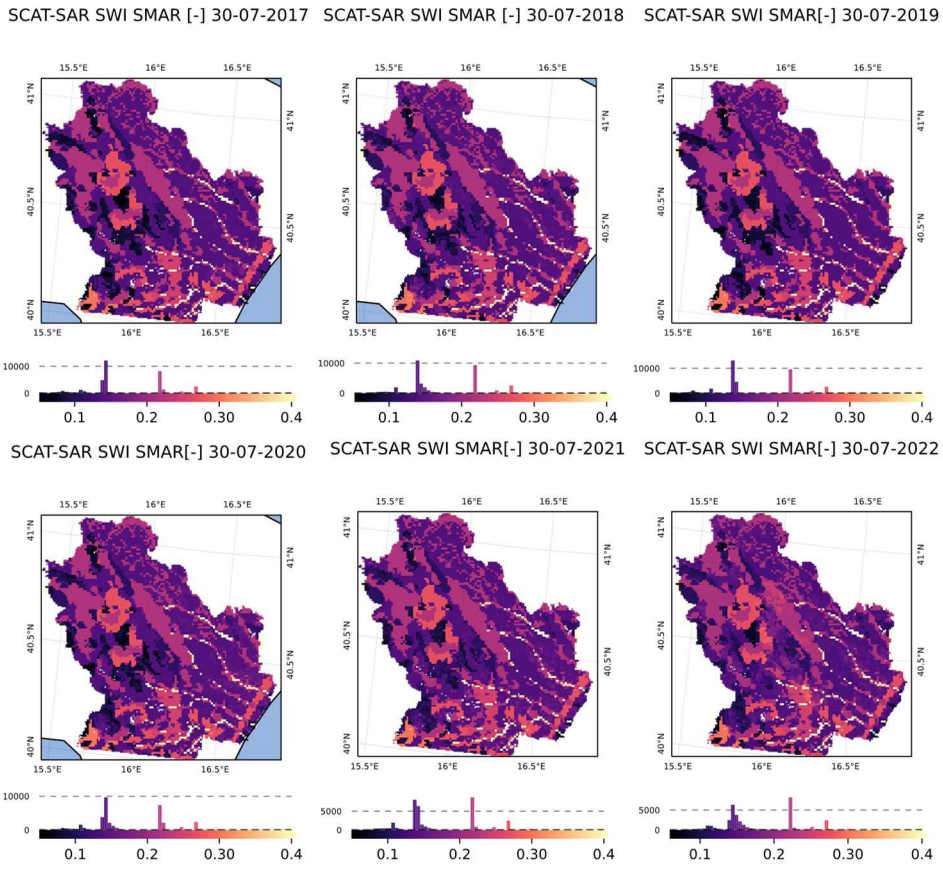


Fig. 39: SCAT-SAR SWI SMAR on Basilicata for July 30 (2017-2018-2019-2020- 2021-2022).

With the dry conditions of the selecting period, i.e., July 30 across 2017–2022, we saw that the SCAT-SAR SWI SMAR exhibited values of RZSM lower than the SCAT-SAR SWI (SSM), as expected; in addition, it lost the difference between the west and eastern part of the region, following the soil property clusters, as shown in Fig. 39. Comparing it with the ERA5-Land 7-28 cm dataset still yielded excellent correlation (Fig. 40), but the potential of this approach becomes evident primarily when compared with the RZ SCAT-SAR SWI SWI products. We report the correlation between ERA5-Land 7-28 cm and two SCAT-SAR SWI SWI products corresponding to T= (10; 15) in Fig. 40.

In terms of r, both the SCAT-SAR SWI SWI products exhibited a consistent trend. This implies that, like the at the Alento point scale, the use of SWI instead of SMAR to penetrate deeper into the soil profile led to an excessive adjustment, thereby flattening the surface SCAT-SAR SWI.

In addition, their comparison with the SCAT-SAR SWI product showed the same pattern with a sort of difference between the west and eastern parts of Basilicata. The use of physically based parameters in Fig. 38 resulted in the SCAT-SAR SWI SMAR product having a better correlation with the ERA5-Land 7-28 cm dataset, keeping the area of water bodies visible, which we have removed from the computation of correlation.

The proposed methodology has enabled the creation of a product sensitive to soil wetting and drying dynamics that can be used for monitoring soil water stress conditions. This provides a solid basis for the study of vulnerability to climate change in the areas examined. The relevance of the obtained SCAT-SAR SWI SMAR is evident in the context of the UNSDGs, since it proposes an innovative method that specifically contributes to action against climate change (SDG 13).

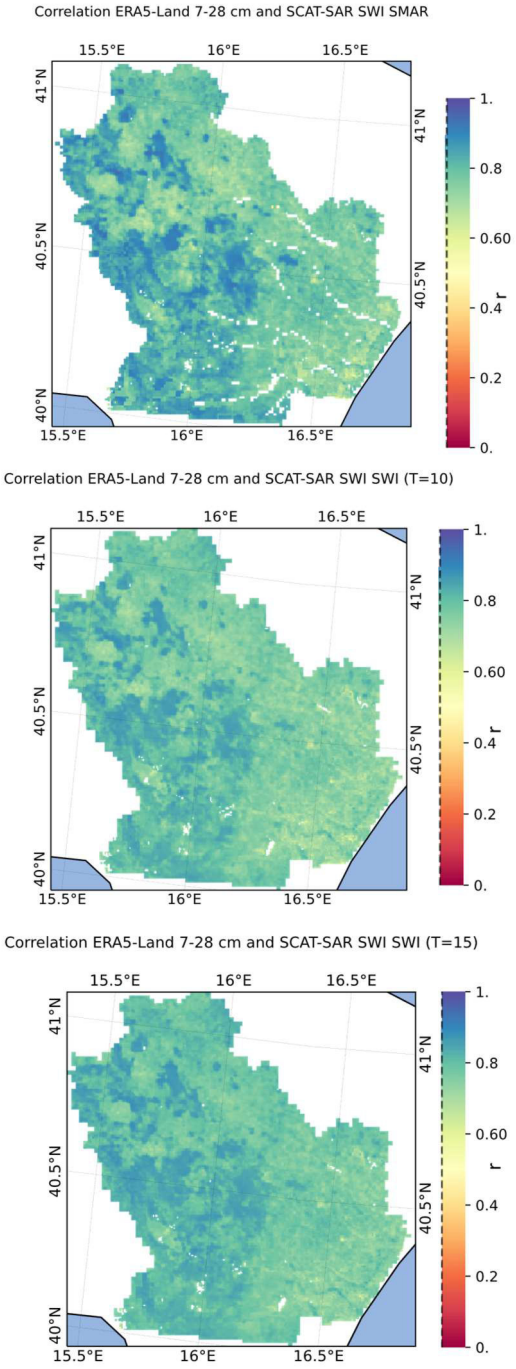


Fig. 40: Correlation between ERA5-Land 7-28 cm and RZ from SMAR, SWI T=10, SWI T= 15.

*Chapter 5*

# CONCLUSION

The identification of SM content and its variability is a crucial action to better analyze and monitor the effects induced by climate change. SM is an important parameter that can provide valuable insights, at different temporal scales, for example by helping in the identification of the status of flood-prone areas as well as assessing areas at risk of drought and/or landslides. This work addresses the issue of estimating relative SM conditions through integrated techniques involving microwave satellite measurements and hydrological modeling.

Its relevance is evident in the context of the UNSDGs, proposing an innovative method that specifically contributes to action against climate change (SDG 13). The advanced methodology enables the creation of an excellent product for monitoring soil water stress conditions, thus providing a solid foundation for studying the vulnerability to climate change in the examined areas. In fact, a detailed understanding of the pros and cons of remote sensing products paves the way for the subsequent development of studies aimed at improving crop resilience and adapting to extreme climatic events.

In the first part of the work, we made a comparison of microwave SM products of NASA and ESA that encompass passive SM retrievals like SMAP L4, SMOS-IC, as well as combined ESA CCI or active (ASCAT, CGLS SSM) in Europe.

ASCAT measurements (at 25 km resolution) have shown a good agreement when compared to ground measurements in European ecoregions, unlike the CGLS SSM measurements, which are less accurate due to being in an experimental phase.

Other microwave products such as SMAP L4 and ESA CCI have demonstrated higher reliability.

Satellite measurements are strongly influenced by the presence of vegetation and stable water bodies within their field of view, especially when using coarse spatial resolution products. Therefore, it is essential improve temporal and spatial resolution. Thus, for the second part of the work, only data processed from Synthetic Aperture Radar (SAR) instruments, such as ASCAT on board MetOp satellites, and SAR on board Sentinel-1 satellites, a constellation of two polar-orbiting satellites, has been used. The unique configuration of these active microwave satellites operating in the C-band, both able to provide SM information using the change detection method developed by TU Wien, has led us to choose ASCAT for its high temporal resolution, providing at least two daily measurements at the same location, and a derived product (SSM) from Sentinel-1 (SSM S-1), offering high spatial resolution with kilometer-scale measurements. The combination of the ASCAT revisit period and the spatial scale of SSM Sentinel-1 allows for monitoring environmental emergencies and supporting monitoring services.

Additionally, obtaining SM information at various depths can be challenging. These challenges were addressed and resolved by employing a Soil Water Index (SWI) fusion technique based on an exponential filter recursive formula, assigning weights to two 1:1 historical time series, and a SM Analytical Relationship (SMAR) hydrological modeling technique with empirically determined parameters.

The potential of this new approach for monitoring spatio-temporal variations in SM has been verified initially by comparing the results with the time series of the COSMOS Alento stations and subsequently in the Basilicata region from 2017 to 2022 through a comparison with the ERA5-Land dataset.

The study proceeded through several phases: the first phase that involved comparing freely available microwave SM products with ground measurements from the International SM Network on a European ecoregion scale has been developed at University of Basilicata. The second phase, conducted at the Department of Geodesy and Geoinformation (GEO) of Technische Universität Wien (TU Wien) in Vienna, focused on a deep analysis of ASCAT, the improved SSM S-1 product, and SWI as a fusion algorithm. The third phase has been the development of a SWI-SMAR framework with subsequent process and analysis thanks to skills acquired. Finally, the results were analyzed and interpreted.

Regarding the capability to identify specific SM conditions, the technique developed in this thesis has demonstrated the following characteristics:

- Scalability: The technique allowed for the estimation of SM values at intermediate depths (while current techniques provide values averaged over a meter), enabling a more realistic assessment of spatio-temporal SM conditions.

- Sensitivity: It could recognize daily variations in both the wetting and drying phases.

- Exportability: The approach can be immediately applied to other satellite sensors and in different geographical areas, as it relies entirely on available satellite data.

In particular, its application in Basilicata has proven its high reliability when compared to the ERA5-Land dataset (maximum $r \sim 0.7\text{-}0.8$), providing insights into SM status with a pattern similar to precipitation regimes. The western part of the region showed a better correlation, as it experiences more regular precipitation.

The proposed work serves as a preliminary study with the potential for interesting future developments in the Mediterranean area, one of the areas most affected by the effects of climate change. It is important to highlight that in the SCAT-SAR SWI, both ASCAT and improved S-1 SSM have been assigned equal weights (1:1). However, ASCAT carries greater significance due to its higher frequency of temporal measurements (ranging from 2 to 6 per day). This situation is further compounded by the current operational status of only one Sentinel-1 satellite (Sentinel-1 B has been out of service since December 23, 2021). Consequently, the launch of the Sentinel-1 C satellite, with an augmented number of high-temporal-resolution measurements, could represent a substantial improvement in the achieved results. In addition, a more precise derivation of SWI-SMAR model parameters would further refine its prediction. In a future perspective, the availability of soil macroporosity products with detailed studies of its alteration in response to climate change would meet the demand for more refined parameters. An example of this could be Hirmas et al., 2018, who demonstrated that continent-scale changes in soil hydraulic properties can give rise to unexplored feedback loops between climate and the Earth's surface, thereby intensifying the water cycle. The combination of more precise parameters with machine learning techniques could yield additional benefits.

# REFERENCE

Abbott, M.B., Refsgaard, J.C., 1996. Distributed hydrological modelling. Springer Science & Business Media.

Albano, R., Manfreda, S., Celano, G., 2017. MY SIRR: Minimalist agro-hYdrological model for Sustainable IRRigation management—Soil moisture and crop dynamics. SoftwareX 6, 107–117. https://doi.org/10.1016/j.softx.2017.04.005

Albergel, C., De Rosnay, P., Gruhier, C., Muñoz-Sabater, J., Hasenauer, S., Isaksen, L., Kerr, Y., Wagner, W., 2012. Evaluation of remotely sensed and modelled soil moisture products using global ground-based in situ observations. Remote Sensing of Environment 118, 215–226.

Albergel, C., Munier, S., Leroux, D.J., Dewaele, H., Fairbairn, D., Barbu, A.L., Gelati, E., Dorigo, W., Faroux, S., Meurey, C., Le Moigne, P., Decharme, B., Mahfouf, J.-F., Calvet, J.-C., 2017. Sequential assimilation of satellite-derived vegetation and soil moisture products using SURFEX_v8.0: LDAS-Monde assessment over the Euro-Mediterranean area. Geosci. Model Dev. 10, 3889–3912. https://doi.org/10.5194/gmd-10-3889-2017

Albergel, C., Rüdiger, C., Pellarin, T., Calvet, J.-C., Fritz, N., Froissard, F., Suquia, D., Petitpa, A., Piguet, B., Martin, E., 2008. From near-surface to root-zone soil moisture using an exponential filter: an assessment of the method based on in-situ observations and model simulations. Hydrology and Earth System Sciences 12, 1323–1337.

Al-Yaari, A., Wigneron, J.-P., Dorigo, W., Colliander, A., Pellarin, T., Hahn, S., Mialon, A., Richaume, P., Fernandez-Moran, R., Fan, L., Kerr, Y.H., De Lannoy, G., 2019. Assessment and inter-comparison of recently developed/reprocessed microwave satellite soil moisture products using ISMN ground-based measurements. Remote Sensing of Environment 224, 289–303. https://doi.org/10.1016/j.rse.2019.02.008

Al-Yaari, A., Wigneron, J.-P., Ducharne, A., Kerr, Y., De Rosnay, P., De Jeu, R., Govind, A., Al Bitar, A., Albergel, C., Munoz-Sabater, J., others, 2014. Global-scale evaluation of two satellite-based passive microwave soil moisture datasets (SMOS and AMSR-E) with respect to Land Data Assimilation System estimates. Remote Sensing of Environment 149, 181–195.

Ameijeiras-Alonso, J., Crujeiras, R.M., Rodríguez-Casal, A., 2019. Mode testing, critical bandwidth and excess mass. Test 28, 900–919.

Baldwin, D., Manfreda, S., Keller, K., Smithwick, E.A.H., 2017. Predicting root zone soil moisture with soil properties and satellite near-surface moisture data across the conterminous United States. Journal of Hydrology 546, 393–404. https://doi.org/10.1016/j.jhydrol.2017.01.020

Baldwin, D., Manfreda, S., Lin, H., Smithwick, E.A.H., 2019. Estimating Root Zone Soil Moisture Across the Eastern United States with Passive Microwave Satellite Data and a Simple Hydrologic Model. Remote Sensing 11, 2013. https://doi.org/10.3390/rs11172013

Bauer-Marschallinger, B., Freeman, V., Cao, S., Paulik, C., Schaufler, S., Stachl, T., Modanesi, S., Massari, C., Ciabatta, L., Brocca, L., Wagner, W., 2019. Toward Global Soil Moisture Monitoring With Sentinel-1: Harnessing Assets and Overcoming Obstacles. IEEE Trans. Geosci. Remote Sensing 57, 520–539. https://doi.org/10.1109/TGRS.2018.2858004

Bauer-Marschallinger, B., Paulik, C., Hochstöger, S., Mistelbauer, T., Modanesi, S., Ciabatta, L., Massari, C., Brocca, L., Wagner, W., 2018. Soil Moisture from Fusion of Scatterometer and SAR: Closing the Scale Gap with Temporal Filtering. Remote Sensing 10, 1030. https://doi.org/10.3390/rs10071030

Bauer-Marschallinger, B., Sabel, D., Wagner, W., 2014. Optimisation of global grids for high-resolution remote sensing data. Computers & Geosciences 72, 84–93. https://doi.org/10.1016/j.cageo.2014.07.005

Bircher, S., Skou, N., Jensen, K.H., Walker, J.P., Rasmussen, L., 2012. A soil moisture and temperature network for SMOS validation in Western Denmark. Hydrology and Earth System Sciences 16, 1445–1463.

Blunden, J., Boyer, T., 2022. A Look at 2021: Takeaway Points from the State of the Climate Supplement. Bulletin of the American Meteorological Society 103, 684–691. https://doi.org/10.1175/BAMS-D-22-0177.1

Blunden, Jessica, Boyer, T., 2022. State of the climate in 2021. Bulletin of the American Meteorological Society 103, S1–S465.

Bogena, H., Schron, M., Jakobi, J., Ney, P., Rosolem, R., Zacharias, S., Vereecken, H.,

2021. Challenges and opportunities of COSMOS networks for continental scale moisture and drought monitoring, in: AGU Fall Meeting Abstracts. pp. H53B-01.

Bojinski, S., Verstraete, M., Peterson, T.C., Richter, C., Simmons, A., Zemp, M., 2014. The concept of essential climate variables in support of climate research, applications, and policy. Bulletin of the American Meteorological Society 95, 1431–1443.

Bouma, J., 1989. Using soil survey data for quantitative land evaluation. Advances in Soil Science: Volume 9 177–213.

Boussetta, S., Balsamo, G., Arduini, G., Dutra, E., McNorton, J., Choulga, M., Agustí-Panareda, A., Beljaars, A., Wedi, N., Munõz-Sabater, J., De Rosnay, P., Sandu, I., Hadade, I., Carver, G., Mazzetti, C., Prudhomme, C., Yamazaki, D., Zsoter, E., 2021. ECLand: The ECMWF Land Surface Modelling System. Atmosphere 12, 723. https://doi.org/10.3390/atmos12060723

Bowling, L., Pomeroy, J., Lettenmaier, D., 2004. Parameterization of blowing-snow sublimation in a macroscale hydrology model. Journal of Hydrometeorology 5, 745–762.

Bowling, L.C., Lettenmaier, D.P., 2010. Modeling the Effects of Lakes and Wetlands on the Water Balance of Arctic Environments. Journal of Hydrometeorology 11, 276–295. https://doi.org/10.1175/2009JHM1084.1

Brakensiek, D., Rawls, W., Stephenson, G., 1984. Modifying SCS hydrologic soil groups and curve numbers for rangeland soils. ASAE Paper (PNR-84203).

Brocca, L., Hasenauer, S., Lacava, T., Melone, F., Moramarco, T., Wagner, W., Dorigo, W., Matgen, P., Martínez-Fernández, J., Llorens, P., others, 2011. Soil moisture estimation through ASCAT and AMSR-E sensors: An intercomparison and validation study across Europe. Remote Sensing of Environment 115, 3390–3408.

Brocca, L., Melone, F., Moramarco, T., Morbidelli, R., 2009. Soil moisture temporal stability over experimental areas in Central Italy. Geoderma 148, 364–374. https://doi.org/10.1016/j.geoderma.2008.11.004

Brooks, R.H., Corey, A.T., 1966. Properties of porous media affecting fluid flow. Journal of the irrigation and drainage division 92, 61–88.

Brown, J.D., Heuvelink, G.B., 2006. Assessing uncertainty propagation through physically based models of soil water flow and solute transport. Encyclopedia of hydrological sciences.

Budyko, M.I., 1974. Climate and life. (No Title).

Budyko, M.I., 1956. The heat balance of the earth's surface. (No Title).

Bulgarini, F., Teofili, C., Bologna, G., 2004. Global 200 ERC, Ecoregional Conservation. Il processo di conservazione.

Chakravorty, A., Chahar, B.R., Sharma, O.P., Dhanya, C.T., 2016. A regional scale performance evaluation of SMOS and ESA-CCI soil moisture products over India with simulated soil moisture from MERRA-Land. Remote Sensing of Environment 186, 514–527. https://doi.org/10.1016/j.rse.2016.09.011

Champion, I., 1996. Simple modelling of radar backscattering coefficient over a bare soil: variation with incidence angle, frequency and polarization. International Journal of Remote Sensing 17, 783–800.

Chen, F., Crow, W.T., Colliander, A., Cosh, M.H., Jackson, T.J., Bindlish, R., Reichle, R.H., Chan, S.K., Bosch, D.D., Starks, P.J., Goodrich, D.C., Seyfried, M.S., 2017. Application of Triple Collocation in Ground-Based Validation of Soil Moisture Active/Passive (SMAP) Level 2 Data Products. IEEE J. Sel. Top. Appl. Earth Observations Remote Sensing 10, 489–502. https://doi.org/10.1109/JSTARS.2016.2569998

Chen, F., Mitchell, K., Schaake, J., Xue, Y., Pan, H.-L., Koren, V., Duan, Q.Y., Ek, M., Betts, A., 1996. Modeling of land surface evaporation by four schemes and comparison with FIFE observations. Journal of Geophysical Research: Atmospheres 101, 7251–7268.

Chen, J.M., Chen, X., Ju, W., Geng, X., 2005. Distributed hydrological model for mapping evapotranspiration using remote sensing inputs. Journal of Hydrology 305, 15–39.

Cherkauer, K.A., Bowling, L.C., Lettenmaier, D.P., 2003. Variable infiltration capacity cold land process model updates. Global and Planetary Change 38, 151–159.

Clapp, R.B., Hornberger, G.M., 1978. Empirical equations for some soil hydraulic properties. Water resources research 14, 601–604.

Colliander, A., Jackson, T.J., Bindlish, R., Chan, S., Das, N., Kim, S.B., Cosh, M.H., Dunbar, R.S., Dang, L., Pashaian, L., Asanuma, J., Aida, K., Berg,

A., Rowlandson, T., Bosch, D., Caldwell, T., Caylor, K., Goodrich, D., al Jassar, H., Lopez-Baeza, E., Martínez-Fernández, J., González-Zamora, A., Livingston, S., McNairn, H., Pacheco, A., Moghaddam, M., Montzka, C., Notarnicola, C., Niedrist, G., Pellarin, T., Prueger, J., Pulliainen, J., Rautiainen, K., Ramos, J., Seyfried, M., Starks, P., Su, Z., Zeng, Y., van der Velde, R., Thibeault, M., Dorigo, W., Vreugdenhil, M., Walker, J.P., Wu, X., Monerris, A., O'Neill, P.E., Entekhabi, D., Njoku, E.G., Yueh, S., 2017. Validation of SMAP surface soil moisture products with core validation sites. Remote Sensing of Environment 191, 215–231. https://doi.org/10.1016/j.rse.2017.01.021

Copernicus Climate Change Service, 2019a. ERA5-Land monthly averaged data from 2001 to present. https://doi.org/10.24381/CDS.68D2BB30

Copernicus Climate Change Service, 2019b. ERA5-Land hourly data from 2001 to present. https://doi.org/10.24381/CDS.E2161BAC

Cosby, B., Hornberger, G., Clapp, R., Ginn, T., 1984. A statistical exploration of the relationships of soil moisture characteristics to the physical properties of soils. Water resources research 20, 682–690.

Cosh, M.H., Jackson, T.J., Starks, P., Heathman, G., 2006. Temporal stability of surface soil moisture in the Little Washita River watershed and its applications in satellite soil moisture product validation. Journal of Hydrology 323, 168–177. https://doi.org/10.1016/j.jhydrol.2005.08.020

Cramer, W., Guiot, J., Fader, M., Garrabou, J., Gattuso, J.-P., Iglesias, A., Lange, M.A., Lionello, P., Llasat, M.C., Paz, S., Peñuelas, J., Snoussi, M., Toreti, A., Tsimplis, M.N., Xoplaki, E., 2018. Climate change and interconnected risks to sustainable development in the Mediterranean. Nature Clim Change 8, 972–980. https://doi.org/10.1038/s41558-018-0299-2

Cui, C., Xu, J., Zeng, J., Chen, K.-S., Bai, X., Lu, H., Chen, Q., Zhao, T., 2017. Soil moisture mapping from satellites: An intercomparison of SMAP, SMOS, FY3B, AMSR2, and ESA CCI over two dense network regions at different spatial scales. Remote Sensing 10, 33.

Dai, Y., Shangguan, W., Duan, Q., Liu, B., Fu, S., Niu, G., 2013. Development of a China dataset of soil hydraulic parameters using pedotransfer

functions for land surface modeling. Journal of Hydrometeorology 14, 869–887.

de Nijs, A.H., Parinussa, R.M., de Jeu, R.A., Schellekens, J., Holmes, T.R., 2015. A methodology to determine radio-frequency interference in AMSR2 observations. IEEE Transactions on Geoscience and Remote Sensing 53, 5148–5159.

De Troch, F., Troch, P., Su, Z., Lin, D., 1996. Application of remote sensing for hydrological modelling. Distributed hydrological modelling 165–191.

Derksen, C., Xu, X., Scott Dunbar, R., Colliander, A., Kim, Y., Kimball, J.S., Black, T.A., Euskirchen, E., Langlois, A., Loranty, M.M., Marsh, P., Rautiainen, K., Roy, A., Royer, A., Stephens, J., 2017. Retrieving landscape freeze/thaw state from Soil Moisture Active Passive (SMAP) radar and radiometer measurements. Remote Sensing of Environment 194, 48–62. https://doi.org/10.1016/j.rse.2017.03.007

Di Polito, C., Ciancia, E., Coviello, I., Doxaran, D., Lacava, T., Pergola, N., Satriano, V., Tramutoli, V., 2016. On the Potential of Robust Satellite Techniques Approach for SPM Monitoring in Coastal Waters: Implementation and Application over the Basilicata Ionian Coastal Waters Using MODIS-Aqua. Remote Sensing 8, 922. https://doi.org/10.3390/rs8110922

Dinerstein, E., Olson, D., Joshi, A., Vynne, C., Burgess, N.D., Wikramanayake, E., Hahn, N., Palminteri, S., Hedao, P., Noss, R., others, 2017. An ecoregion-based approach to protecting half the terrestrial realm. BioScience 67, 534–545.

Dorigo, W., De Jeu, R., Chung, D., Parinussa, R., Liu, Y., Wagner, W., Fernández-Prieto, D., 2012. Evaluating global trends (1988–2010) in harmonized multi-satellite surface soil moisture. Geophysical Research Letters 39.

Dorigo, W., Himmelbauer, I., Aberer, D., Schremmer, L., Petrakovic, I., Zappa, L., Preimesberger, W., Xaver, A., Annor, F., Ardö, J., Baldocchi, D., Bitelli, M., Blöschl, G., Bogena, H., Brocca, L., Calvet, J.-C., Camarero, J.J., Capello, G., Choi, M., Cosh, M.C., van de Giesen, N., Hajdu, I., Ikonen, J., Jensen, K.H., Kanniah, K.D., de Kat, I., Kirchengast, G., Kumar Rai, P., Kyrouac, J., Larson, K., Liu, S., Loew, A., Moghaddam, M., Martínez Fernández, J., Mattar Bader,

C., Morbidelli, R., Musial, J.P., Osenga, E., Palecki, M.A., Pellarin, T., Petropoulos, G.P., Pfeil, I., Powers, J., Robock, A., Rüdiger, C., Rummel, U., Strobel, M., Su, Z., Sullivan, R., Tagesson, T., Varlagin, A., Vreugdenhil, M., Walker, J., Wen, J., Wenger, F., Wigneron, J.P., Woods, M., Yang, K., Zeng, Y., Zhang, X., Zreda, M., Dietrich, S., Gruber, A., van Oevelen, P., Wagner, W., Scipal, K., Drusch, M., Sabia, R., 2021. The International Soil Moisture Network: serving Earth system science for over a decade. Hydrol. Earth Syst. Sci. 25, 5749–5804. https://doi.org/10.5194/hess-25-5749-2021

Dorigo, W., Oevelen, P., Wagner, W., Drusch, M., Mecklenburg, S., Robock, A., Jackson, T., 2011. A New International Network for in Situ Soil Moisture Data. Eos Trans. AGU 92, 141–142. https://doi.org/10.1029/2011EO170001

Dorigo, W., Wagner, W., Albergel, C., Albrecht, F., Balsamo, G., Brocca, L., Chung, D., Ertl, M., Forkel, M., Gruber, A., Haas, E., Hamer, P.D., Hirschi, M., Ikonen, J., de Jeu, R., Kidd, R., Lahoz, W., Liu, Y.Y., Miralles, D., Mistelbauer, T., Nicolai-Shaw, N., Parinussa, R., Pratola, C., Reimer, C., van der Schalie, R., Seneviratne, S.I., Smolander, T., Lecomte, P., 2017. ESA CCI Soil Moisture for improved Earth system understanding: State-of-the art and future directions. Remote Sensing of Environment 203, 185–215. https://doi.org/10.1016/j.rse.2017.07.001

Dorigo, W.A., Xaver, A., Vreugdenhil, M., Gruber, A., Hegyiová, A., Sanchis-Dufau, A.D., Zamojski, D., Cordes, C., Wagner, W., Drusch, M., 2013. Global Automated Quality Control of In Situ Soil Moisture Data from the International Soil Moisture Network. Vadose Zone Journal 12, vzj2012.0097. https://doi.org/10.2136/vzj2012.0097

Ek, M., Mitchell, K., Lin, Y., Rogers, E., Grunmann, P., Koren, V., Gayno, G., Tarpley, J., 2003. Implementation of Noah land surface model advances in the National Centers for Environmental Prediction operational mesoscale Eta model. Journal of Geophysical Research: Atmospheres 108.

El Hajj, M., Baghdadi, N., Zribi, M., Rodríguez-Fernández, N., Wigneron, J.P., Al-Yaari, A., Al Bitar, A., Albergel, C., Calvet, J.-C., 2018. Evaluation of SMOS, SMAP, ASCAT and Sentinel-1 soil moisture

products at sites in Southwestern France. Remote Sensing 10, 569.
Elachi, C., 1987. Spaceborne imaging radar research in the 1990 s: An overview. Johns Hopkins APL Technical Digest 8, 60–64.
Engman, E.T., Chauhan, N., 1995. Status of microwave soil moisture measurements with remote sensing. Remote Sensing of Environment 51, 189–198.
Entekhabi, D., Nakamura, H., Njoku, E.G., 1994. Solving the inverse problem for soil moisture and temperature profiles by sequential assimilation of multifrequency remotely sensed observations. IEEE Transactions on Geoscience and Remote Sensing 32, 438–448.
Entekhabi, D., Reichle, R.H., Koster, R.D., Crow, W.T., 2010. Performance Metrics for Soil Moisture Retrievals and Application Requirements. Journal of Hydrometeorology 11, 832–840. https://doi.org/10.1175/2010JHM1223.1
Evett, S., Steiner, J., 1995. Precision of neutron scattering and capacitance type soil water content gauges from field calibration. Soil Science Society of America Journal 59, 961–968.
Faridani, F., Farid, A., Ansari, H., Manfreda, S., 2017a. A modified version of the SMAR model for estimating root-zone soil moisture from time-series of surface soil moisture. WSA 43, 492. https://doi.org/10.4314/wsa.v43i3.14
Faridani, F., Farid, A., Ansari, H., Manfreda, S., 2017b. Estimation of the Root-Zone Soil Moisture Using Passive Microwave Remote Sensing and SMAR Model. J. Irrig. Drain Eng. 143, 04016070. https://doi.org/10.1061/(ASCE)IR.1943-4774.0001115
Fascetti, F., Pierdicca, N., Pulvirenti, L., Crapolicchio, R., Muñoz-Sabater, J., 2016. A comparison of ASCAT and SMOS soil moisture retrievals over Europe and Northern Africa from 2010 to 2013. International journal of applied earth observation and geoinformation 45, 135–142.
Fernandez-Moran, R., Al-Yaari, A., Mialon, A., Mahmoodi, A., Al Bitar, A., De Lannoy, G., Rodriguez-Fernandez, N., Lopez-Baeza, E., Kerr, Y., Wigneron, J.-P., 2017. SMOS-IC: An Alternative SMOS Soil Moisture and Vegetation Optical Depth Product. Remote Sensing 9, 457. https://doi.org/10.3390/rs9050457
FRIEDL, M.A., STRAHLER, A.H., HODGES, J., 2010. ISLSCP II MODIS (Collection 4) IGBP Land Cover, 2000-2001

3.564251 MB. https://doi.org/10.3334/ORNLDAAC/968

Gleeson, T., Moosdorf, N., Hartmann, J., van Beek, L.P.H., 2014. A glimpse beneath earth's surface: GLobal HYdrogeology MaPS (GLHYMPS) of permeability and porosity. Geophys. Res. Lett. 41, 3891–3898. https://doi.org/10.1002/2014GL059856

Gruber, A., De Lannoy, G., Albergel, C., Al-Yaari, A., Brocca, L., Calvet, J.-C., Colliander, A., Cosh, M., Crow, W., Dorigo, W., Draper, C., Hirschi, M., Kerr, Y., Konings, A., Lahoz, W., McColl, K., Montzka, C., Muñoz-Sabater, J., Peng, J., Reichle, R., Richaume, P., Rüdiger, C., Scanlon, T., Van Der Schalie, R., Wigneron, J.-P., Wagner, W., 2020. Validation practices for satellite soil moisture retrievals: What are (the) errors? Remote Sensing of Environment 244, 111806. https://doi.org/10.1016/j.rse.2020.111806

Gruber, A., Scanlon, T., van der Schalie, R., Wagner, W., Dorigo, W., 2019a. Evolution of the ESA CCI Soil Moisture climate data records and their underlying merging methodology. Earth Syst. Sci. Data 11, 717–739. https://doi.org/10.5194/essd-11-717-2019

Gruber, A., Scanlon, T., van der Schalie, R., Wagner, W., Dorigo, W., 2019b. Evolution of the ESA CCI Soil Moisture climate data records and their underlying merging methodology. Earth System Science Data 11, 717–739.

Guo, J., Shi, X., Ke, S., Li, Y., Hu, C., Zwain, H.M., Gu, J., Chunyun, Z., Li, A., Shenghong, L., others, 2023. Climate Change Critique on Dams and Anthropogenic Impact to Mediterranean Mountains for Freshwater Ecosystem-a Review. Polish Journal of Environmental Studies 32.

Gupta, Sc., Larson, W., 1979. Estimating soil water retention characteristics from particle size distribution, organic matter percent, and bulk density. Water resources research 15, 1633–1635.

H SAF, 2021. SSM ASCAT DR2021 EXT TS12.5ASCAT Surface Soil Moisture Climate Data Record v7 12.5 km sampling - Metop. https://doi.org/10.15770/EUM_SAF_H_0009

H SAF, 2020. ASCAT SSM CDR v5 12.5 kmASCAT Surface Soil Moisture Climate Data Record v5 12.5 km sampling - Metop. https://doi.org/10.15770/EUM_SAF_H_0006

Hallikainen, M., Ulaby, F., Dobson, M., El-Rayes, M., 1985.

Microwave dielectric behaviour of wet soil—Part II: Dielectric-mixing models. IEEE Transactions on Geoscience and Remote Sensing 23, 35–46.
Haugaasen, T., Peres, C.A., 2005. Primate assemblage structure in Amazonian flooded and unflooded forests. American Journal of Primatology: Official Journal of the American Society of Primatologists 67, 243–258.
Heimovaara, T., 1994. Frequency domain analysis of time domain reflectometry waveforms: 1. Measurement of the complex dielectric permittivity of soils. Water Resources Research 30, 189–199.
Henry, J.-B., Chastanet, P., Fellah, K., Desnos, Y.-L., 2006. Envisat multi-polarized ASAR data for flood mapping. International Journal of Remote Sensing 27, 1921–1929.
Henyey, L.G., Greenstein, J.L., 1941. Diffuse radiation in the galaxy. Astrophysical Journal, vol. 93, p. 70-83 (1941). 93, 70–83.
Hilhorst, M.A., 2000. A Pore Water Conductivity Sensor. Soil Sci. Soc. Am. J. 64, 1922–1925. https://doi.org/10.2136/sssaj2000.6461922x
Hillel, D., 2003. Introduction to environmental soil physics. Elsevier.
Hirmas, D.R., Giménez, D., Nemes, A., Kerry, R., Brunsell, N.A., Wilson, C.J., 2018. Climate-induced changes in continental-scale soil macroporosity may intensify water cycle. Nature 561, 100–103. https://doi.org/10.1038/s41586-018-0463-x
Hoekstra, P., Delaney, A., 1974. Dielectric properties of soils at UHF and microwave frequencies. Journal of geophysical research 79, 1699–1708.
Hollinger, S.E., Isard, S.A., 1994. A soil moisture climatology of Illinois. Journal of Climate 7, 822–833.
Hook, W., Livingston, N., 1996. Errors in converting time domain reflectometry measurements of propagation velocity to estimates of soil water content. Soil Science Society of America Journal 60, 35–41.
Horritt, M., Mason, D., Cobby, D., Davenport, I., Bates, P., 2003. Waterline mapping in flooded vegetation from airborne SAR imagery. Remote Sensing of Environment 85, 271–281.
Houser, P.R., Shuttleworth, W.J., Famiglietti, J.S., Gupta, H.V., Syed, K.H., Goodrich, D.C., 1998. Integration of soil moisture remote sensing and hydrologic modeling using data assimilation. Water

resources research 34, 3405–3420.
Hupet, F., Trought, M.C.T., Greven, M., Green, S.R., Clothier, B.E., 2005. Data requirements for identifying macroscopic water stress parameters: A study on grapevines: ESTIMATION OF MACROSCOPIC WATER STRESS PARAMETERS. Water Resour. Res. 41. https://doi.org/10.1029/2004WR003609
IPCC, A., others, 2013. Climate change 2013: the physical science basis. Contribution of working group I to the fifth assessment report of the intergovernmental panel on climate change 1535.
Jackson, T., Schugge, T., Nicks, A., Coleman, G., Engman, E., 1981. Soil moisture updating and microwave remote sensing for hydrological simulation/La remise à jour de l'état d'humidité des sols en vue de la simulation hydrologique. Hydrological Sciences Journal 26, 305–319.
Jackson, T.J., 1986. Soil water modeling and remote sensing. IEEE Transactions on Geoscience and Remote Sensing 37–46.
Jackson, T.J., O'Neill, P.E., Swift, C.T., 1997. Passive microwave observation of diurnal surface soil moisture. IEEE Transactions on Geoscience and Remote Sensing 35, 1210–1222.
Jackson, T.J., Schmugge, J., Engman, E., 1996. Remote sensing applications to hydrology: soil moisture. Hydrological Sciences Journal 41, 517–530.
Jackson, T.J., Schmugge, T.J., 1989. Passive microwave remote sensing system for soil moisture: Some supporting research. IEEE transactions on geoscience and remote sensing 27, 225–235.
Jarvis, N., Leeds-Harrison, P., 1987. Some problems associated with the use of the neutron probe in swelling/shrinkling clay soils. Journal of Soil Science 38, 149–156.
Jin, H., Eklundh, L., 2014. A physically based vegetation index for improved monitoring of plant phenology. Remote Sensing of Environment 152, 512–525. https://doi.org/10.1016/j.rse.2014.07.010
Keenan, T.F., Gray, J., Friedl, M.A., Toomey, M., Bohrer, G., Hollinger, D.Y., Munger, J.W., O'Keefe, J., Schmid, H.P., Wing, I.S., others, 2014. Net carbon uptake has increased through warming-induced changes in temperate forest phenology. Nature Climate Change 4, 598–604.
Kerr, Y.H., Waldteufel, P., Richaume, P., Wigneron, J.P., Ferrazzoli, P., Mahmoodi, A., Al Bitar,

A., Cabot, F., Gruhier, C., Juglea, S.E., others, 2012. The SMOS soil moisture retrieval algorithm. IEEE transactions on geoscience and remote sensing 50, 1384–1403.

Kerr, Y.H., Waldteufel, P., Wigneron, J.-P., Martinuzzi, J., Font, J., Berger, M., 2001. Soil moisture retrieval from space: The Soil Moisture and Ocean Salinity (SMOS) mission. IEEE transactions on Geoscience and remote sensing 39, 1729–1735.

Koeppen, W., Pilger, E., Wright, R., 2011. Time series analysis of infrared satellite data for detecting thermal anomalies: a hybrid approach. Bulletin of Volcanology 73, 577–593.

Koster, R.D., Dirmeyer, P.A., Guo, Z., Bonan, G., Chan, E., Cox, P., Gordon, C.T., Kanae, S., Kowalczyk, E., Lawrence, D., Liu, P., Lu, C.-H., Malyshev, S., McAvaney, B., Mitchell, K., Mocko, D., Oki, T., Oleson, K., Pitman, A., Sud, Y.C., Taylor, C.M., Verseghy, D., Vasic, R., Xue, Y., Yamada, T., 2004. Regions of Strong Coupling Between Soil Moisture and Precipitation. Science 305, 1138–1140. https://doi.org/10.1126/science.1100217

Kottek, M., Grieser, J., Beck, C., Rudolf, B., Rubel, F., 2006. World Map of the Köppen-Geiger climate classification updated. metz 15, 259–263. https://doi.org/10.1127/0941-2948/2006/0130

Kumar, S.V., Peters-Lidard, C.D., Tian, Y., Houser, P.R., Geiger, J., Olden, S., Lighty, L., Eastman, J.L., Doty, B., Dirmeyer, P., others, 2006. Land information system: An interoperable framework for high resolution land surface modeling. Environmental modelling & software 21, 1402–1415.

Lacava, T., Ciancia, E., Faruolo, M., Pergola, N., Satriano, V., Tramutoli, V., 2019. On the Potential of RST-FLOOD on Visible Infrared Imaging Radiometer Suite Data for Flooded Areas Detection. Remote Sensing 11, 598. https://doi.org/10.3390/rs11050598

Lacava, T., Coviello, I., Faruolo, M., Mazzeo, G., Pergola, N., Tramutoli, V., 2013. A Multitemporal Investigation of AMSR-E C-Band Radio-Frequency Interference. IEEE Trans. Geosci. Remote Sensing 51, 2007–2015. https://doi.org/10.1109/TGRS.2012.2228487

Lacava, T., Greco, M., Di Leo, E., Martino, G., Pergola, N., Sannazzaro, F., Tramutoli, V., 2005. Monitoring soil wetness variations by means of satellite passive microwave observations: the HYDROPTIMET study cases. Natural Hazards and

Earth System Sciences 5, 583–592.
Lacava, T., Matgen, P., Brocca, L., Bittelli, M., Pergola, N., Moramarco, T., Tramutoli, V., 2012. A first assessment of the SMOS soil moisture product with in situ and modeled data in Italy and Luxembourg. IEEE Transactions on Geoscience and Remote Sensing 50, 1612–1622.
Laio, F., 2006. A vertically extended stochastic model of soil moisture in the root zone. Water resources research 42.
Laio, F., Porporato, A., Ridolfi, L., Rodriguez-Iturbe, I., 2001. Plants in water-controlled ecosystems: active role in hydrologic processes and response to water stress: II. Probabilistic soil moisture dynamics. Advances in water resources 24, 707–723.
Lakhankar, T., Krakauer, N., Khanbilvardi, R., 2009. Applications of microwave remote sensing of soil moisture for agricultural applications. International Journal of Terraspace Science and Engineering 2, 81–91.
Li, X., Al-Yaari, A., Schwank, M., Fan, L., Frappart, F., Swenson, J., Wigneron, J.-P., 2020. Compared performances of SMOS-IC soil moisture and vegetation optical depth retrievals based on Tau-Omega and Two-Stream microwave emission models. Remote Sensing of Environment 236, 111502.
Li, X., Wigneron, J.-P., Frappart, F., Fan, L., Ciais, P., Fensholt, R., Entekhabi, D., Brandt, M., Konings, A.G., Liu, X., others, 2021. Global-scale assessment and inter-comparison of recently developed/reprocessed microwave satellite vegetation optical depth products. Remote Sensing of Environment 253, 112208.
Liang, X., Lettenmaier, D.P., Wood, E.F., Burges, S.J., 1994. A simple hydrologically based model of land surface water and energy fluxes for general circulation models. Journal of Geophysical Research: Atmospheres 99, 14415–14428.
Liang, X., Wood, E.F., Lettenmaier, D.P., 1996. Surface soil moisture parameterization of the VIC-2L model: Evaluation and modification. Global and Planetary Change 13, 195–206.
Lin, C.-P., 2003. Frequency domain versus travel time analyses of TDR waveforms for soil moisture measurements. Soil Science Society of America Journal 67, 720–729.
Lionello, P., Abrantes, F., Gacic, M., Planton, S., Trigo, R., Ulbrich, U., 2014. The climate of the Mediterranean region: research progress and climate

change impacts. Reg Environ Change 14, 1679–1684. https://doi.org/10.1007/s10113-014-0666-0

Liu, Yongwei, Liu, Yuanbo, Wang, W., 2019. Inter-comparison of satellite-retrieved and Global Land Data Assimilation System-simulated soil moisture datasets for global drought analysis. Remote Sensing of Environment 220, 1–18. https://doi.org/10.1016/j.rse.2018.10.026

Liu, Y.Y., Parinussa, R.M., Dorigo, W.A., De Jeu, R.A.M., Wagner, W., Van Dijk, A.I.J.M., McCabe, M.F., Evans, J.P., 2011. Developing an improved soil moisture dataset by blending passive and active microwave satellite-based retrievals. Hydrol. Earth Syst. Sci. 15, 425–436. https://doi.org/10.5194/hess-15-425-2011

Loew, A., Schlenz, F., 2011. A dynamic approach for evaluating coarse scale satellite soil moisture products. Hydrol. Earth Syst. Sci. 15, 75–90. https://doi.org/10.5194/hess-15-75-2011

Ma, H., Zeng, J., Chen, N., Zhang, X., Cosh, M.H., Wang, W., 2019. Satellite surface soil moisture from SMAP, SMOS, AMSR2 and ESA CCI: A comprehensive assessment using global ground-based observations. Remote Sensing of Environment 231, 111215. https://doi.org/10.1016/j.rse.2019.111215

Malardel, S., Wedi, N., Deconinck, W., Diamantakis, M., Kuehnlein, C., Mozdzynski, G., Hamrud, M., Smolarkiewicz, P., 2016. A new grid for the IFS. https://doi.org/10.21957/ZWDU9U5I

Malnes, E., Storvold, R., Lauknes, I., Solbo, S., Solberg, R., Amlien, J., Koren, H., 2005. Multi-sensor monitoring of snow parameters in Nordic mountainous areas, in: Proceedings. 2005 IEEE International Geoscience and Remote Sensing Symposium, 2005. IGARSS'05. IEEE, pp. 1951–1954.

Manabe, S., 1969. Climate and the ocean circulation: I. The atmospheric circulation and the hydrology of the earth's surface. Monthly weather review 97, 739–774.

Manfreda, S., Brocca, L., Moramarco, T., Melone, F., Sheffield, J., 2014. A physically based approach for the estimation of root-zone soil moisture from surface measurements. Hydrol. Earth Syst. Sci. 18, 1199–1212. https://doi.org/10.5194/hess-18-1199-2014

Manfreda, S., Lacava, T., Onorati, B., Pergola, N., Di Leo, M.,

Margiotta, M.R., Tramutoli, V., 2011. On the use of AMSU-based products for the description of soil water content at basin scale. Hydrol. Earth Syst. Sci. 15, 2839–2852. https://doi.org/10.5194/hess-15-2839-2011

Manfreda, S., McCabe, M.F., Fiorentino, M., Rodríguez-Iturbe, I., Wood, E.F., 2007. Scaling characteristics of spatial patterns of soil moisture from distributed modelling. Advances in Water Resources 30, 2145–2150. https://doi.org/10.1016/j.advwatres.2006.07.009

Masson-Delmotte, V., Zhai, P., Pirani, S., Connors, C., Péan, S., Berger, N., Caud, Y., Chen, L., Goldfarb, M., Scheel Monteiro, P.M., 2021. Ipcc, 2021: Summary for policymakers. in: Climate change 2021: The physical science basis. contribution of working group i to the sixth assessment report of the intergovernmental panel on climate change.

McNeill, S.J., Lilburne, L.R., Carrick, S., Webb, T.H., Cuthill, T., 2018. Pedotransfer functions for the soil water characteristics of New Zealand soils using S-map information. Geoderma 326, 96–110. https://doi.org/10.1016/j.geoderma.2018.04.011

Milly, P., 1993. An analytic solution of the stochastic storage problem applicable to soil water. Water Resources Research 29, 3755–3758.

Min, X., Shangguan, Y., Huang, J., Wang, H., Shi, Z., 2022. Relative Strengths Recognition of Nine Mainstream Satellite-Based Soil Moisture Products at the Global Scale. Remote Sensing 14, 2739. https://doi.org/10.3390/rs14122739

Minet, J., Lambot, S., Delaide, G., Huisman, J.A., Vereecken, H., Vanclooster, M., 2010. A generalized frequency domain reflectometry modeling technique for soil electrical properties determination. Vadose zone journal 9, 1063–1072.

Miralles, D.G., van den Berg, M.J., Teuling, A.J., de Jeu, R.A.M., 2012. Soil moisture-temperature coupling: A multiscale observational analysis: SOIL MOISTURE-TEMPERATURE COUPLING. Geophys. Res. Lett. 39, n/a-n/a. https://doi.org/10.1029/2012GL053703

Mitchell, K.E., Lohmann, D., Houser, P.R., Wood, E.F., Schaake, J.C., Robock, A., Cosgrove, B.A., Sheffield, J., Duan, Q., Luo, L., others, 2004. The multi-institution North American Land Data

Assimilation System (NLDAS): Utilizing multiple GCIP products and partners in a continental distributed hydrological modeling system. Journal of Geophysical Research: Atmospheres 109.

Mittelbach, H., Lehner, I., Seneviratne, S.I., 2012. Comparison of four soil moisture sensor types under field conditions in Switzerland. Journal of Hydrology 430, 39–49.

Mohammed, P.N., Aksoy, M., Piepmeier, J.R., Johnson, J.T., Bringer, A., 2016. SMAP L-Band Microwave Radiometer: RFI Mitigation Prelaunch Analysis and First Year On-Orbit Observations. IEEE Trans. Geosci. Remote Sensing 54, 6035–6047. https://doi.org/10.1109/TGRS.2016.2580459

Muñoz-Sabater, J., Dutra, E., Agustí-Panareda, A., Albergel, C., Arduini, G., Balsamo, G., Boussetta, S., Choulga, M., Harrigan, S., Hersbach, H., Martens, B., Miralles, D.G., Piles, M., Rodríguez-Fernández, N.J., Zsoter, E., Buontempo, C., Thépaut, J.-N., 2021. ERA5-Land: a state-of-the-art global reanalysis dataset for land applications. Earth Syst. Sci. Data 13, 4349–4383. https://doi.org/10.5194/essd-13-4349-2021

Myneni, R.B., Keeling, C., Tucker, C.J., Asrar, G., Nemani, R.R., 1997. Increased plant growth in the northern high latitudes from 1981 to 1991. Nature 386, 698–702.

Naeimi, V., Paulik, C., Bartsch, A., Wagner, W., Kidd, R., Park, S.-E., Elger, K., Boike, J., 2012. ASCAT Surface State Flag (SSF): Extracting information on surface freeze/thaw conditions from backscatter data using an empirical threshold-analysis algorithm. IEEE Transactions on Geoscience and Remote Sensing 50, 2566–2582.

Naeimi, V., Scipal, K., Bartalis, Z., Hasenauer, S., Wagner, W., 2009. An Improved Soil Moisture Retrieval Algorithm for ERS and METOP Scatterometer Observations. IEEE Trans. Geosci. Remote Sensing 47, 1999–2013. https://doi.org/10.1109/TGRS.2008.2011617

Nasta, P., Bogena, H.R., Sica, B., Weuthen, A., Vereecken, H., Romano, N., 2020a. Integrating Invasive and Non-invasive Monitoring Sensors to Detect Field-Scale Soil Hydrological Behavior. Front. Water 2, 26. https://doi.org/10.3389/frwa.2020.00026

Nasta, P., Palladino, M., Sica, B., Pizzolante, A., Trifuoggi, M., Toscanesi, M., Giarra, A., D'Auria, J., Nicodemo, F.,

Mazzitelli, C., Lazzaro, U., Di Fiore, P., Romano, N., 2020b. Evaluating pedotransfer functions for predicting soil bulk density using hierarchical mapping information in Campania, Italy. Geoderma Regional 21, e00267. https://doi.org/10.1016/j.geodrs.2020.e00267

Nasta, P., Palladino, M., Ursino, N., Saracino, A., Sommella, A., Romano, N., 2017. Assessing long-term impact of land-use change on hydrological ecosystem functions in a Mediterranean upland agro-forestry catchment. Science of The Total Environment 605–606, 1070–1082. https://doi.org/10.1016/j.scitotenv.2017.06.008

Njoku, E.G., Entekhabi, D., 1996. Passive microwave remote sensing of soil moisture. Journal of hydrology 184, 101–129.

Noto, L., Cipolla, G., Pumo, D., Francipane, A., 2023. Climate change in the Mediterranean Basin (Part II): A review of challenges and uncertainties in climate change modeling and impact analyses. Water Resources Management 1–17.

Noto, L.V., Cipolla, G., Francipane, A., Pumo, D., 2023. Climate change in the mediterranean basin (part I): Induced alterations on climate forcings and hydrological processes. Water Resources Management 37, 2287–2305.

Oliva, R., Daganzo, E., Kerr, Y.H., Mecklenburg, S., Nieto, S., Richaume, P., Gruhier, C., 2012. SMOS radio frequency interference scenario: Status and actions taken to improve the RFI environment in the 1400–1427-MHz passive band. IEEE Transactions on Geoscience and Remote Sensing 50, 1427–1439.

Olson, D.M., Dinerstein, E., 2002. The Global 200: Priority ecoregions for global conservation. Annals of the Missouri Botanical garden 199–224.

Olson, D.M., Dinerstein, E., 1998. The Global 200: A Representation Approach to Conserving the Earth's Most Biologically Valuable Ecoregions. Conservation Biology 12, 502–515. https://doi.org/10.1046/j.1523-1739.1998.012003502.x

Olson, D.M., Dinerstein, E., Wikramanayake, E.D., Burgess, N.D., Powell, G.V.N., Underwood, E.C., D'amico, J.A., Itoua, I., Strand, H.E., Morrison, J.C., Loucks, C.J., Allnutt, T.F., Ricketts, T.H., Kura, Y., Lamoreux, J.F., Wettengel, W.W., Hedao, P., Kassem, K.R., 2001. Terrestrial Ecoregions of the World: A New Map of Life on Earth. BioScience 51, 933.

https://doi.org/10.1641/0006-3568(2001)051[0933:TEOTWA]2.0.CO;2

Ontel, I., Irimescu, A., Boldeanu, G., Mihailescu, D., Angearu, C.-V., Nertan, A., Craciunescu, V., Negreanu, S., 2021. Assessment of Soil Moisture Anomaly Sensitivity to Detect Drought Spatio-Temporal Variability in Romania. Sensors 21, 8371. https://doi.org/10.3390/s21248371

Or, D., 2001. Who Invented the Tensiometer? Soil Sci. Soc. Am. J. 65, 1–3. https://doi.org/10.2136/sssaj2001.6511

Palagi, E., Coronese, M., Lamperti, F., Roventini, A., 2022. Climate change and the nonlinear impact of precipitation anomalies on income inequality. Proc. Natl. Acad. Sci. U.S.A. 119, e2203595119. https://doi.org/10.1073/pnas.2203595119

Paloscia, S., Macelloni, G., Santi, E., Koike, T., 2001. A multifrequency algorithm for the retrieval of soil moisture on a large scale using microwave data from SMMR and SSM/I satellites. IEEE Transactions on Geoscience and Remote Sensing 39, 1655–1661.

Parinussa, R., Holmes, T., Yilmaz, M., Crow, W., 2011. The impact of land surface temperature on soil moisture anomaly detection from passive microwave observations. Hydrology and Earth System Sciences 15, 3135–3151.

Parrens, M., Wigneron, J.-P., Richaume, P., Mialon, A., Al Bitar, A., Fernandez-Moran, R., Al-Yaari, A., Kerr, Y.H., 2016. Global-scale surface roughness effects at L-band as estimated from SMOS observations. Remote Sensing of Environment 181, 122–136. https://doi.org/10.1016/j.rse.2016.04.006

Pathe, C., Wagner, W., Sabel, D., Doubkova, M., Basara, J.B., 2009. Using ENVISAT ASAR global mode data for surface soil moisture retrieval over Oklahoma, USA. IEEE Transactions on Geoscience and Remote Sensing 47, 468–480.

Peng, J., Tanguy, M., Robinson, E.L., Pinnington, E., Evans, J., Ellis, R., Cooper, E., Hannaford, J., Blyth, E., Dadson, S., 2021. Estimation and evaluation of high-resolution soil moisture from merged model and Earth observation data in the Great Britain. Remote Sensing of Environment 264, 112610. https://doi.org/10.1016/j.rse.2021.112610

Pepin, S., Livingston, N., Hook, W., 1995. Temperature-dependent measurement

errors in time domain reflectometry determinations of soil water. Soil Science Society of America Journal 59, 38–43.
Pettorelli, N., Wegmann, M., Skidmore, A., Mücher, S., Dawson, T.P., Fernandez, M., Lucas, R., Schaepman, M.E., Wang, T., O'Connor, B., others, 2016. Framing the concept of satellite remote sensing essential biodiversity variables: challenges and future directions. Remote sensing in ecology and conservation 2, 122–131.
Pompeu, J., Ruiz, I., Ruano, A., Sanz, M.J., 2023. Sustainable land management for addressing soil conservation under climate change in Mediterranean landscapes: perspectives from the Mijares watershed. Euro-Mediterranean Journal for Environmental Integration 8, 41–54.
Porporato, A., Daly, E., Rodriguez-Iturbe, I., 2004. Soil water balance and ecosystem response to climate change. The American Naturalist 164, 625–632.
Porporato, A., Rodriguez-Iturbe, I., 2002. Ecohydrology-a challenging multidisciplinary research perspective / Ecohydrologie: une perspective stimulante de recherche multidisciplinaire. Hydrological Sciences Journal 47, 811–821. https://doi.org/10.1080/02626660209492985
Qiu, J., Crow, W.T., Nearing, G.S., 2016. The Impact of Vertical Measurement Depth on the Information Content of Soil Moisture for Latent Heat Flux Estimation. Journal of Hydrometeorology 17, 2419–2430. https://doi.org/10.1175/JHM-D-16-0044.1
Quast, R., Albergel, C., Calvet, J.-C., Wagner, W., 2019. A Generic First-Order Radiative Transfer Modelling Approach for the Inversion of Soil and Vegetation Parameters from Scatterometer Observations. Remote Sensing 11, 285. https://doi.org/10.3390/rs11030285
Quast, R., Wagner, W., 2016. Analytical solution for first-order scattering in bistatic radiative transfer interaction problems of layered media. Applied Optics 55, 5379–5386.
Ragab, R., 1995. Towards a continuous operational system to estimate the root-zone soil moisture from intermittent remotely sensed surface moisture. Journal of Hydrology 173, 1–25. https://doi.org/10.1016/0022-1694(95)02749-F
Rao, B.H., Singh, D., 2011. Moisture content determination by TDR and capacitance

techniques: a comparative study. Int. J. Earth Sci. Eng 4, 132–137.
Rawls, W., Brakensiek, D., 1989. Estimation of soil water retention and hydraulic properties, in: Unsaturated Flow in Hydrologic Modeling: Theory and Practice. Springer, pp. 275–300.
Rawls, W.J., Ahuja, L.R., Brakensiek, D.L., Shirmohammadi, A., others, 1992. Infiltration and soil water movement. McGraw-Hill Inc.
Rawls, W.J., Brakensiek, D.L., Saxtonn, K., 1982. Estimation of soil water properties. Transactions of the ASAE 25, 1316–1320.
Ray, R., Fares, A., He, Y., Temimi, M., 2017. Evaluation and Inter-Comparison of Satellite Soil Moisture Products Using In Situ Observations over Texas, U.S. Water 9, 372. https://doi.org/10.3390/w9060372
Reichle, R.H., De Lannoy, G.J., Forman, B.A., Draper, C.S., Liu, Q., 2014. Connecting satellite observations with water cycle variables through land data assimilation: Examples using the NASA GEOS-5 LDAS. Surveys in Geophysics 35, 577–606.
Ricketts, T.H., Dinerstein, E., Olson, D.M., Eichbaum, W., Loucks, C.J., DellaSala, D.A., Kavanagh, K., Hedao, P., Hurley, P., Carney, K., others, 1999. Terrestrial ecoregions of North America: a conservation assessment. Island Press.
Robinson, D.A., Campbell, C.S., Hopmans, J.W., Hornbuckle, B.K., Jones, S.B., Knight, R., Ogden, F., Selker, J., Wendroth, O., 2008. Soil moisture measurement for ecological and hydrological watershed-scale observatories: A review. Vadose zone journal 7, 358–389.
Robinson, M., Dean, T., 1993. Measurement of near surface soil water content using a capacitance probe. Hydrological processes 7, 77–86.
Robock, A., Vinnikov, K.Y., Srinivasan, G., Entin, J.K., Hollinger, S.E., Speranskaya, N.A., Liu, S., Namkhai, A., 2000. The Global Soil Moisture Data Bank. Bull. Amer. Meteor. Soc. 81, 1281–1299. https://doi.org/10.1175/1520-0477(2000)081<1281:TGSMDB>2.3.CO;2
Rodell, M., Houser, P., Jambor, U., Gottschalck, J., Mitchell, K., Meng, C.-J., Arsenault, K., Cosgrove, B., Radakovich, J., Bosilovich, M., others, 2004. The global land data assimilation system. Bulletin of the American Meteorological society 85, 381–394.

Rodríguez-Iturbe, I., Isham, V., Cox, D.R., Manfreda, S., Porporato, A., 2006. Space-time modeling of soil moisture: Stochastic rainfall forcing with heterogeneous vegetation: SPACE-TIME MODELING OF SOIL MOISTURE. Water Resour. Res. 42. https://doi.org/10.1029/2005WR004497

Rodriguez-Iturbe, I., Porporato, A., Ridolfi, L., Isham, V., Coxi, D.R., 1999. Probabilistic modelling of water balance at a point: the role of climate, soil and vegetation. Proc. R. Soc. Lond. A 455, 3789–3805. https://doi.org/10.1098/rspa.1999.0477

Rohini, K., Singh, D.N., 2004. Methodology for determination of electrical properties of soils. Journal of Testing and Evaluation 32, 62–68.

Romano, N., Santini, A., 1997. Effectiveness of using pedo-transfer functions to quantify the spatial variability of soil water retention characteristics. Journal of Hydrology 202, 137–157.

Rubel, F., Brugger, K., Haslinger, K., Auer, I., 2017. The climate of the European Alps: Shift of very high resolution Köppen-Geiger climate zones 1800–2100. Meteorologische Zeitschrift 26, 115–125.

Sabater, J.M., Jarlan, L., Calvet, J.-C., Bouyssel, F., De Rosnay, P., 2007. From near-surface to root-zone soil moisture using different assimilation techniques. Journal of Hydrometeorology 8, 194–206.

Salvucci, G.D., 2001. Estimating the moisture dependence of root zone water loss using conditionally averaged precipitation. Water Resources Research 37, 1357–1365.

Satriani, A., Loperte, A., Soldovieri, F., 2015. Integrated geophysical techniques for sustainable management of water resource. A case study of local dry bean versus commercial common bean cultivars. Agricultural Water Management 162, 57–66.

Saxton, K.E., Rawls, W.J., 2006. Soil water characteristic estimates by texture and organic matter for hydrologic solutions. Soil science society of America Journal 70, 1569–1578.

Saxton, K.E., Rawls, W.J., Romberger, J.S., Papendick, R.I., 1986. Estimating Generalized Soil-water Characteristics from Texture. Soil Science Society of America Journal 50, 1031–1036. https://doi.org/10.2136/sssaj1986.03615995005000040039x

Scheinost, A., Sinowski, W., Auerswald, K., 1997. Regionalization of soil water retention curves in a highly variable soilscape, I. Developing a new pedotransfer function. Geoderma 78, 129–143.

Schmugge, T., Jackson, T., McKim, H., 1980. Survey of methods for soil moisture determination. Water Resources Research 16, 961–979.

Schmugge, T., Wang, J., Asrar, G., 1988. Results from the push broom microwave radiometer flights over the Konza Prairie in 1985. IEEE Transactions on Geoscience and Remote Sensing 26, 590–596.

Schmugge, T.J., 1983. Remote sensing of soil moisture: Recent advances. IEEE Transactions on Geoscience and Remote Sensing 336–344.

Schmullius, C., Furrer, R., 1992. Frequency dependence of radar backscattering under different moisture conditions of vegetation-covered soil. International Journal of Remote Sensing 13, 2233–2245.

Schumann, G., Hostache, R., Puech, C., Hoffmann, L., Matgen, P., Pappenberger, F., Pfister, L., 2007. High-resolution 3-D flood information from radar imagery for flood hazard management. IEEE transactions on geoscience and remote sensing 45, 1715–1725.

Schwartz, B.F., Schreiber, M.E., Yan, T., 2008. Quantifying field-scale soil moisture using electrical resistivity imaging. Journal of Hydrology 362, 234–246.

Scipal, Klaus, Drusch, M., Wagner, W., 2008. Assimilation of a ERS scatterometer derived soil moisture index in the ECMWF numerical weather prediction system. Advances in water resources 31, 1101–1112.

Scipal, K, Holmes, T., De Jeu, R., Naeimi, V., Wagner, W., 2008. A possible solution for the problem of estimating the error structure of global soil moisture data sets. Geophysical Research Letters 35.

Sellers, P., Mintz, Y., Sud, Y. e al, Dalcher, A., 1986. A simple biosphere model (SiB) for use within general circulation models. Journal of the atmospheric sciences 43, 505–531.

Seneviratne, S.I., Corti, T., Davin, E.L., Hirschi, M., Jaeger, E.B., Lehner, I., Orlowsky, B., Teuling, A.J., 2010. Investigating soil moisture–climate interactions in a changing climate: A review. Earth-Science Reviews 99, 125–161. https://doi.org/10.1016/j.earscirev.2010.02.004

Sharkov, E.A., 2003. Passive microwave remote sensing of the Earth: physical foundations. Springer Science & Business Media.

Singh, A., Meena, G.K., Kumar, S., Gaurav, K., 2019. Evaluation of the Penetration Depth of L- and S-Band (NISAR mission) Microwave SAR Signals into Ground, in: 2019 URSI Asia-Pacific Radio Science Conference (AP-RASC). Presented at the 2019 URSI Asia-Pacific Radio Science Conference (AP-RASC), IEEE, New Delhi, India, pp. 1–1. https://doi.org/10.23919/URSIAP-RASC.2019.8738217

Singh, D., Sing, K., Herlin, I., Sharma, S., 2003. Ground—Based scatterometer measurements of periodic surface roughness and correlation length for remote sensing. Advances in Space Research 32, 2281–2286.

Solbø, S., Solheim, I., 2005. Towards operational flood mapping with satellite SAR, in: Envisat & ERS Symposium.

Sperry, J., Hacke, U., Oren, R., Comstock, J., 2002. Water deficits and hydraulic limits to leaf water supply. Plant, cell & environment 25, 251–263.

Stamm, J.F., Wood, E.F., Lettenmaier, D.P., 1994. Sensitivity of a GCM simulation of global climate to the representation of land-surface hydrology. Journal of Climate 7, 1218–1239.

Starks, P.J., Heathman, G.C., Jackson, T.J., Cosh, M.H., 2006. Temporal stability of soil moisture profile. Journal of hydrology 324, 400–411.

Stroud, P.D., 1999. A recursive exponential filter for time-sensitive data. Los Alamos National Laboratory, Tech. Rep. LAUR-99-5573 131.

S.U., S.L., Singh, D.N., Shojaei Baghini, M., 2014. A critical review of soil moisture measurement. Measurement 54, 92–105. https://doi.org/10.1016/j.measurement.2014.04.007

Su, Z., Troch, P.A., De Troch, F., 1997. Remote sensing of bare surface soil moisture using EMAC/ESAR data. International journal of remote sensing 18, 2105–2124.

Tavakol, A., Rahmani, V., Quiring, S.M., Kumar, S.V., 2019. Evaluation analysis of NASA SMAP L3 and L4 and SPoRT-LIS soil moisture data in the United States. Remote Sensing of Environment 229, 234–246. https://doi.org/10.1016/j.rse.2019.05.006

Teuling, A.J., Hirschi, M., Ohmura, A., Wild, M., Reichstein, M., Ciais, P., Buchmann, N., Ammann, C., Montagnani, L., Richardson, A.D., Wohlfahrt, G., Seneviratne, S.I., 2009. A

regional perspective on trends in continental evaporation: EVAPORATION TRENDS. Geophys. Res. Lett. 36, n/a-n/a. https://doi.org/10.1029/2008GL036584

Topp, G.C., Davis, J., Annan, A.P., 1980. Electromagnetic determination of soil water content: Measurements in coaxial transmission lines. Water resources research 16, 574–582.

Tramutoli, V., 2007. Robust satellite techniques (RST) for natural and environmental hazards monitoring and mitigation: Theory and applications, in: 2007 International Workshop on the Analysis of Multi-Temporal Remote Sensing Images. IEEE, pp. 1–6.

Tramutoli, V., 1998. Robust AVHRR Techniques (RAT) for environmental monitoring: theory and applications, in: Earth Surface Remote Sensing II. SPIE, pp. 101–113.

Ulaby, F., Moore, R., Fung, A., 1982. Microwave remote sensing: Active and passive. Volume 2-Radar remote sensing and surface scattering and emission theory.

Ulaby, F.T., 1986. Microwave remote sensing active and passive. theory to applications 2059–2081.

Ulaby, F.T., Dubois, P.C., Van Zyl, J., 1996. Radar mapping of surface soil moisture. Journal of hydrology 184, 57–84.

Ungaro, F., Calzolari, C., 2001. Using existing soil databases for estimating retention properties for soils of the Pianura Padano-Veneta region of North Italy. Geoderma 99, 99–121.

Vachaud, G., Passerat De Silans, A., Balabanis, P., Vauclin, M., 1985. Temporal Stability of Spatially Measured Soil Water Probability Density Function. Soil Science Society of America Journal 49, 822–828. https://doi.org/10.2136/sssaj1985.03615995004900040006x

Van de Griend, A.A., Engman, E.T., 1985. Partial area hydrology and remote sensing. Journal of Hydrology 81, 211–251.

Van der Schalie, R., De Jeu, R., Rodríguez-Fernández, N., Al-Yaari, A., Kerr, Y., Wigneron, J.-P., Parinussa, R., Drusch, M., 2018. The effect of three different data fusion approaches on the quality of soil moisture retrievals from multiple passive microwave sensors. Remote Sensing 10, 107.

Van Genuchten, M.T., 1980. A closed-form equation for predicting the hydraulic conductivity of unsaturated soils. Soil science society of America journal 44, 892–898.

Vereecken, H., Maes, J., Feyen, J., 1990. Estimating unsaturated

hydraulic conductivity from easily measured soil properties. Soil Science 149, 1–12.
Wagner, W., 1998. Soil moisture retrieval from ERS scatterometer data. Citeseer.
Wagner, W., Lemoine, G., Borgeaud, M., Rott, H., 1999a. A study of vegetation cover effects on ERS scatterometer data. IEEE Transactions on Geoscience and Remote Sensing 37, 938–948.
Wagner, W., Lemoine, G., Rott, H., 1999b. A Method for Estimating Soil Moisture from ERS Scatterometer and Soil Data. Remote Sensing of Environment 70, 191–207. https://doi.org/10.1016/S0034-4257(99)00036-X
Wagner, W., Lindorfer, R., Melzer, T., Hahn, S., Bauer-Marschallinger, B., Morrison, K., Calvet, J.-C., Hobbs, S., Quast, R., Greimeister-Pfeil, I., others, 2022. Widespread occurrence of anomalous C-band backscatter signals in arid environments caused by subsurface scattering. Remote Sensing of Environment 276, 113025.
Walfish, S., 2006. A review of statistical outlier methods. Pharmaceutical technology 30, 82.
Walker, J., Houser, P., 2002. Soil moisture estimation using remote sensing, in: Proceedings of the 27th Hydrology and Water Resources Symposium.
Wang, J., King, J., Wilheit, T., Szejwach, G., Gesell, L., Nieman, R., Niver, D., Krupp, B., Gagliano, J., 1983. Profiling atmospheric water vapor by microwave radiometry. Journal of climate and Applied Meteorology 779–788.
Wang, J.R., Engman, E.T., Mo, T., Schmugge, T.J., Shiue, J., 1987. The effects of soil moisture, surface roughness, and vegetation on L-band emission and backscatter. IEEE Transactions on Geoscience and Remote Sensing 825–833.
Wang, J.R., Schmugge, T.J., 1980. An empirical model for the complex dielectric permittivity of soils as a function of water content. IEEE Transactions on Geoscience and remote sensing 288–295.
Wang, T., Franz, T.E., You, J., Shulski, M.D., Ray, C., 2017. Evaluating controls of soil properties and climatic conditions on the use of an exponential filter for converting near surface to root zone soil moisture contents. Journal of Hydrology 548, 683–696. https://doi.org/10.1016/j.jhydrol.2017.03.055
Wigneron, J.-P., Fan, L., Ciais, P., Bastos, A., Brandt, M., Chave,

J., Saatchi, S., Baccini, A., Fensholt, R., 2020. Tropical forests did not recover from the strong 2015–2016 El Niño event. Sci. Adv. 6, eaay4603. https://doi.org/10.1126/sciadv.aay4603

Wigneron, J.-P., Li, X., Frappart, F., Fan, L., Al-Yaari, A., De Lannoy, G., Liu, X., Wang, M., Le Masson, E., Moisy, C., 2021. SMOS-IC data record of soil moisture and L-VOD: Historical development, applications and perspectives. Remote Sensing of Environment 254, 112238.

Wigneron, J.-P., Schmugge, T., Chanzy, A., Calvet, J.-C., Kerr, Y.H., 1998. Use of passive microwave remote sensing to monitor soil moisture. Agronomie 18, 27–43.

WOOD, E.F., 1991. Global scale hydrology: Advances in land surface modeling. Reviews of Geophysics 29, 193–201.

Wood, E.F., Lettenmaier, D.P., Zartarian, V.G., 1992. A land-surface hydrology parameterization with subgrid variability for general circulation models. Journal of Geophysical Research: Atmospheres 97, 2717–2728.

Wood, E.F., Lin, D.-S., Mancini, M., Thongs, D., Troch, P., Jackson, T., Famiglietti, J., Engman, E., 1993. Intercomparisons between passive and active microwave remote sensing, and hydrological modeling for soil moisture. Advances in Space Research 13, 167–176.

Xue, Y., Sellers, P., Kinter, J., Shukla, J., 1991. A simplified biosphere model for global climate studies. Journal of climate 4, 345–364.

Zheng, J., Zhao, T., Lü, H., Shi, J., Cosh, M.H., Ji, D., Jiang, L., Cui, Q., Lu, H., Yang, K., Wigneron, J.-P., Li, X., Zhu, Y., Hu, L., Peng, Z., Zeng, Y., Wang, X., Kang, C.S., 2022. Assessment of 24 soil moisture datasets using a new in situ network in the Shandian River Basin of China. Remote Sensing of Environment 271, 112891. https://doi.org/10.1016/j.rse.2022.112891

Zwieback, S., Colliander, A., Cosh, M.H., Martínez-Fernández, J., McNairn, H., Starks, P.J., Thibeault, M., Berg, A., 2018. Estimating time-dependent vegetation biases in the SMAP soil moisture product. Hydrol. Earth Syst. Sci. 22, 4473–4489. https://doi.org/10.5194/hess-22-4473-2018